



UNIVERSITY OF CAPE TOWN

MSC THESIS

---

# Chaos and Scrambling in Quantum Small Worlds

---

Author:

Jean-Gabriel Keiser Hartmann

Supervisors:

Prof. J. Murugan

Dr. J. Shock

*A thesis submitted in fulfilment of the requirements for the degree of MSc  
in the*

*Laboratory for Quantum Gravity and Strings  
Department of Mathematics and Applied Mathematics  
Faculty of Science*

June 24, 2020

---

## Abstract

---

In this thesis, we introduce a novel class of many-body quantum system, which we term ‘quantum small worlds’. These are strongly-interacting systems that interpolate between completely ordered (nearest-neighbour, next-to-nearest-neighbour etc.) and completely random interactions. They are systems of quantum spin particles in which the network topology is given by the Watts-Strogatz model of network theory.

As such, they furnish a novel laboratory for studying quantum systems transitioning between integrable and non-integrable behaviour. Our motivation is to understand how the dynamics of the system are affected by this transition, particularly with regards to the ability of the system to scramble (quantum) information, and potential emergence of chaotic behaviour.

Our work begins with a review of the relevant literature regarding algebraic graph theory and quantum chaos. Next, we introduce the model by starting from a well understood integrable system, a spin- $\frac{1}{2}$  Heisenberg, or Ising, chain. We then inject a small number of long-range interactions and study its ability to scramble quantum information using two primary devices: the out-of-time-order correlator (OTOC) and the spectral form factor (SFF). We find that the system shows increasingly rapid scrambling as its interactions become progressively more random, with no evidence of quantum chaos as diagnosed by either of these devices.

---

## Declaration

---

I DECLARE THAT:

1. I am presenting this dissertation in full fulfilment of the requirements for my degree.
2. I know the meaning of plagiarism and declare that all of the work in the dissertation, save for that which is properly acknowledged, is my own.
3. I hereby grant the University of Cape Town free licence to reproduce for the purpose of research either the whole or any portion of the contents in any manner whatsoever of the above dissertation.

---

Jean-Gabriel Keiser Hartmann

---

## Acknowledgements

---

I would like to begin by thanking the National Institute of Theoretical Physics (NITheP) for providing the funding that allowed me to pursue these studies.

Of course, none of this work would have been possible without the support of my supervisors, Prof. Jeff Murugan and Dr. Jonathan Shock. Thank you for your guidance and mentorship; I am truly grateful. I also wish to thank our collaborator, Dario Rosa, for sharing his time and expertise.

To all of the members of the QGasLab and HEPCAT groups, I am grateful for the many insightful discussions we have had.

To my parents, Mark and Marie, my brother Tristan, and my grandmother Faith Hartmann, thank you for your unwavering support and encouragement, regardless of the difficulties we have faced. I would not be who I am without you.

Lastly, and most importantly, to my fiancée, Shannon Sass, you are my shining light, my beacon of hope; thank you for all your love and patience.

---

# Contents

---

<b>List of Figures</b>	<b>vi</b>	
<b>1</b>	<b>Introduction</b>	<b>1</b>
1.1	Background and Motivation	1
1.2	Thesis Overview	5
<b>2</b>	<b>Classical Small Worlds</b>	<b>7</b>
2.1	Introduction	7
2.2	Graph-theoretic Formalism	8
2.2.1	Definitions	8
2.2.2	Architectures	10
2.2.3	Network Measures	11
2.3	Small-world Model	18
2.3.1	Construction	18
2.3.2	Analysis	19
2.4	Summary	24
<b>3</b>	<b>Diagnostics of Quantum Chaos</b>	<b>28</b>
3.1	Introduction	28
3.2	Spectral Statistics	29

3.2.1	r-Statistic	34
3.3	Time-Dependent Signatures	37
3.3.1	Out-of-time-order Correlation Functions	37
3.3.2	Spectral Form Factor	41
3.4	Summary	44
<b>4</b>	<b>Quantum Small Worlds</b>	<b>46</b>
4.1	Introduction	46
4.2	Methodology	47
4.2.1	Network Initialisation	48
4.2.2	Hamiltonian Construction	49
4.2.3	Numerical Diagonalisation	52
4.3	Analysis	52
4.3.1	Out-of-time-order Correlators	52
4.3.2	Spectral Form Factors	69
4.3.3	Eigenvalue Statistics	73
4.4	Summary	75
<b>5</b>	<b>Conclusion</b>	<b>77</b>
5.1	Thesis Summary	77
5.2	Outlook	81
<b>Appendices</b>		<b>83</b>
A	Mathematica Code Package	83
<b>Bibliography</b>		<b>96</b>

---

## List of Figures

---

2.1	Graph topologies of one-dimensional spin chains featuring nearest-neighbour interactions, with $N = 11$ vertices. . . . .	11
2.2	$k$ -regular cycle graphs of order 11 (11 vertices). $k$ is typically even, except for complete graphs of even order, where then $k = N - 1$ . . . . .	12
2.3	Erdős-Rényi and Gilbert random graphs of order 11, with $M = 22$ and $p = 0.4$ , respectively. Note that the graph in $G(11, 0, 4)$ has $\mathbb{E}[M] = 22$ but in fact contains only 19 edges. . . . .	13
2.4	Two identical random graphs of $G(6, 9)$ differing only in vertex numbering. The change in numbering corresponds to a circular permutation of the vertices. This permutation is therefore also applied to the rows and columns of the adjacency matrices, as well as to the elements of the degree distribution. . . . .	14
2.5	A random graph of $G(6, 9)$ and associated distance matrix $\mathbf{D}(g)$ . Note that one of the shortest paths between vertices 3 and 6 has been highlighted, but that it is not unique, as there exist other paths of equal length. . . . .	16
2.6	Neighbourhoods (red) of vertex 1 (black) in graphs of varying connectivities. . . . .	17
2.7	Procedure of the Watts-Strogatz Algorithm for constructing a small-world network. . . . .	20
2.8	Results of the Watts-Strogatz Algorithm for $N = 20$ , $K = 6$ , and varying $p$ . . . . .	22

2.9	Small-worldness parameters as functions of the rewiring probability, averaged over 50 realizations for $N = 1000$ and $K = 20$ . The vertical dashed lines at $p = 0.1$ indicate the value at which the small-worldness is maximised, according to Watts and Strogatz. The horizontal lines in 2.9c and 2.9d show the regions in which the authors classify the networks as small-world. . . . .	26
2.10	Small-worldness parameters as functions of the rewiring probability, averaged over 50 realizations, showing dependence on the number of vertices and edges in the networks. . . . .	27
3.1	Examples of $4 \times 4$ random matrices drawn from the Gaussian ensembles. . . . .	31
3.2	Graphs illustrating the distribution of eigenvalues and eigenvalue spacings in Gaussian random matrices. . . . .	33
3.3	Graphs illustrating the structure of the density of states for the GUE and a random spin network of equal size. . . . .	35
3.4	Hypothetical plot of $\langle r \rangle$ as a function of a parametric disorder term in a given system. . . . .	37
3.5	Log-log plot of $g(t; \beta = 5)$ for random matrices sampled from the GUE of dimension $2^{12}$ . Image reproduced from (1). . . . .	43
4.1	Example Spin Models . . . . .	52
4.2	OTOCs for the Ising spin chain given by (4.11) with $N = 10$ vertices. Each figure plots the quantity $C_0^{\mu\nu}(v, t)$ in (4.9) as a function of time, $t$ , and vertex position, $v$ . These plots indicate how the different operators spread through the periodic chain following an initial perturbation applied at vertex 1. . . . .	55
4.3	Log-Log plots of the OTOCs, for vertices 2 through 5, from Figure 4.2, focusing on the growth at early timescales. The dashed lines represent the power-law expressions given by (4.12) to (4.14). . . . .	56
4.4	Contour and 2D plots of the OTOCs for different rewiring probabilities. Note that the colour of the curve refers to the OTOC probed at the corresponding vertex of the same colour on the graph. . . . .	58

4.5	Contour and 2D plots for an Ising network of next-to-nearest-neighbour interactions for varying rewiring probabilities. . . . .	59
4.6	Contour plots of $C_0^{zz}(v, t)$ using different methods of ordering the vertices. . . . .	60
4.7	Plots indicating the initial growth periods of the OTOCs for varying rewiring probabilities. In (a) and (b), the green highlighted points indicate convexity, at times $t \leq t_v^*$ , with the red vertical lines at $t = t_v^*$ for each vertex $v$ . The curves in (c) are for rewiring probabilities $p = 0, 0.1, 0.5, 1.0$ on networks with $N = 10$ and $K = 1$ . For $p \neq 0$ , each data point was obtained by taking the disorder average over 10 randomly generated networks sampled from the ensemble $G_{SW}(10, 1, p)$ . . . . .	61
4.8	Log-log plots of the OTOCs for networks generated with (a) $p = 0.1$ and (b) $p = 1$ , showing power-law behaviour. The solid lines are the $C_0^{zz}(v, t)$ , and the dashed lines are given by the power-law expression of (4.14), with $l = d(1, v)$ . . . . .	62
4.9	Plots indicating the (a, b) exponential and (c, d) power-law fitted models for (a, c) $p = 0.1$ and (b, d) $p = 1$ . The models were fitted to the convex regions of each curve (highlighted green), where $t \leq t_v^*$ . The goodness-of-fit is given by the $R^2$ statistic, averaged over each of the curves. The legends indicate the best-fit exponents (b) for each fitted model, with the curves numbered sequentially in time. . . . .	63
4.10	Log-log plots of the OTOCs for networks generated with (a) $p = 0$ , (b) $p = 0.1$ and (c) $p = 1$ , showing power-law behaviour. The solid lines are the $C_0^{zz}(v, t)$ , and the dashed lines are given by the power-law expression of (4.14), with $l = d(1, v)$ . The colours of each curve indicate distance from the initial site. . . . .	64
4.11	OTOCs for the regular, and random, next-to-nearest neighbour networks with $N = 10$ . The red curve indicates the mean, $\langle C_0^{zz}(t) \rangle_v$ , averaged over the $N$ vertices, plotted with standard deviation on the error bars. The horizontal dashed line at 1 represents the value of the correlations at which the system is said to be scrambled. . . . .	65

- 4.12 OTOCs for the Heisenberg XXZ model with  $N = 10$  and  $K = 1$  nearest-neighbour interactions, at  $p = 0, 0.1, 1$  in columns 1,2 and 3, respectively. The first row depicts the graph for which the OTOCs were computed. The second row shows a 3D plot of the initial perturbation propagating over the system. The third row shows the 2D plot of the OTOCs projected onto the same plane. The colouring of vertices (in the first row) and curves (in the third row), reflects the edge distance  $d(1, v)$ , to vertex 1 (red). . . . . 66
- 4.13 OTOCs for the Heisenberg XXZ model with  $N = 10$  and  $K = 2$  next-to-nearest-neighbour interactions, at  $p = 0, 0.1, 1$ . The first row depicts the graph for which the OTOCs were computed. The second row shows a 3D plot of the initial perturbation propagating over the system. The third row shows the 2D plot of the OTOCs projected onto the same plane. The colouring of vertices (in the first row) and curves (in the third row), reflects the edge distance  $d(1, v)$ , to vertex 1 (red). . . . . 67
- 4.14 Log-log plots of the early-time behaviour of the  $C_0^{zz}(v, t)$  for the Heisenberg XXZ model, with  $N = 10$  vertices. Row 1 corresponds to the OTOCs, with  $K = 1$  nearest neighbour interaction, from Figure 4.12. Row 2 corresponds to the OTOCs, with  $K = 2$  next-to-nearest neighbour interaction, from Figure 4.13. The columns, from left to right, represent increasing rewiring probabilities,  $p = 0, 0.1, 1$ . In each plot, the solid curves are the computed OTOCs, highlighted by colour depending on edge distance from vertex 1. The dashed lines represent the power law curves. . . . . 68
- 4.15 Log-log plots of the early-time behaviour of the  $C_0^{zz}(v, t)$  for the Heisenberg XXZ model, with  $N = 10$  vertices. In each plot, the solid curves are the computed OTOCs, highlighted by colour depending on edge distance from vertex 1. The red dashed lines represent the original power law curves predicted by (2). The black dashed lines represent the modified power law curves given by (4.19). . . . . 69

---

## LIST OF FIGURES

---

4.16 Replotted OTOCs for the 6 network configurations of Figures 4.12 and 4.13, showing the scrambling behaviour. The dotted black curves are the original curves $C_0^{zz}(v, t)$ . The blue dashed lines represent the correlator values at which the scrambling is expected to maximise. The red curve is the mean correlation, $\langle C_0^{zz}(t) \rangle_v$ , averaged over each vertex, with standard deviation on the error bars. . . . .	70
4.17 Spectral form factors $g(t; 0)$ , at infinite temperature, for various rewiring probabilities of the Heisenberg XXX network of $N = 11$ vertices. The plot on the left is for the regular chain with $p = 0$ . The central plot is of the small-world network containing a small number of rewirings (1 $\Rightarrow$ $p \approx 0.09$ in black, 2 $\Rightarrow$ $p \approx 0.18$ , in blue and 3 $\Rightarrow$ $p \approx 0.27$ in red). The plot on the right is for $p = 1$ , corresponding to a random graph. The disorder average is taken over $J = 100$ realizations of each network. . . . .	71
4.18 Log-log plot of the function $\cos t$ for small values of $t$ . . . . .	71
4.19 Plot of the spectral form factors for varying system sizes, with a fixed number of edges, $K = 2$ , and (a) 3 rewirings and (b) completely random graphs. . . . .	72
4.20 Network graph and normalised eigenvalue spectrum for a periodic Ising chain of 5 particles and nearest-neighbour interactions. Note that we normalise the spectrum in the range 0 to 1, since we are more interested in their relative values, for the spacing distribution. . . . .	74
4.21 Eigenvalue spectra for the chain of 5 particles, illustrating the effects of an external field and edge weightings on the system energy levels. . . . .	76

# Chapter 1

---

## Introduction

---

### 1.1 Background and Motivation

Quantum small worlds are many-body quantum systems that are able to transition between completely ordered and disordered behaviour, through the introduction of random, long-range, interactions. These form a novel class of models of strongly-correlated quantum matter – systems in which the dynamics are dominated by strong couplings between the constituent particles – where qualitatively new behaviour emerges from the large number of interactions; behaviour that would not otherwise be observed by simply extrapolating from the, fundamentally well-understood, individual particles and interactions.

Indeed, two such phenomena that have received significant attention in the last five to ten years are (many-body) quantum chaos and (quantum information) scrambling. As for classical systems, chaos is characterised by sensitive dependence on initial conditions (colloquially, the butterfly effect; introduced by Lorenz (3; 4)). However, for quantum mechanical systems, understanding this sensitivity is more complex. This is the case since one does not, particularly for many-body problems, have well-defined particle trajectories. Without being able to extract a classical Lyapunov exponent that would indicate

exponential divergence of the trajectories (5), classifying a quantum system as chaotic is more subtle, and less well-defined. Historically, quantum chaos (chaology, according to Berry (6)) was concerned with the study of the quantum mechanical origins of classically chaotic systems in the classical limit. More recently, the field of many-body quantum chaos has gained traction through the work of Shenker and Stanford (7), in their study of the butterfly effect in strongly-coupled large- $N$  theories.

The concept of scrambling was first introduced, in the context of the black hole information problem, by Hayden and Preskill (8), and refined by Susskind and Sekino (9), thereby bridging the fields of quantum information theory and high energy physics. It describes the process by which the quanta of information contained in the initial state become spread over all the system degrees of freedom, and are no longer recoverable by simply probing any single local observable (10).

Furthermore, since this scrambling represents an effective loss of memory in a system, it is closely related to quantum thermalisation in closed quantum systems, whereby an initially out-of-equilibrium system reaches thermal equilibrium through unitary time evolution. The study of closed quantum thermalisation was initiated by Deutsch (11), and expanded by Srednicki's proposal of the Eigenstate Thermalisation Hypothesis (ETH) (12). Since there is no coupling to an external heat bath (as in an open system), the initial conditions become spread over the various subsystems. Thus, without probing a large number of observables over the whole system, there is an emergence of perceived irreversibility, despite unitary time evolution.

This is to be contrasted with many-body localisation (MBL), an extension of Anderson localisation (13) to many-body systems, introduced in the seminal work of Basko *et al* (14). Here, closed quantum systems exhibiting MBL fail to reach thermal equilibrium, and hence the information of the initial conditions is retained over long (infinite) timescales in local operators (15).

As alluded to above, while strongly-correlated quantum systems historically fell in the domain of condensed matter physics, the past five years have witnessed a tremendous global effort to understand the emergence of spacetime from the quantum properties of matter and information (16). This has been precipitated largely by studies of the gauge/-

gravity correspondence, following the groundbreaking work of Maldacena (17). In turn, this large body of recent work has redefined the boundaries of contemporary condensed matter physics, high energy theory and quantum information theory, resulting in a number of remarkable discoveries. Among these are: (i) Maldacena, Shenker and Stanford’s (MSS) bound on the growth rate of chaos in thermal quantum systems (18), (ii) Kitaev’s elaboration on the Sachdev-Ye spin-glass model (19) to the Sachdev-Ye-Kitaev (SYK) model (20) of the quantum mechanics of  $N$  Majorana fermions with infinitely long range disorder, and (iii) Witten’s insight (21) that the perturbative structure of the large- $N$  limit of the SYK model is the same as colored random tensor models (22), thereby uncovering a new and tractable sweet-spot in between vector models and matrix models. Within this context, there are three lessons that are of particular importance to us: (i) Chaos and scrambling are generic features of quantum systems that thermalise, (ii) novel classes of many-body spin networks are able to furnish a new laboratory for detailed study of the relationships between chaos, disorder, randomness and scrambling, which are not yet well-understood, and (iii) a new set of diagnostic measures is required for this work.

Regarding point (ii), we note that the vast majority of work on such systems falls into a small number of categories: (i) regular, integrable models, such as those of Ising or Heisenberg (2; 23), (ii) Infinite-range theories, with all-to-all random weighted interactions, such as the SY, SYK, infinite-range Heisenberg spin glass (24), Sherrington-Kirkpatrick (SK) (25) models, (iii) models featuring power-law interactions (26), and (iv) modified regular models with a disorder term, either through external interactions (27), longer-range hopping terms (28) or weighted interactions (29). We note that this classification is illustrative, not exhaustive. Moreover, it is worth mentioning the contemporary work of Bentsen *et al* (30), in which they analyse the scrambling behaviour on systems featuring sparse network topologies.

Under these considerations, it is apparent to us that most of the aforementioned models are either integrable or non-integrable. Therefore, we intend to introduce, and study, a model in which we may interpolate between these two classes of behaviour, through the introduction of a disorder parameter. To this end, we take a graph-theoretic approach towards constructing a network with parametric disorder, and propose the concept of a

quantum small world. This is a system in which the network topology is based on the Watts-Strogatz model (31) of small-world networks. This relatively simple model forms the foundations of modern network theory (32), and has been successfully applied to a wide range of phenomena in different fields of study, from human social networks, electrical transmission grids and the internet (31), to physical neural networks (33; 34) and protein interactions (35). The sheer breadth of the impact of the original article is evidenced by the > 40000 citations (as of January 2020), making it one of the most highly-cited papers of all time (36).

Beginning with a sparse, yet regular graph, we associate each vertex, and each edge, with a spin particle, and interaction, respectively. We will therefore be able to tune the amount of randomness in the system by probabilistically rewiring small numbers of the regular couplings. In this way, we can transition from a regular, completely ordered, network, to a completely disordered network of random couplings. This is a novel, yet general, approach to constructing a many-body network, and we will be able to apply our method to generate a wide range of network configurations.

Finally, let us turn to point (iii) above regarding diagnostics of chaos. We note that, to date, the primary measure in strongly-correlated systems has been the squared commutator, or equivalently, the out-of-time-order correlator (OTOC), which essentially measures how the commutativity of local operators in a system evolve in time, thereby providing a measure of the scrambling, or information spreading. First introduced by Larkin and Ovchinnikov (37), it was repurposed by Kitaev in his initial work on the SYK model, and used, most significantly, by Roberts and Stanford (38) to show that the SYK model saturates the MSS bound and is therefore a maximally chaotic theory. However, as pointed out by Hashimoto *et al* (39), they are still not yet well understood in generic quantum theories. Hence, a large body of work has developed around studying the OTOCs for different models of many-body systems.

In order to further understand exactly what information is encoded in the OTOCs, it has been necessary to compare them to other diagnostics that have been more well-established in the quantum chaos community, most notably the spectral statistics (5), and the spectral form factor (SFF) (1), drawn from the field of random matrix theory

---

(40). Most recently, theoretical work in understanding these diagnostics has uncovered some striking relationships. In particular, de Mello Koch *et al* (41) obtained the (two-point) SFF from the (two-point) OTOC averaged over the Heisenberg group for bosonic quantum systems. This was an extension of work initiated by Cotler *et al* (42). This is in addition to Ryu *et al*'s (43) work in uncovering a web of quantum chaos diagnostics in two-dimensional conformal field theories (2D CFTs). Finally, we mention Schalm *et al*'s proposal of an Operator Thermalisation Hypothesis (OTH), which is a fascinating contrast to the thermalisation due to dynamics, as proposed by the ETH. In the OTH, thermalisation occurs due to the specific choice of operator. Most surprisingly, their work shows that even non-interacting, free field, theories (containing an infinite set of conserved charges), are able to scramble through careful choice of composite operators.

With these considerations in mind, we turn to the central questions of our thesis: *What can we learn from, and about, OTOCs in the context of scrambling in strongly-correlated quantum systems that transition between completely ordered and completely disordered behaviour?*

## 1.2 Thesis Overview

In this thesis, we will be applying the Watts-Strogatz model of network theory to generate systems of randomly interacting quantum spins, and studying them through known diagnostics of quantum chaos.

In Chapter 2, we present a review of algebraic graph, and network, theory. Beginning with basic definitions and concepts, we build up the foundations that will enable us to describe the Watts-Strogatz model, the algorithm for its construction, as well as its properties. We go on to study these properties through a number of parameters that aim to quantify network ‘small-worldness’.

In Chapter 3, we introduce the theory of chaos in quantum systems. This begins with an historical overview of the field, where we discuss its origins in the study of the complex energy spectra of large atomic nuclei, and their relation to the mathematical field of

random matrix theory. Next, we consider two diagnostic tools, the out-of-time-order correlator and spectral form factor, which, in recent years, have been widely studied in the context of chaos in strongly-correlated condensed matter systems.

In Chapter 4, we present a detailed analysis of the numerical simulations of our quantum small world networks. We begin with a discussion of the methodology of our computations, and how these are applied to generate a quantum small world network. As part of our analysis, we confirm the validity of our numerical procedures by reproducing existing results in the literature for well-known spin chains. We then go on to introduce increasing levels of disorder into these networks through the random rewiring procedure outlined in Chapter 2. We analyse their effects on the model through calculations of the out-of-time-order correlators and spectral form factors as the network parameters for edge density and amount of rewiring are varied. Besides the confirmatory work in reproducing known results, the work in this chapter is original and has been submitted for publication (44).

In Chapter 5, we conclude this thesis with a summary of its aims, content, and central results. We go on to discuss a number of potential directions for future work on this topic, beginning with the existing shortcomings and how best they may be improved, as well as further extensions. We note that some of this work is currently ongoing.

# Chapter 2

---

## Classical Small Worlds

---

I read somewhere that everybody on this planet is separated by only six other people. Six degrees of separation between us and everyone else on this planet. The President of the United States, a gondolier in Venice, just fill in the names... I am bound, you are bound, to everyone on this planet by a trail of six people.

---

‘Ouisa Kitteridge’ in *Six Degrees of Separation*  
John Guare (45)

### 2.1 Introduction

First penned by John Guare in his 1990 screenplay of the same name (45), the term ‘six degrees of separation’ was used to describe the observed small-world phenomenon within the context of human social networks; heuristically, this is based on the observation, first attributed to the Hungarian writer Karinthy in his 1929 anthology ‘Everything is Different’ (32), that globalisation has lead to a society in which any two individuals

on the planet are ‘connected’ by a chain of, on average, six acquaintances. The first scientific experiments to explore this effect were conducted by the American social scientist Stanley Milgram in 1967 (46), and later formalised by Watts and Strogatz in their seminal paper ‘Collective Dynamics of Small-world Networks’ (31), that laid the mathematical foundations of modern network science (34), and forms the basis for our work.

In this chapter, we introduce the concepts from algebraic graph theory that will allow us to construct and characterise classical small-world networks. Section 2.2 presents a review of basic terminology that may be found in an introductory text on graph theory. Section 2.3 makes precise the notion of the small-world phenomenon in network science; we present the graph theoretic properties of such a model, an algorithmic approach to its construction, as well as modern measures for quantifying small-worldness in a given network.

## 2.2 Graph-theoretic Formalism

### 2.2.1 Definitions

We begin with a brief review of terminology from graph theory that is pertinent to our work. Formal definitions and results may be found in Appendix ??.

Mathematically, a *graph* is a pair  $G = (V, E)$  where  $V$  is the *vertex set* and  $E$  is the *edge set* of non-empty subsets of  $V$ . Elements  $v \in V$  and  $e \in E$  are called *vertices*, or nodes, and *edges*, or connections, respectively.

In pure mathematics, graph theory is a rich, though abstract, field of study. However its greatest strength lies in its application to real-world systems, or *networks*, in which vertices and edges represent objects and their interactions, respectively.

Beginning with this most general definition, we want to restrict ourselves to the classes of graphs that will be applicable to our particular systems of interest; those being quantum-mechanical spin systems whose dynamics are governed by spin-exchange interactions (see Chapter 4).

Since our intention is to perform numerical simulations, rather than, say, analytical calculations in the large  $N$  limit, we consider only *finite* graphs, having a finite number of vertices (graph *order*) and edges (graph *size*). Furthermore, we restrict ourselves to *connected* graphs, in which every vertex is connected to every other vertex by some sequence of edges (*walk* or *path*). In other words, we disregard any graphs that contain *isolated vertices* or *neighbourhoods*, since we want to study the effects of interactions acting over the full system. Finally, we are not interested in *multipartite*, or *k-partite*, graphs, in which  $V$  is partitioned into  $k$  independent sets  $V = V_1 \cap \dots \cap V_k$  such that there are no edges between vertices within each partition. Thus, it is possible for any vertex to be connected, or *adjacent*, to any other within our networks.

Regarding the spin-exchange interactions, we do not want our network to contain any self-interactions (loops) or repetitions. Graphs without these edges are called *simple*. Additionally, spin exchange operates on pairs of spin particles, thus we consider only *dyadic* graphs, in which  $E \subseteq V \times V$  contains only 2-element subsets of  $V$ .

Of course higher order interactions exist; for example we could consider a 4-particle interaction of the form used in the SYK model, or even combinations of varying orders, which would fall under the general class of *hypergraphs*. For the purposes of this dissertation, however, we will focus our calculations on the simple case of 2-particle interactions. Finally, since the spin exchange operates on two particles symmetrically, we need only consider *undirected* graphs, having edges that do not distinguish between ‘in’ and ‘out’ vertices (as in a *directed* graph).

Given these constraints, we still have a number of degrees of freedom to consider in constructing our networks. Most obviously is the actual graph architecture, or topology, which we discuss in detail in Section 2.3. Another is the interaction strength; we can consider either *binary*, or *unweighted*, graphs, in which all edges represent interactions of equal strength, or *weighted* graphs, in which we may vary the relative interaction strength of connections. Although unweighted graphs are useful for extracting basic information based on the overall graph structure, they often contain a large number of internal symmetries that may mask more fundamental features. In this case, further work can be done by sampling individual edge weights as random variables from some statistical distribution.

Another reference to the SYK model is relevant here; the actual network topology is that of a *complete* graph, in which all vertices are connected to every other vertex. Since this introduces a large number of symmetries into the system, the (*hyper*)-edge weights are drawn from a Gaussian distribution (47).

### 2.2.2 Architectures

Having narrowed in on the classes of graphs in which we are interested, we can now discuss the different network topologies that will be relevant in our study of spin chains with long-range interactions.

To begin, let us consider the well-studied case of a one-dimensional spin chain, as considered in the Ising or Heisenberg models. These models feature only nearest-neighbour interactions, in which each vertex interacts only with its two nearest (spatial) neighbours. A further distinction may be made between those chains with non-periodic or periodic boundary conditions, as shown in Figure 2.1. The periodic chain is known as a *cycle* graph, denoted by  $C_N$ , where  $N$  is the number of vertices. It is also a *regular* graph, since each vertex has the same *degree*, or number of edges to which it is connected; in particular, it is a 2-regular graph.

Working toward our goal of constructing a network that exhibits the small-world phenomenon, and beginning with this fundamental structure of short-range connections, let us consider two variations that introduce long-range interactions into the system.

The first approach is inspired by the fully-connected structure of the SYK model, the complete graphs  $K_N$ ; we may generalise the notion of the (2-regular) cycle graph to that of a *k-regular* cycle, by introducing next-to-nearest-neighbour, next-to-next-to-nearest-neighbour (and so on), connections, as shown in Figure 2.2. These are known as *circulant* graphs, and denoted by  $C_N^k$ ; we may identify  $C_N^{N-1}$  as *isomorphic* to the complete graph  $K_N$ .

The second approach is to consider the class of *random* graphs, which are distinct from the regular, cycle, graphs in that their edges are chosen randomly. In fact, there are two

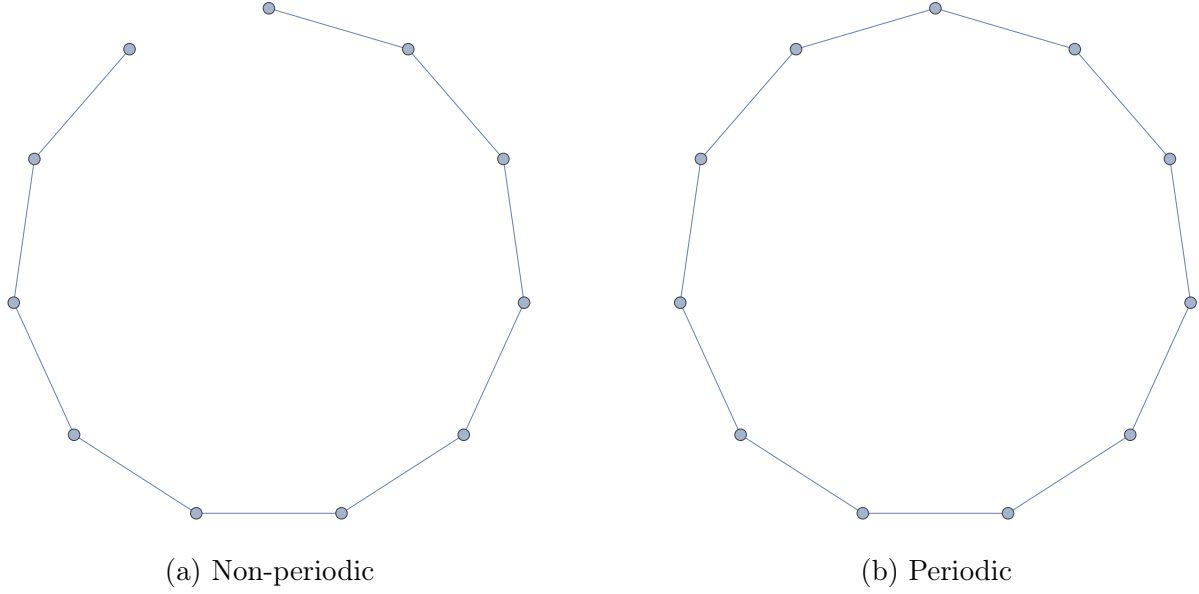


Figure 2.1: Graph topologies of one-dimensional spin chains featuring nearest-neighbour interactions, with  $N = 11$  vertices.

closely related models, the Erdős-Rényi (48),  $G(N, M)$ , and Gilbert (49),  $G(N, p)$ , random graphs, introduced independently in 1959. The  $G(N, M)$  model considers the ensemble of all possible graphs of order  $N$  and size  $M$ , where any one graph is drawn from this set (of  $\binom{N}{M}$  elements), with uniform probability  $\binom{N}{M}^{-1}$ . The  $G(N, p)$  model connects each possible pair of vertices, independently and uniformly, with probability  $p$ , resulting in a graph with  $\mathbb{E}[M] = p\binom{n}{2}$  edges. These two models therefore become equivalent in the limit  $\lim_{n \rightarrow \infty} G(N, p) = G(N, p\binom{n}{2})$ .

### 2.2.3 Network Measures

With these network architectures defined, we are almost in a position to construct and analyse small-world networks. However, we first need to introduce several measures that will be useful in analysing general graph properties.

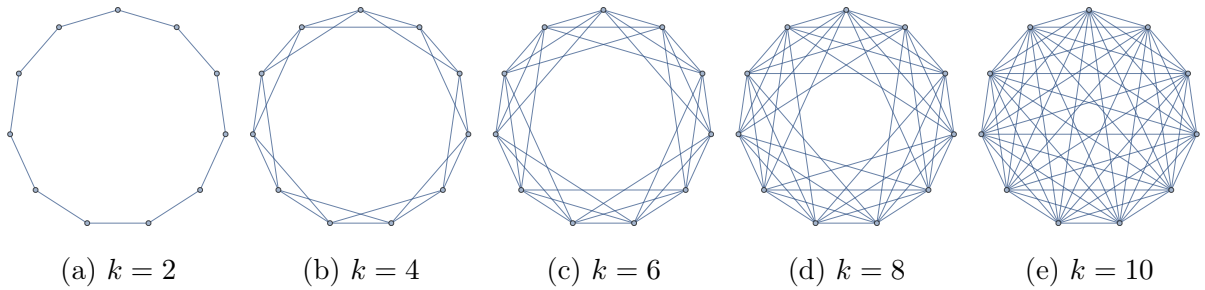


Figure 2.2:  $k$ -regular cycle graphs of order 11 (11 vertices).  $k$  is typically even, except for complete graphs of even order, where then  $k = N - 1$ .

## Basics

The simplest two graph measures are of course the graph order and size, which, as we have already seen, refer to the size of the vertex and edge sets, respectively;  $N = |V|$  and  $M = |E|$ . We have also introduced the vertex degree, which we use to define the *degree sequence*, a set of size  $N$  whose elements are the degree of the corresponding vertices,  $\{\deg(i) \mid 1 \leq i \leq N\}$ . This allows us to discuss a number of extensions, such as the *maximum degree*,  $\Delta(G)$ , and *minimum degree*,  $\delta(g)$ , and *degree distribution*,  $P(k) = \frac{N_k}{N}$ , where  $N_k$  is the number of vertices having degree  $k$ . We note that, by Euler's Handshaking Lemma for undirected graphs,

$$M = \frac{1}{2} \sum_{i=1}^N \deg(i) \quad (2.1)$$

Relating the order and size of a graph provides a measure of the *density* of edges, as

$$\rho(G) = \frac{M}{\frac{1}{2}N(N-1)} \quad (2.2)$$

where the denominator is the number of edges in a complete graph of the same number of vertices (the maximum possible number of edges). Taking this ratio gives us the density as a fraction between 0 and 1. Similarly, we may define the *edge sparsity* as simply  $1 - \rho(G)$ . However, both of these are only global measures of the overall number of edges in a graph, and do not take into account local structures or additional features such as edge weightings; a number of alternative approaches to quantifying graph density have been proposed but are not relevant for our purposes, see, for example (50; 51).

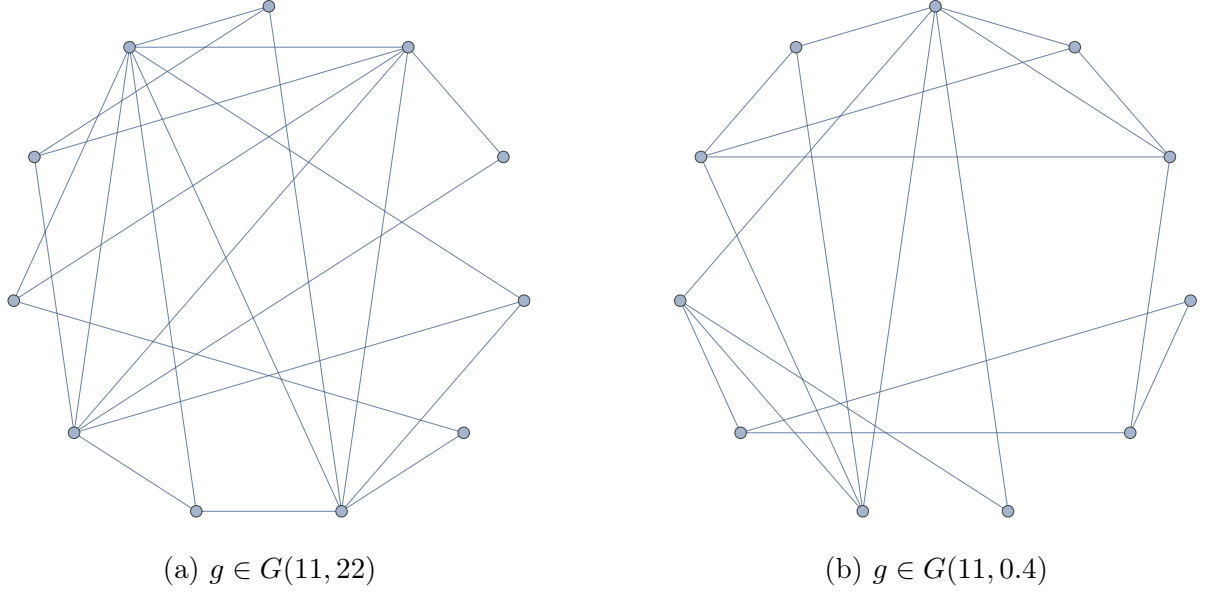


Figure 2.3: Erdős-Rényi and Gilbert random graphs of order 11, with  $M = 22$  and  $p = 0.4$ , respectively. Note that the graph in  $G(11, 0.4)$  has  $\mathbb{E}[M] = 22$  but in fact contains only 19 edges.

## Representations

The *adjacency matrix*, denoted  $\mathbf{A}$ , is one of the most fundamental measures used to describe graph connectivity; it is the matrix representation that we shall use most frequently to define our networks. Using the  $N$  rows and columns to represent vertices, each element  $A_{ij}$  corresponds to a possible edge,  $e_{ij}$ , between vertices  $i$  and  $j$ , as follows,

$$A_{ij} = \begin{cases} \omega_{ij} & e_{ij} \in E \\ 0 & \text{otherwise} \end{cases} \quad (2.3)$$

where  $\omega_{ij}$  is the weight of edge  $e_{ij}$ ; for simplicity, we shall refer to a binary graph as a special case of a weighted graph in which all edges have unit weighting.

The adjacency matrix is particularly useful, since it completely defines the topology of the associated network. It is worth noting at this point that this representation (and

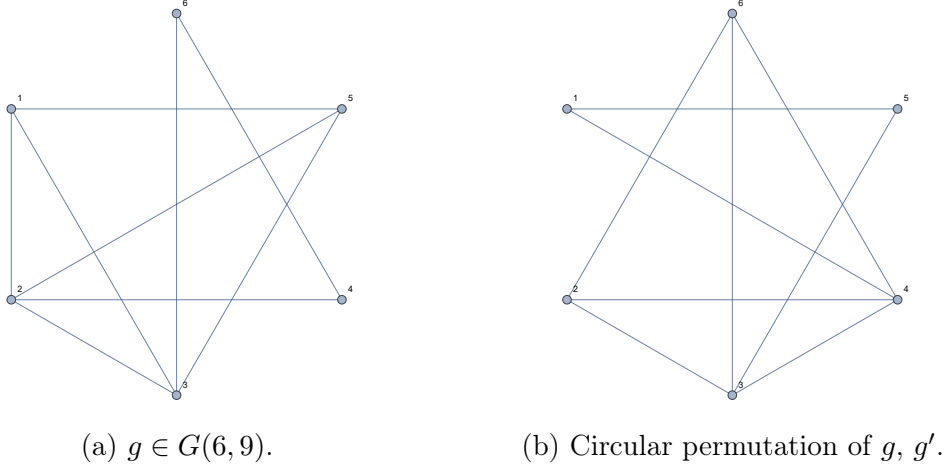


Figure 2.4: Two identical random graphs of  $G(6, 9)$  differing only in vertex numbering. The change in numbering corresponds to a circular permutation of the vertices. This permutation is therefore also applied to the rows and columns of the adjacency matrices, as well as to the elements of the degree distribution.

others, including the degree sequence), is not unique, since it is dependent on the vertex numbering scheme applied. As an example to illustrate this, see Figure 2.4, where the graph  $g'$  is obtained from  $g$  by circular permutation of the vertices, leading to the following adjacency matrices:

$$\mathbf{D}(g) = \begin{pmatrix} 0 & 1 & 1 & 0 & 1 & 0 \\ 1 & 0 & 1 & 1 & 1 & 0 \\ 1 & 1 & 0 & 0 & 1 & 1 \\ 0 & 1 & 0 & 0 & 0 & 1 \\ 1 & 1 & 1 & 0 & 0 & 0 \\ 0 & 0 & 1 & 1 & 0 & 0 \end{pmatrix} \quad \mathbf{D}(g') = \begin{pmatrix} 0 & 0 & 0 & 1 & 1 & 0 \\ 0 & 0 & 1 & 1 & 0 & 1 \\ 0 & 1 & 0 & 1 & 1 & 1 \\ 1 & 1 & 1 & 0 & 0 & 1 \\ 1 & 0 & 1 & 0 & 0 & 0 \\ 0 & 1 & 1 & 1 & 0 & 0 \end{pmatrix}$$

Note that, although the vertex numberings, and hence adjacency matrices, differ between these otherwise identical graphs, the eigenvalue spectra of the adjacency matrices are the same, namely  $\{1 + \sqrt{5}, -2, 1 - \sqrt{5}, -1, 1, 0\}$ .

While the adjacency matrix and degree sequence describe direct connections between

vertex pairs, a further class of measures is based on indirect connections spanned by sequences of edges. We have briefly mentioned the concept of a path; to be precise, a path is a sequence of unique edges connecting two vertices such that no edge or vertex is traversed more than once. In general, a sequence that may contain only repeated vertices is a *trail*, and one that may contain repeated vertices and edges is called a *walk*. More specifically, a path that starts and ends at the same vertex is a *cycle*.

## Global Integration

Now, we have already seen that paths are important for determining whether a given graph is connected or not, but they are also used for analysing many other graph properties. Indeed, they naturally lead to the notion of *distance* in a graph: The distance  $d(i, j)$  is simply the *shortest path length* between vertices  $i$  and  $j$ . It is easy to define the length of a given path as simply the sum of edge weights in its edge sequence, and to understand the concept of a shortest path; however, efficiently determining the actual shortest path for a vertex pair is a non-trivial computational process. A number of algorithms exist for finding the shortest path for different types of graphs, the most well-known being Dijkstra's algorithm (52) for positively-weighted graphs. For graphs with possibly negatively-weighted edges, the Bellman-Ford algorithm (53) is often used, with the caveat that the given graph contains no negative cycles (cycle paths with negative length). In such cases, the Floyd-Warshall algorithm (54) is needed since it is able to identify negative cycles.

Being able to calculate distances between vertices leads to another important graph representation: the distance matrix,  $\mathbf{D}$ , containing the distances between all vertex pairs. Similarly to the adjacency matrix, each element of the  $N \times N$  matrix is given by  $D_{ij} = d(i, j)$ , the distance between vertices  $i$  and  $j$ . As an illustrative example, see Figure 2.5. A number of statistical measures may therefore be introduced based on the elements of the distance matrix: The *graph diameter* is the length of the longest path in the graph,  $\max(D_{ij})$ , and the *mean distance*, or *characteristic path length*, is, as the name suggests,

$$L = \frac{\sum_{i=1}^N \sum_{j=i+1}^N D_{ij}}{\frac{1}{2}N(N-1)}. \quad (2.4)$$

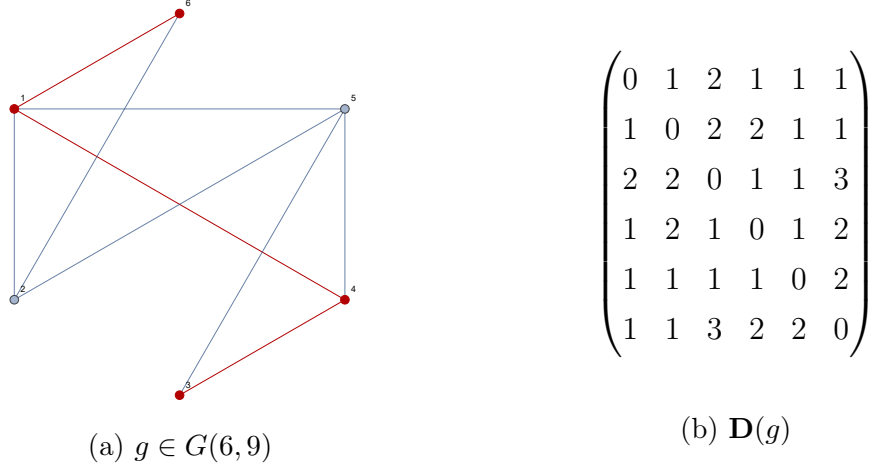


Figure 2.5: A random graph of  $G(6, 9)$  and associated distance matrix  $\mathbf{D}(g)$ . Note that one of the shortest paths between vertices 3 and 6 has been highlighted, but that it is not unique, as there exist other paths of equal length.

The characteristic path length was introduced by Watts and Strogatz (31), and is of particular importance to our study of small-world networks; it will be discussed in more detail in Section 2.3.2. It provides, in the words of Sporns (34), a measure of the global integration of the network, or, how easy it is for information to flow over long distances throughout the network.

### Local Clustering

Finally, we need to introduce a quantity that measures the strength of local connections within groups of vertices in the network. To be precise, a *neighbourhood*  $G_i(V_i, E_i) \subset G(V, E)$ , of vertex  $i$ , is the *induced subgraph* containing all vertices *adjacent* to vertex  $i$  (See Figure 2.6),

$$V_i = \{j \in V \mid e_{ij} \in E\} \quad (2.5)$$

$$E_i = \{e_{ij} \in E \mid i, j \in V_i\}. \quad (2.6)$$

Now, given that a neighbourhood is a graph in its own right, we can apply any of the measures previously introduced. However, the most important is simply the edge density

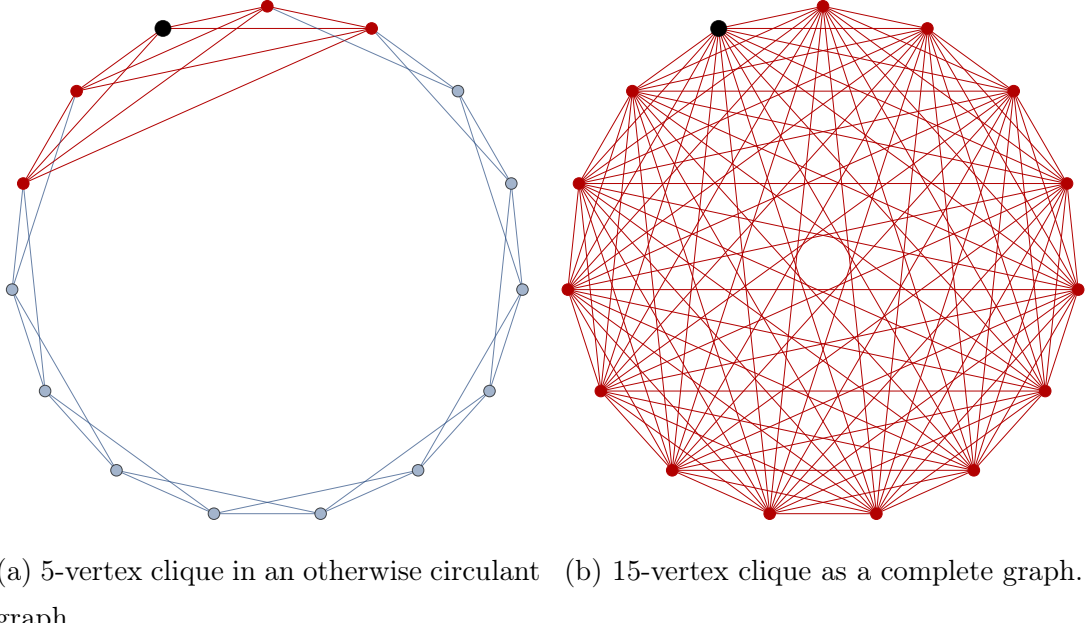


Figure 2.6: Neighbourhoods (red) of vertex 1 (black) in graphs of varying connectivities.

of the neighbourhood of vertex  $i$ , the *local clustering coefficient*,

$$C_i = \rho(G_i) = \frac{M_i}{\frac{1}{2}N_i(N_i - 1)}, \quad (2.7)$$

where  $M_i$  and  $N_i$  are the size and order of the neighbourhood. This is the ratio of the size of a neighbourhood relative to the complete graph of equal order, and gives a measure of how well connected the neighbours are. If the neighbourhood is complete (as in Figure 2.6a), then  $C_i = 1$  and it is referred to as a *clique*. By averaging over the clustering coefficients for each vertex in the graph, we obtain the *average clustering*, as introduced by Watts and Strogatz (31), which is fundamental to the study of small-world networks,

$$C = \frac{1}{N} \sum_{i=1}^N C_i. \quad (2.8)$$

## 2.3 Small-world Model

With the theoretical formalism in place, we are now in a position to put it to use in the construction and analysis of small-world networks. Originally proposed by Watts and Strogatz (31) as a network model that characterises the small-world phenomenon in complex systems, such networks have been successfully applied to a wide variety of complex systems in the biological, social and technological sciences (31; 34).

### 2.3.1 Construction

Heuristically, a small-world network is one that contains clusters of short-range connections, with a number of long-range, random, connections serving as bridges between clusters.

### Properties

In other words, we want networks that exhibit high average clustering and low characteristic path length. However another factor is important here, and that is the edge density of the network; we require networks to have low density, such that neighbourhoods are small relative to the size of the overall network.

As an example of why this is the case, consider a complete graph in which  $C = 1$  and  $L = 1$  are maximised and minimised, respectively (see Figure 2.6b). However, due to the fully-connected topology, it is not representative of a ‘small world’ as it is a single, large, neighbourhood.

These properties are made more precise in Table 2.1, using the terminology introduced in Section 2.2.3. Note that these are applicable to any vertices  $i, j \in V$  in the graph.

1	Edge Sparsity	$M \ll \frac{1}{2}N(N - 1)$
2	Local Clustering	$M_i \sim \frac{1}{2}N_i(N_i - 1)$
3	Global Integration	$d(i, j) \ll \frac{N}{2}$

Table 2.1: General properties of a small-world network for any vertices  $i, j$ .

### Algorithm

Now, how do we construct a network that exhibits these properties? The standard approach has since become known as the Watts-Strogatz Algorithm (31), and produces a network as a random variable sampled from a distribution having three degrees of freedom, namely:

1. Graph order,  $N$
2. Initial vertex degree,  $K$
3. Rewiring probability,  $p$

Given some choice of these three parameters, the algorithm proceeds as follows: Begin with a 2-regular cycle graph of order  $N$ . Next, introduce clustering by adding edges between successive pairs of vertices  $i$  and  $i + k \forall 1 \leq k \leq \frac{K}{2}$ , producing a  $K$ -regular circulant graph of size  $M = \frac{1}{2}NK$ . Finally, iterate through each edge in the graph, and with probability  $p$ , rewire it from the original end-vertex to any other vertex, chosen at random such that a new edge is created that does not already exist in  $E$ . This introduces long-range connections into the network in a parametrically controlled manner.

Note that this is a summary of the overall process; for the full algorithm we refer the reader to Algorithm 1. As an example of this process, see Figure 2.7.

#### 2.3.2 Analysis

Given this algorithmic approach to constructing a network exhibiting the small-world phenomenon, how can we analyse how the graph topology depends on the three parameters

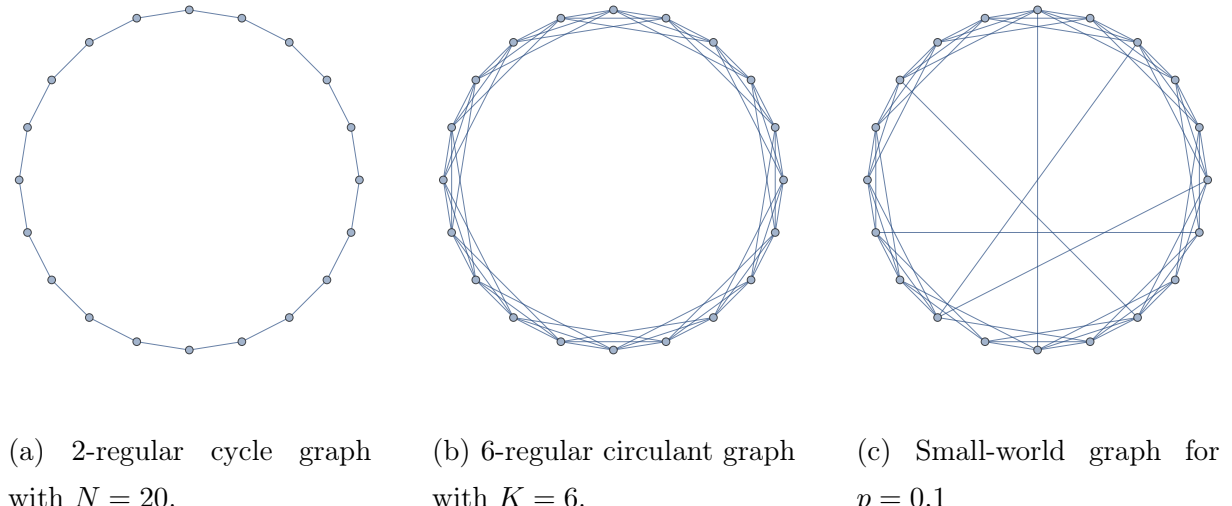


Figure 2.7: Procedure of the Watts-Strogatz Algorithm for constructing a small-world network.

$N$ ,  $K$  and  $p$ ? Or, in other words, how do they affect the edge density, local clustering and global integration of the network?

What we shall see is that there is an inherent tension between these network properties; they are not independent (34). Therefore, increasing global integration, above some limit, necessitates a decrease in clustering, and vice versa; we shall explore this in more detail in the following sections.

### Measures of Small-worldness

In order to do so, we must first introduce a quantitative measure of small-worldness that can be calculated for a given network. Watts and Strogatz's original proposal was to make use of the average clustering,  $C$ , and path length,  $L$ . Since these quantities are dependent on the number of rewired edges in the network, what they did was to consider the *normalized* clustering and path length, relative to those of the regular network,  $\tilde{C} = \frac{C(p)}{C(0)}$  and  $\tilde{L} = \frac{L(p)}{L(0)}$ . They found that the small-world effect was most pronounced when  $\tilde{C} \sim 1$  and  $\tilde{L} \ll 1$ . Furthermore, they showed that this occurred for a small rewiring probability,  $p \sim 0.1$ .

Following on from this work, a number of other quantities have been proposed to classify small-worldness. These include: the *small-world coefficient*,  $\sigma(p)$ , of Humphries *et al* (55),

$$\sigma(p) = \frac{C(p)}{C(1)} \times \frac{L(1)}{L(p)}, \quad (2.19)$$

the *small-world measurement*,  $\omega(p)$ , of Telesford *et al* (35),

$$\omega(p) = \frac{L(1)}{L(p)} - \frac{C(p)}{C_{lattice}}, \quad (2.20)$$

as well as the *network efficiency*,  $E(G)$ , of Latora and Marchiori (56),

$$E(G) = \frac{1}{\frac{1}{2}N(N-1)} \sum_{i=1}^N \sum_{j=i+1}^N \frac{1}{d(i,j)}, \quad (2.21)$$

$$E_{local} = \frac{1}{N} \sum_{i=1}^N E(G_i \setminus \{i\}). \quad (2.22)$$

Here, 2.19 uses a normalization relative to an equivalent random graph (of equal size and order), denoted  $C(1)$  and  $L(1)$ . It results in a curve with a peak at the value of  $p$  giving maximal small-worldness, and we can categorise a given network as small-world if  $\sigma > 1$ .

However, Telesford argues that this is too broad a definition, since it can include ‘almost’ random graphs, where  $p \sim 1$ , and therefore proposed 2.20 as an alternative. In this case, the clustering coefficient is compared to that of an equivalent lattice graph, generated according to the latticization algorithm of Sporns (33). This produces a monotonically increasing function of  $p$  from  $-1$  (regular) to  $+1$  (random), with  $\omega(p) \approx 0$  corresponding to  $\max(\sigma(p))$ , and small-worldness in the range  $-0.5 \leq \omega(p) \leq 0.5$ .

Finally, the global and local efficiencies, 2.21 and 2.22, were proposed as generalizations of the average path length and clustering coefficients, respectively. These are based on the inverse distance, which is particularly useful for weighted and (possibly) disconnected graphs. Here,  $E(G_i \setminus \{i\})$  is the efficiency of the subgraph of neighbours of vertex  $i$ , and also provides a measure of the robustness, or fault tolerance, of the network.

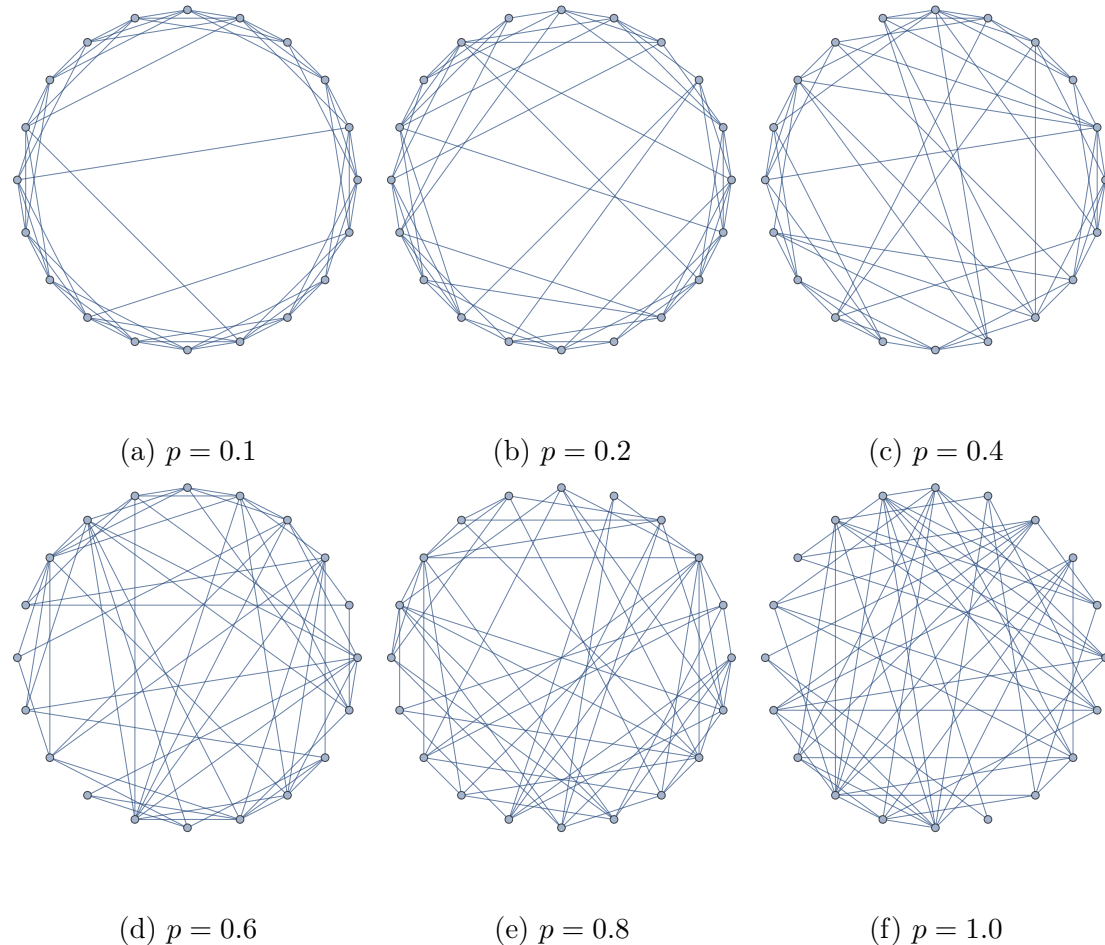


Figure 2.8: Results of the Watts-Strogatz Algorithm for  $N = 20$ ,  $K = 6$ , and varying  $p$ .

### Rewiring Probability

It is most instructive to first consider varying the rewiring probability for a given  $N$  and  $K$ . In doing so, one observes a clear transition from a completely regular, circulant, graph for  $p = 0$  to a completely disordered, random, graph for  $p = 1$ , in which every edge has been randomly rewired (see Figure 2.8). In the context of physical systems, this gives us a controlled mechanism for introducing disordered interactions into an otherwise ordered network.

Due to the random rewiring process, the algorithm produces one possible realization of the

ensemble,  $g \in G_{WS}(N, K, p)$ . Since this is a probabilistic process, the number of rewired edges is a random variable with expectation value,  $\frac{1}{2}NKp$ .

Now, referring to Figures 2.7 and 2.9, we can observe the tradeoff between clustering and path length as  $p$  is varied between 0 and 1. For small values of  $p$ , we have  $\mathcal{O}(1)$  rewired edges. Thus, we find that the neighbourhood structure of the graph is relatively undisturbed, yet even such a few rewired edges are able to significantly reduce the average path length of the network. For  $p \sim 1$ , we have  $\mathcal{O}(M)$  rewired edges; the network has lost its clustering and the average path length has reached a minimum.

### Network Size and Order

Having discussed the effect of rewiring probability on the small-world properties of a given network, we now need to consider the effects of the choice of  $N$  and  $K$ .

Together, these two parameters affect not only the initial clustering and path length, but also the edge density, since

$$\rho(G_{WS}) = \frac{K}{N-1}. \quad (2.23)$$

This effect is illustrated in Figure 2.10. From 2.10a and 2.10b, we observe that, for a given  $N$ , increasing  $K$  leads to a large number of longer range connections, thereby permanently increasing the clustering, but also decreasing the path length (consider a complete graph with  $L = 1$ ) to the point where random rewirings do not have a significant effect.

One could argue that this is a beneficial situation, since in principle we are interested in networks with high clustering and low path length. However, considering 2.10c, we can see that even small changes in edge density lead to large changes in the small-worldness coefficient; indeed, maximising  $\sigma$  requires very sparse graphs, such that neighbourhoods are small relative to the rest of the network,  $N_i \ll N$ , and therefore most neighbourhoods are independent of one another. This also ensures that the long-range rewirings have a larger effect on the global integration of the network, by joining otherwise disconnected neighbourhoods; something that wouldn't be observed in a dense network.

Finally, we can see, from 2.10d, that even for a fixed edge density, the small-worldness

decreases with a subsequent decrease in  $N$  and  $K$ , to the point where, for  $N \sim \mathcal{O}(10)$ , there is no observed peak in small-worldness near  $p \sim 1$ . This is due to smaller  $K$  resulting in lower clustering, and the smaller  $N$  resulting in a lower path length, since  $L(0) \propto N$  but  $L(1) \propto \ln N$  (31).

## 2.4 Summary

In this chapter, we began by reviewing basic concepts of algebraic graph theory, with particular reference to graph representations and measures. Most importantly, we considered the adjacency matrix representation, and measures of clustering and distance. We then used these to describe relevant graph architectures such as the complete, circulant and random graphs.

These concepts allowed us to formally describe the small-world phenomenon in terms of associated graph measures; specifically, the edge density, average local clustering coefficient and average shortest path length. From here we introduced the Watts-Strogatz Algorithm as a mechanism for constructing such a network based on three parameters: the graph order, vertex degree and rewiring probability. We then introduced quantitative measures, such as the small-worldness coefficient, and used these to analyse the dependence of the network clustering and integration on the three model parameters.

Most significantly, we observed a strong dependence on the network order,  $N$ , and corresponding edge density,  $\rho$ ; networks exhibiting the most small-worldness had a very low edge density,  $\rho < 0.1$ , as in Figure 2.10d. This is particularly important for our work, since obtaining such a low edge density in a network requires a large number of vertices,  $N \geq \mathcal{O}(10^2)$ . To see why this is the case, note that from 2.23,  $N \propto \frac{K}{\rho}$ , and that  $K \geq 2$  otherwise the network is a cycle graph with no clustering. Therefore to achieve just  $\rho = 0.1$  requires  $N \sim 200$ . As we shall discuss in Chapter 4, this poses a significant computational challenge for simulating a small-world network of quantum particles, due to the exponential growth in the size of the network Hilbert space.

**Algorithm 1** Watts-Strogatz Algorithm

1. Define parameters:

$$\text{Vertex number: } N \in \{n \in \mathbb{Z} : 3 \leq n\} \quad (2.9)$$

$$\text{Vertex degree: } D \in \{d \in 2\mathbb{Z} : 2 \leq d \leq N - 1\} \quad (2.10)$$

$$\text{Rewiring probability: } P \in \{p \in \mathbb{R} : 0 \leq p \leq 1\} \quad (2.11)$$

 2. Define network as a simple, undirected,  $D$ -regular, cycle graph of  $N$  vertices:

$$\text{Graph: } G = \{V, E\} \quad (2.12)$$

$$\text{Vertex Set: } V = \{v \in \mathbb{Z}_N\} \quad (2.13)$$

$$\text{Edge Set: } E = \left\{ \{v, v + d\} \mid \forall v, v + d \in V : 1 \leq d \leq \frac{D}{2} \right\} \quad (2.14)$$

 3. For each edge length,  $1 \leq d \leq \frac{D}{2}$ 

 (a) For each vertex,  $1 \leq v \leq N$ 

 i. Define a random variable of real numbers on the unit interval,  $X_{\mathbb{R}} : \Omega_{\mathbb{R}} \rightarrow \mathbb{R}$ :

$$\Omega_{\mathbb{R}} \equiv \{r \in \mathbb{R} : 0 \leq r \leq 1\} \quad (2.15)$$

 ii. Sample  $\omega_{\mathbb{R}} \in \Omega_{\mathbb{R}}$  randomly and uniformly.

 iii. If  $X_{\mathbb{R}}(\omega_{\mathbb{R}}) \leq P$ , then rewire with probability  $P$ :

 A. Define the random variable of all edges not in the graph,  $X : \Omega_E \rightarrow \mathbb{Z}^2$ , where:

$$\Omega_E \equiv \{\{v, \omega\} \notin E : \omega \in V\} \quad (2.16)$$

 B. Sample an edge  $\omega_E \in \Omega_E$  randomly and uniformly

 C. Remove the element  $\{v, v + d\}$  from the edge set,

$$E \rightarrow E' = E \setminus \{v, v + d\} \quad (2.17)$$

 D. Add the element  $\{v, \omega_E\}$  to the edge set,

$$E \rightarrow E' = E \cup \{v, v + \omega_E\} \quad (2.18)$$

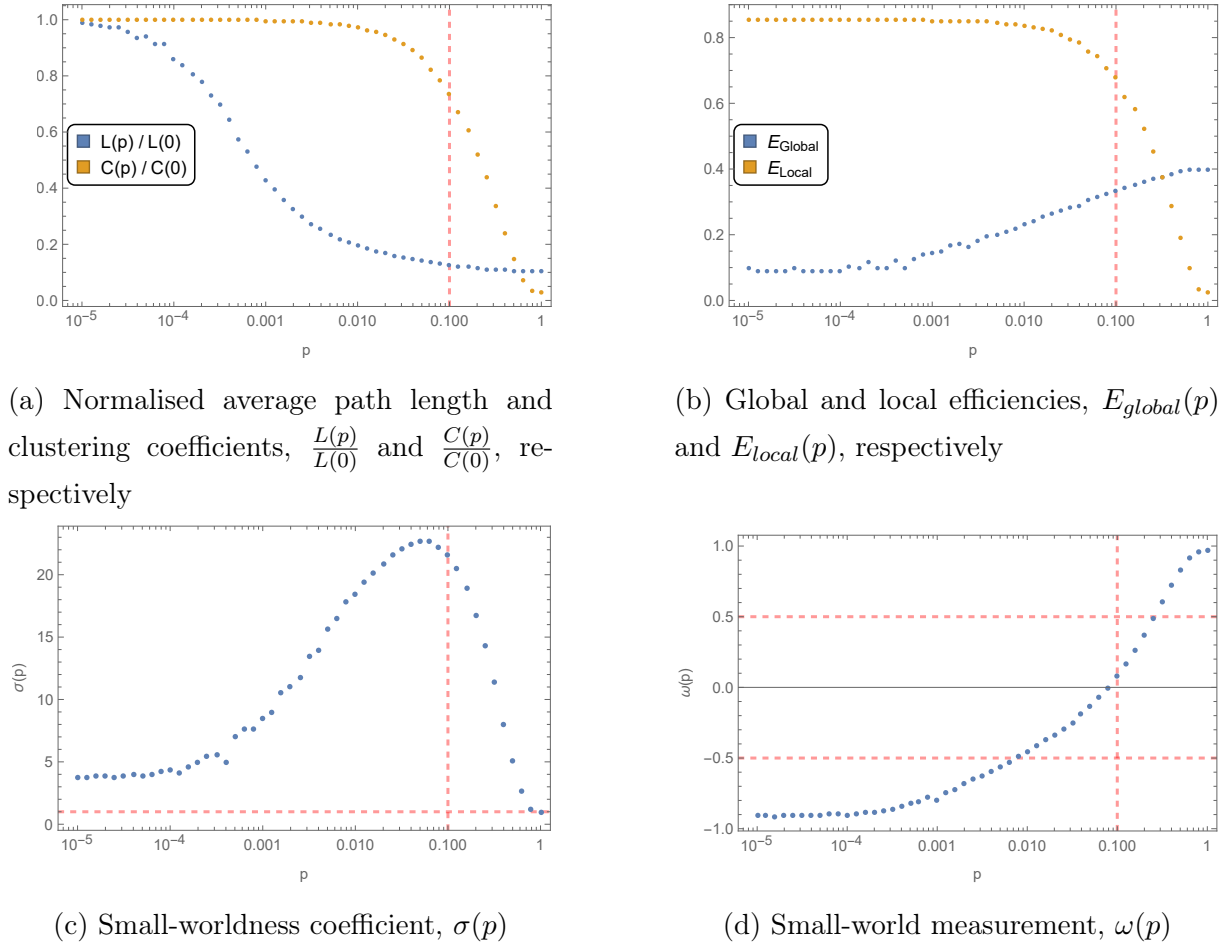


Figure 2.9: Small-worldness parameters as functions of the rewiring probability, averaged over 50 realizations for  $N = 1000$  and  $K = 20$ . The vertical dashed lines at  $p = 0.1$  indicate the value at which the small-worldness is maximised, according to Watts and Strogatz. The horizontal lines in 2.9c and 2.9d show the regions in which the authors classify the networks as small-world.

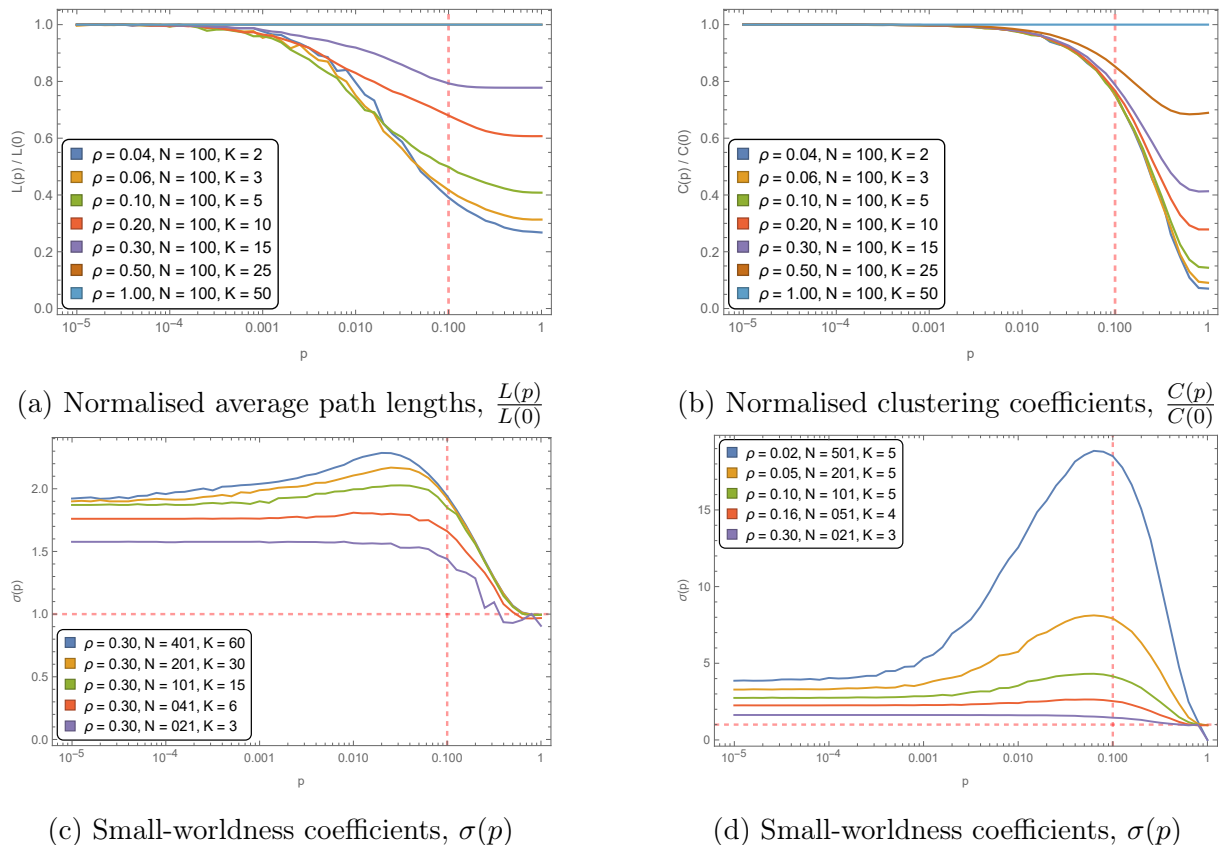


Figure 2.10: Small-worldness parameters as functions of the rewiring probability, averaged over 50 realizations, showing dependence on the number of vertices and edges in the networks.

# Chapter 3

---

## Diagnostics of Quantum Chaos

---

...it may happen that small differences in the initial conditions produce very great ones in the final phenomena.

---

Henri Poincaré in *Science and Method* (57)

### 3.1 Introduction

As an early proponent of chaos, Poincaré is widely attributed as the first to make the observation that certain, nonlinear, systems exhibit ‘sensitive dependence on initial conditions’, which is now known to be the defining feature of chaos in classical dynamical systems (58). Informally, this is the statement that two trajectories with infinitesimally close initial conditions, evolving in time in a system with chaotic dynamics, will diverge exponentially such that their initial relationship cannot be reconstructed. The implication is that there exist classes of classically deterministic systems in which long-term prediction is impossible.

The modern foundations of chaos theory are generally attributed to the American math-

ematician and meteorologist Edward Lorenz, following his 1963 discovery of the strange attractor in toy models of atmospheric weather systems (3), as well as his 1972 talk ‘Predictability; Does the Flap of a Butterfly’s wings in Brazil Set Off a Tornado in Texas?’ (4).

Early work on quantum chaos leading up to the turn of the century focused on quantum mechanical systems whose corresponding classical analogues are chaotic; the aim being to understand the emergence of deterministic (classical) chaos from the underlying quantum mechanisms (5; 6). Notable examples include the single-particle Hamiltonian ‘billiards’ models, such as those of Sinai (59) and Bunimovich (60). Berry (6) went so far as to assert that ‘there is no quantum chaos, in the sense of exponential sensitivity to initial conditions...’, and suggested such studies be termed *quantum chaology*.

Most recently, there has been a significant confluence of interest within the condensed matter, high energy theory, and even theoretical computer science communities, regarding chaotic behaviour in strongly-correlated quantum many-body systems; the focus of our current work. These are systems that do not have corresponding classical analogues, or are far from (semi-)classical regimes; much emphasis has been placed on identifying novel signatures of chaos in such systems, which are of central importance to our analysis of quantum spin networks.

In this chapter, we introduce the diagnostics representing the current state of the art in this rapidly evolving field. Section 3.2 discusses approaches from random matrix theory to studying the eigenvalue spectra of quantum systems. In section 3.3, we introduce a number of modern diagnostics of quantum chaos that have received much worldwide attention in recent years, and are used to identify chaotic behaviour at different time and energy scales.

## 3.2 Spectral Statistics

The first studies of large, random, matrices, pioneered by Wigner (61) and Dyson (62), were attempts at modelling the energy levels of heavy atomic nuclei. Since then, random

matrix theory has been applied to many fields ranging from number theory to statistical, and condensed matter, physics; see Mehta's seminal text on the subject, to which we refer in the following discussion (40).

In trying to understand the large Hamiltonian matrices describing complex nuclei, Dyson introduced a class of random matrices, known as the Gaussian ensembles; the most-studied models being:

1. The *Gaussian Orthogonal Ensemble* (GOE) of  $N \times N$  real, symmetric matrices; representing Hamiltonians with time-reversal symmetry.
2. The *Gaussian Unitary Ensemble* (GUE) of  $N \times N$  complex, Hermitian, matrices; representing Hamiltonians without time-reversal symmetry.
3. The *Gaussian Symplectic Ensemble* (GSE) of  $N \times N$  quaternionic, Hermitian, matrices; representing Hamiltonians with time-reversal, but without rotational, symmetry.

In each of these ensembles, each distinct element  $M_{ij}$  of the  $N \times N$  matrix  $\mathbf{M}(N)$  is a random variable independently and identically distributed (iid) according to a normal (Gaussian) distribution,  $M_{ij} \sim \mathcal{N}(\mu, \sigma^2)$ , generally with zero mean ( $\mu = 0$ ) and unit variance ( $\sigma^2 = 1$ ). Furthermore, each element is either real (GOE), complex (GUE) or quaternionic (GSE), and the matrices themselves are invariant under orthogonal (GOE), unitary (GUE) or symplectic group (GSE) conjugation. Physically, this means that the ensembles model systems with their respective aforementioned symmetries. As examples of each of these, consider the matrices shown in 3.1. Note that the quaternionic form of the  $2N \times 2N$  symplectic matrix in 3.1c is given by the block structure

$$\begin{pmatrix} z_0 + iz_1 & z_2 + iz_3 \\ iz_3 - z_2 & z_0 - iz_1 \end{pmatrix},$$

where  $z_i$  are  $N \times N$  matrices, with  $z_0$  real symmetric and  $z_1, z_2$  and  $z_3$  real anti-symmetric.

Wigner's insight was that these matrix ensembles represent universal features of generic quantum systems having sufficiently large Hamiltonians. In order to discuss this, we first introduce some terminology. Given a generic quantum system, we can describe the

$$\begin{array}{c}
 \left( \begin{array}{cccc}
 -0.525384 & -0.495722 & -0.523965 & -0.951493 \\
 -0.495722 & -1.46075 & 1.1065 & -0.247524 \\
 -0.523965 & 1.1065 & 1.82595 & 0.82336 \\
 -0.951493 & -0.247524 & 1.02336 & -0.581046
 \end{array} \right) \quad (a) \text{ GOE}(4) \\
 \left( \begin{array}{cccc}
 1.62846 - 0.1i & 0.522773 - 0.93918i & -0.472166 - 0.334425i & 0.15871 - 0.860236i \\
 0.522773 - 0.93918i & -0.233212 + 0.1i & 0.183185 - 0.059916i & -1.21941 - 0.366297i \\
 -0.472166 - 0.334425i & 0.183185 - 0.059916i & 0.729626 + 0.1i & 0.076883 - 0.698327i \\
 0.15871 - 0.860236i & -1.21941 - 0.366297i & 0.076883 - 0.698327i & -0.0868632 + 0.1i
 \end{array} \right) \quad (b) \text{ GUE}(4) \\
 \left( \begin{array}{cccc}
 -0.589117 - 0.1i & -0.479315 - 0.631202i & 0.146692 - 0.435651i & 0.146692 - 0.435651i \\
 -0.479315 - 0.631202i & 1.05741 + 0.1i & -0.146692 + 0.435651i & -0.146692 + 0.435651i \\
 0.146692 - 0.435651i & -0.146692 + 0.435651i & 0.588117 + 0.1i & 0.479315 + 0.631202i \\
 0.146692 - 0.435651i & -0.0868632 + 0.1i & 0.479315 - 0.631202i & 1.05741 + 0.1i
 \end{array} \right) \quad (c) \text{ GSE}(4)
 \end{array}$$

Figure 3.1: Examples of  $4 \times 4$  random matrices drawn from the Gaussian ensembles.

dynamics, in the Heisenberg representation, as an eigenvalue problem using the associated Hamiltonian matrix,

$$H\psi_j = \lambda_j \psi_j, \quad (3.1)$$

with energy spectrum,

$$\sigma(H) = \{\lambda_j \mid 1 \leq j \leq N\}, \quad (3.2)$$

where the number of eigenvalues and eigenvectors,  $N$ , is equal to the dimension of the system Hilbert space. We use  $\lambda_j \equiv E_j$  interchangeably to represent the eigenvalue of the  $j$ -th energy level.

This is standard linear algebra, and we may also apply it to any random matrices  $\mathbf{M}(N) \sim \text{GXE}(N)$  (the X is a placeholder for either O, U or S of the aforementioned ensembles) we may generate. Computing a histogram (counting the number of eigenvalues within some range) of the spectrum  $\sigma(\mathbf{M})$ , we obtain the *eigenvalue density*, which we denote  $\rho(\lambda)$ .

This eigenvalue density of the Gaussian matrices was observed to follow what is now referred to as the Wigner *semi-circle distribution*, given by

$$\rho(\lambda; r, a) = \begin{cases} \frac{2}{\pi r} \sqrt{1 - (\frac{\lambda-a}{r})^2} & |\lambda - a| \leq r \\ 0 & |\lambda| > r \end{cases}, \quad (3.3)$$

where all the eigenvalues are found in the compact region centered at some  $a$  and bounded by some  $a \pm r$ ; see Figure 3.2a for an example, which is indeed semi-circular.

However, this distribution is insufficient to characterise specific system behaviour; it does not differentiate between the three ensembles, and so the same semi-circular density is observed regardless of the symmetries in the system. Therefore, to obtain more information from the spectra, Wigner introduced the *eigenvalue spacing distribution*, by ordering the eigenvalues from smallest to largest,  $0 \leq \lambda_1 \leq \dots \leq \lambda_N$ , and considering the distances

between consecutive (neighbouring) energy levels,  $s_j = \lambda_{j+1} - \lambda_j$ , resulting in

$$P(s, N) = \frac{1}{N-1} \sum_{j=1}^{N-1} \delta(s - s_j). \quad (3.4)$$

It is important that, at this point, we normalise the distribution by *unfolding* the spectrum relative to the mean spacing,  $\langle s \rangle = \frac{1}{N} \sum_{j=1}^N s_j$ . In other words, when studying the spectrum of some Hamiltonian matrix, and wanting to compare it to that of an appropriate random matrix, we are only interested in the relative spacing distribution. We are not concerned with absolute differences in the spacings, and so by dividing by the mean spacing for the distribution, we ensure that we are able to correctly compare with that of a Gaussian random matrix. More precisely, this is done to remove finite-size effects on the local density of states (15), so that the unfolded spacing distribution of a generic Hamiltonian may be compared directly to that of one of the Gaussian ensembles.

Now, if the spacings for a given system are completely random and uncorrelated, one would expect to see a Poisson distribution,

$$P_{\text{Poisson}}(s) = e^{-s}. \quad (3.5)$$

However, Wigner found that, for the Gaussian matrices, the spacings were in fact correlated, and followed distributions of the form,

$$P_\beta(s) = C_\beta s^\beta e^{-a_\beta s^2}, \quad (3.6)$$

now known as the *Wigner Surmise*, or Wigner-Dyson distribution, following Dyson's classification as follows:  $\beta = 1, 2, 4$  for GOE, GUE and GSE, respectively, and  $C_\beta$  and  $a_\beta$  are normalisation constants, resulting in:

$$P_{\text{GOE}}(s) = \frac{\pi}{2} s^1 e^{-\frac{\pi}{4} s^2}, \quad (3.7)$$

$$P_{\text{GUE}}(s) = \frac{2^5}{\pi^2} s^2 e^{-\frac{4}{\pi} s^2}, \quad (3.8)$$

$$P_{\text{GSE}}(s) = \frac{2^{18}}{3^6 \pi^3} s^4 e^{-\frac{2^6}{3^2 \pi} s^2}, \quad (3.9)$$

as shown in Figure 3.2b. Therefore, by calculating the spacing distribution for the (unfolded) spectrum of a given Hamiltonian matrix, we can calculate the goodness-of-fit to each of these distributions, and find the model that most accurately represents the system.

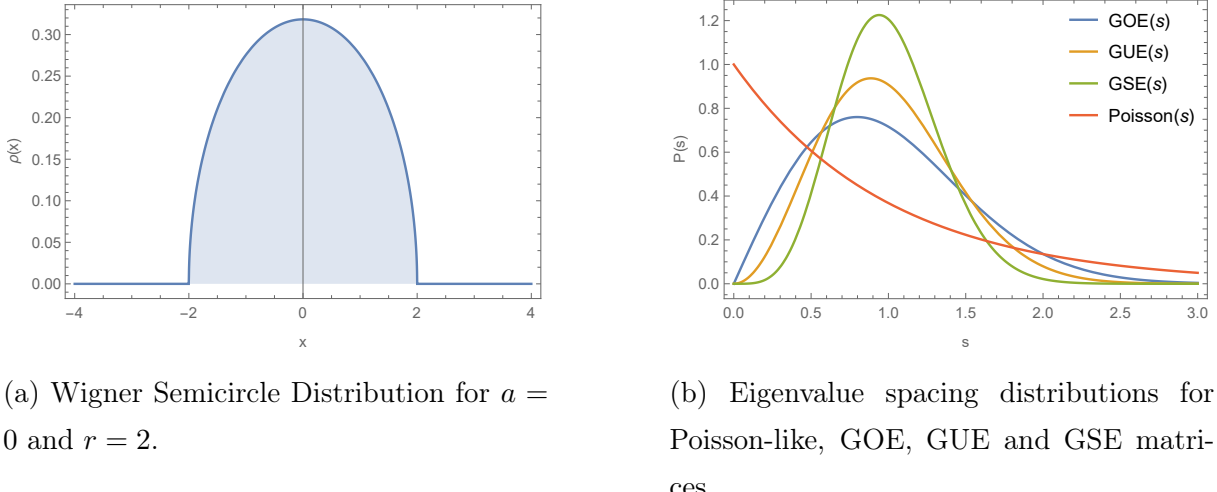


Figure 3.2: Graphs illustrating the distribution of eigenvalues and eigenvalue spacings in Gaussian random matrices.

However, besides telling us about the presence of time-reversal or rotational symmetries in the system, what more can we learn from this fitting, and what does a Poisson-like distribution imply? Most significantly, in the context of semiclassical quantum chaology, are two conjectures which relate the eigenvalue spacing distribution of the underlying quantum system to the regular or chaotic features of the corresponding classical dynamics (63); the Berry-Tabor (BT) and Bohigas-Giannoni-Schmidt (BGS) conjectures, proposed in 1977 (64) and 1984 (65), respectively.

**Conjecture 3.1. *Berry-Tabor Conjecture*** *If the corresponding classical dynamics is completely integrable, then  $P(s)$  exists and is equal to the waiting time between consecutive events of a Poisson process,  $P(s) = e^{-s}$  (63).*

**Conjecture 3.2. *Bohigas-Giannoni-Schmidt Conjecture*** *If the corresponding classical dynamics is **not** completely integrable, i.e. chaotic, then  $P(s)$  exists and is equal to the consecutive level spacing distribution of a suitable Gaussian ensemble of Hermitian random matrices (63).*

The physical argument for this difference between Poisson-like (integrable), and random

matrix-like (chaotic) behaviour is as follows (66): If the spacings between energy levels are uncorrelated, then any transitions between eigenstates are possible and depend only on the (negative exponential of the) change in energy, as for a Poisson process, and the system is said to be integrable.

If, on the other hand, the spacing distribution,  $P(s)$ , peaks at  $s \neq 0$  and  $P(s \rightarrow 0) \rightarrow 0$ , as for the Gaussian ensembles, this is indicative of *level repulsion*, or *avoided level crossings*. In this case, small energetic transitions of the eigenstates are avoided, there is not an infinite number of conserved charges, and the system is said to be non-integrable. Again, Figure 3.2b indicates this behaviour; notice how the Gaussian ensemble distribution peak near  $s \approx 1$ , and drop to zero at  $s = 0$ , indicative of level repulsion of small energy separations.

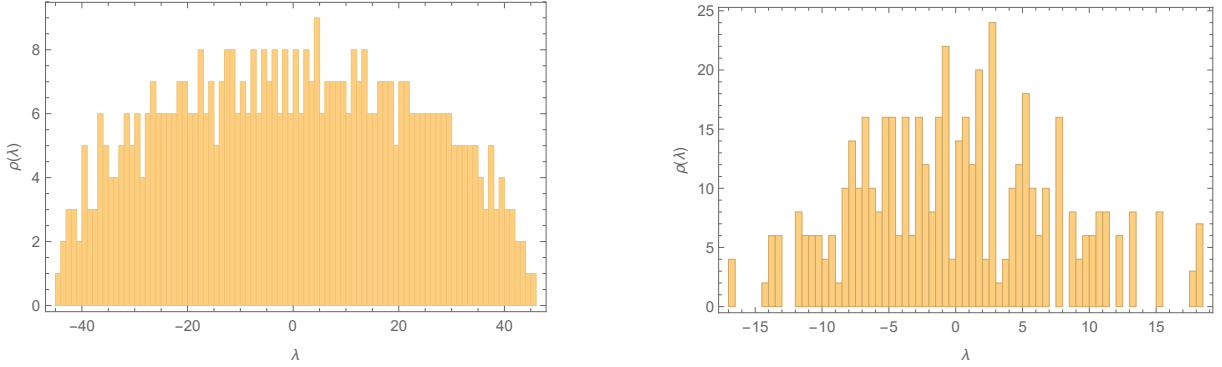
Although still without formal proof, the BGS conjecture has been verified experimentally, and computationally, in a large number of systems, to the point where it is widely regarded as a defining signature of quantum chaos (67).

### 3.2.1 r-Statistic

The spectral unfolding method has proven successful in a large number of studies of semi-classical systems. However, recent work (66; 68) has argued that this method introduces inaccuracies in strongly-correlated many-body systems, due to (i) the appearance of band structures in the density of states, as well as (ii) exponential growth of the system Hilbert space.

As an example of (i), consider Figure 3.3. Notice the semi-circular form of the GUE density of states, whereas the random spin network contains distinct bands of high and low density. Regarding point (ii), adding a single particle to such a system doubles the number of eigenvalues, making it difficult to compare systems that have similar numbers of particles (and, intuitively, very similar physics), but very different eigenvalue distributions.

For this reason, the authors mentioned above propose using the ratio of consecutive spac-



(a) Density of states histogram for a matrix of GUE(512).

(b) Density of states histogram for a random graph Ising model with 512 eigenvalues (see Chapter 4).

Figure 3.3: Graphs illustrating the structure of the density of states for the GUE and a random spin network of equal size.

ings for such systems,

$$r_j = \frac{\min\{s_j, s_{j-1}\}}{\max\{s_j, s_{j-1}\}} \quad (3.10)$$

$$= \min\left\{\frac{s_j}{s_{j-1}}, \frac{s_{j-1}}{s_j}\right\}. \quad (3.11)$$

This quantity, colloquially referred to as the *r-statistic*, was introduced by Oganyesan and Huse (69) as a means of circumventing the unfolding procedure, since the ratio of spacings is independent of the mean spacing. Significantly, the distribution  $P(r)$  has been shown to yield more precise results than  $P(s)$  in comparison with Gaussian ensemble distributions, for many-body quantum systems.

Bogomolny *et al* (68) then went on to derive analytic expressions for the distributions of the Gaussian ensembles (see 3.7 - 3.9) in terms of the r-statistic,

$$P_\beta(r) = \frac{1}{Z_\beta} \frac{(r + r^2)^\beta}{(1 + r + r^2)^{1+(3/2)\beta}}, \quad (3.12)$$

with  $\beta = 1, 2, 4$  as before, and  $Z_\beta$  normalisation constants:

$$\begin{aligned} Z_{GOE} &= \frac{2^3}{3^3}, \\ Z_{GUE} &= \frac{2^2\pi}{3^{9/2}}, \\ Z_{GSE} &= \frac{2^2\pi}{3^{13/2}}. \end{aligned}$$

From here it is relatively straightforward to test whether a system is chaotic (according to the BGS conjecture), by computing the goodness-of-fit of the difference,  $\delta P(r) = P_{num}(r) - P_\beta(r)$ , between the numeric results and the analytic predictions of the Wigner surmise. This is, in principle, very similar to the fitting procedure discussed for the spacing distribution, but simply avoids the unfolding procedure.

A subsequent method for classifying the system dynamics as either Poisson-like or random matrix-like was proposed by Kollath *et al* (66), and utilised in further studies, such as (15). This approach is based on calculating the mean r-statistic,  $\langle r \rangle$ , for a given Hamiltonian, and comparing to the expectation values of the pure distributions:

$$\begin{aligned} \mathbb{E}(r_{Poisson}) &= 2 \ln 2 - 1 & \approx 0.386, \\ \mathbb{E}(r_{GOE}) &= 4 - 2\sqrt{3} & \approx 0.536, \\ \mathbb{E}(r_{GUE}) &= \frac{2\sqrt{3}}{\pi} - \frac{1}{2} & \approx 0.603, \\ \mathbb{E}(r_{GSE}) &= \frac{32\sqrt{3}}{15\pi} - \frac{1}{2} & \approx 0.676. \end{aligned}$$

This gives a more systematic approach, and one that is particularly suited to probing systems that exhibit an integrability-chaos transition, since we may plot  $\langle r \rangle$  as a function of the disorder parameter and observe the transition. Ideally, we would like to observe a transition as shown in Figure 3.4. Here, we begin with an integrable system, having a Poisson-like  $\langle r \rangle$ , at small values of some parameter that introduces disorder into the system. As this parameter grows, we can see a transition from Poisson-like to GUE-like, in this case.

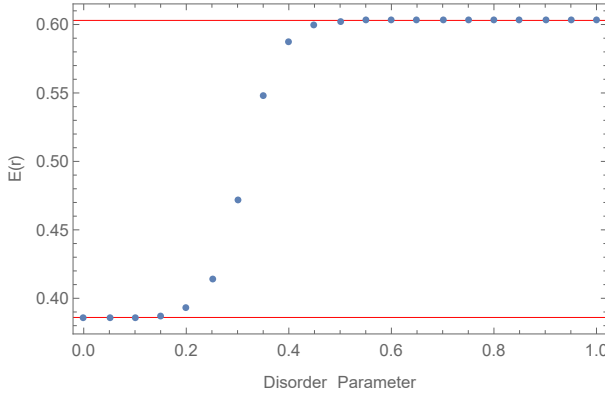


Figure 3.4: Hypothetical plot of  $\langle r \rangle$  as a function of a parametric disorder term in a given system.

### 3.3 Time-Dependent Signatures

Analysis of the spectral statistics of the system Hamiltonian matrix provides insight into the behaviour of the system in the long-time limit, since the matrix itself is time-independent and encodes all the system dynamics in the energy eigenstates.

However, there has been significant recent interest in studying the early-time behaviour of strongly-correlated quantum systems; the aim being to understand quantum information scrambling and its relation to black hole physics. This work was directly influenced by Kitaev’s introduction of the SYK model (20), and his connection of the (growth rate of) *out-of-time-order correlation functions* (OTOC) to Lyapunov exponents of classical chaos (70). For this reason, we now introduce the two diagnostics that are most studied in this context, the OTOC and *spectral form factor* (SFF).

#### 3.3.1 Out-of-time-order Correlation Functions

First introduced by Larkin and Ovchinnikov in 1969 in the context of superconductivity (37), for a single particle in a chaotic potential, the four-point OTOC has been the subject of significant research interest in recent years, see (7; 18; 20; 23; 39; 42; 47; 70; 71; 72; 73; 74; 75; 76) amongst many others.

This interest was precipitated by the relation to the butterfly effect of classical chaos and the Loschmidt echo of quantum systems, particularly following the MSS bound on the growth of chaos in thermal quantum systems (18). Most important was the observation that the OTOC could be used to show that the SYK saturates this MSS bound, and is in fact a maximally chaotic system.

Given a set of *local operators*,  $V$  and  $W$  in some Hilbert space  $\mathcal{H}$ , the OTOC is defined by the expectation value of the squared commutator,

$$C_\beta(t) \equiv -\langle [W(t), V(0)]^2 \rangle, \quad (3.13)$$

$$= -\frac{1}{Z} \sum_{n=1}^{2^N} e^{-\beta E_n} \langle \psi_n | [W(t), V(0)]^2 | \psi_n \rangle, \quad (3.14)$$

where  $\langle \dots \rangle$  represents the thermal average at inverse temperature  $\beta = \frac{1}{T}$ ,  $Z = \sum_{n=1}^{2^N} e^{-\beta E_n}$  is the thermal partition function of the Hamiltonian with  $2^N$  eigenstates given by  $E_n$  and  $\psi_n$ .

Now, what is the physical significance of this quantity, and how is it related to a Lyapunov exponent? While there is not a purely quantum notion of exponential divergence of trajectories in phase space as in classical mechanics, a heuristic argument made by MSS (18), and summarised by Hashimoto *et al* (39), is as follows: Consider  $W(t) = x(t)$  and  $V(0) = p(0)$  as position and momentum operators, respectively. Then, in the semiclassical limit, we may replace the commutator with the Poisson bracket

$$\begin{aligned} [x(t), p(0)] &\rightarrow i\hbar\{x(t), p(0)\} \\ &= i\hbar \frac{\delta x(t)}{\delta x(0)} \\ &\sim e^{\lambda t} \end{aligned}$$

giving a Lyapunov exponent of  $\lambda$  for a classically chaotic system. Thus, the squared commutator should grow as  $\sim \hbar^2 e^{2\lambda t}$ . It is worth noting that, unlike in a classical system, the OTOC does not grow without bound, but saturates at the Ehrenfest time,  $t_E$ , beyond which the wave function has spread throughout the entire system, and cannot grow any further. In this regard, the MSS bound proposes an upper limit on the growth of chaos as  $\lambda \leq 2\pi k_B T / \hbar$  (18).

Now, how do we go about calculating this quantity in a computationally efficient manner? Expanding the commutator, and writing  $W = W(t)$  and  $V = V(0)$ ,

$$\begin{aligned} [W, V]^2 &= (WV - VW)^2 \\ &= (WV - VW)(WV - VW) \\ &= WVWV + VWVW - WVWV - VWVV \end{aligned}$$

Since the operators  $W$  and  $V$  are both Hermitian and Unitary,

$$\begin{aligned} WVWV &= \mathbb{I} = VWVV \\ \therefore [W, V]^2 &= WVWV + VWVW - 2\mathbb{I} \end{aligned}$$

Substituting into (3.14),

$$\begin{aligned} C_\beta(t) &= -\frac{1}{Z} \sum_{n=1}^{2^N} e^{-\beta E_n} \langle \psi_n | WVWV + VWVW - 2\mathbb{I} | \psi_n \rangle \\ &= \frac{1}{Z} \sum_{n=1}^{2^N} e^{-\beta E_n} \{ \langle \psi_n | 2\mathbb{I} | \psi_n \rangle - \langle \psi_n | WVWV | \psi_n \rangle - \langle \psi_n | VWVW | \psi_n \rangle \} \\ &= \frac{1}{Z} \sum_{n=1}^{2^N} e^{-\beta E_n} \{ 2 - \langle \psi_n | (WVW)V | \psi_n \rangle - \langle \psi_n | V(WVW) | \psi_n \rangle \} \end{aligned} \quad (3.15)$$

Noting that the term  $WVW$  is also Hermitian and Unitary, and considering the third term in (3.15), we have that

$$\langle \psi_n | V(WVW) | \psi_n \rangle = \langle \psi_n | (WVW)V | \psi_n \rangle^*$$

This is the complex-conjugate of the second term in (3.15). Therefore, written in terms of the real and imaginary components,

$$\begin{aligned} \langle \psi_n | (WVW)V | \psi_n \rangle &= \text{Re}(\langle \psi_n | (WVW)V | \psi_n \rangle) + i \text{Im}(\langle \psi_n | (WVW)V | \psi_n \rangle) \\ \langle \psi_n | (WVW)V | \psi_n \rangle^* &= \text{Re}(\langle \psi_n | (WVW)V | \psi_n \rangle) - i \text{Im}(\langle \psi_n | (WVW)V | \psi_n \rangle) \end{aligned}$$

Thus, (3.15) reduces to

$$C_\beta(t) = \frac{1}{Z} \sum_{n=1}^{2^N} e^{-\beta E_n} 2[1 - \text{Re}(\langle \psi_n | W(t)V(0)W(t)V(0) | \psi_n \rangle)] \quad (3.16)$$

Two further simplifying approximations may be made by taking the (i) high temperature, and (ii) large  $N$  limits, as follows. Since we are interested in the fastest possible growth of  $C(t)$ , the infinite temperature limit is reasonable; taking  $\beta = 0$  results in  $Z = 2^N$  and  $e^{-\beta E_n} = 1$ , therefore

$$C_0(t) = \frac{1}{2^N} \sum_{n=1}^{2^N} 2[1 - \text{Re}(\langle \psi_n | W(t)V(0)W(t)V(0) | \psi_n \rangle)] \quad (3.17)$$

Now, it is still computationally intensive to sum over all  $2^N$  eigenstates of  $H$  (1). Approximation (ii) to (3.17) may be made by employing the notion of *quantum typicality* in the large  $N$  limit (77): Given some general system, properties of the full statistical ensemble can be well-approximated by those of a single, random, pure state,  $|\psi\rangle$ . Thus, the expectation value term in (3.17) may be written as

$$\frac{1}{2^N} \sum_{n=1}^{2^N} \langle \psi_n | \hat{O} | \psi_n \rangle = \frac{1}{2^N} \langle \psi | \hat{O} | \psi \rangle + \varepsilon(|\psi\rangle) \quad (3.18)$$

$$\Rightarrow \left| \text{Tr}(\hat{O}) - \langle \psi | \hat{O} | \psi \rangle \right| = 2^N |\varepsilon(|\psi\rangle)| \quad (3.19)$$

where  $\varepsilon(|\psi\rangle)$  is the error associated with the approximation. This concept is made precise by *Levy's Lemma* (78; 79),

**Lemma 3.3.1** (Levy's Lemma). *Given a Lipschitz-continuous function  $f : \mathbb{S}^d \rightarrow \mathbb{R}$  defined on the  $d$ -dimensional hypersphere,  $\mathbb{S}^d$ , and a point  $\psi \in \mathbb{S}^d$  chosen uniformly at random,*

$$P[|\langle f \rangle - f(\psi)| \geq \epsilon] \leq 2 \exp\left\{ \frac{-(d+1)\epsilon^2}{9\pi^3\eta^2} \right\} \quad (3.20)$$

where  $\eta$  is the Lipschitz constant of  $f$ , given by  $\eta = \sup |\nabla f|$ .

Taking  $\mathcal{H} \sim \mathbb{S}^d$ , with states  $\psi \in \mathcal{H}$ , and local operators that satisfy Lipschitz-continuity, the error between  $\langle f \rangle$  and the function value of a randomly chosen state,  $f(\psi)$ , decreases exponentially as a function of the Hilbert space dimension,  $d = 2^N$ . Therefore, (77; 80)

$$\lim_{d \rightarrow \infty} \text{Tr}(\hat{O}) = \langle \psi | \hat{O} | \psi \rangle \quad (3.21)$$

Therefore, in the high-temperature and large Hilbert space dimension limits,

$$C_0(t) \approx 2[1 - \text{Re}(\langle \psi | (W(t)V(0)W(t)V(0)) | \psi \rangle)] \quad (3.22)$$

$$= 2[1 - \text{Re}(\langle \psi_2 | \psi_1 \rangle)] \quad (3.23)$$

where the second line is obtained by simply defining the inner product of the operated states:

$$\begin{aligned} |\psi_1\rangle &= V(0)W(t)|\psi\rangle \\ |\psi_2\rangle &= W(t)V(0)|\psi\rangle \end{aligned}$$

Furthermore, in the Heisenberg representation, the operators themselves evolve by the action of the system Hamiltonian,  $H$ , as follows,  $W(t) = e^{iHt}W(0)e^{-iHt}$ . By diagonalisation we can decompose the Hamiltonian into the eigenvector and (diagonal) eigenvalue matrices,  $Q$  and  $D$ , respectively:  $H = QDQ^\dagger$ . Thus the operator evolution can be written as  $W(t) = Q^\dagger e^{iDt} Q W(0) Q e^{-iDt} Q^\dagger$ , and therefore

$$|\psi_1\rangle = V(0)Q^\dagger e^{iDt} Q W(0) Q e^{-iDt} Q^\dagger |\psi\rangle \quad (3.24)$$

$$|\psi_2\rangle = Q^\dagger e^{iDt} Q W(0) Q e^{-iDt} Q^\dagger V(0) |\psi\rangle \quad (3.25)$$

### 3.3.2 Spectral Form Factor

While the OTOC has proven to be an effective diagnostic of early-time chaos and information scrambling in certain models, previous studies of systems able to transition between integrability and chaos (81), have uncovered a tension between the OTOC and typical RMT diagnostics. In part, this is a reflection of the nature of the two sets of tools; the OTOC captures early time, quantum mechanical features of the model whereas RMT captures late time, statistical features. To reconcile these two observations, in the context of black hole information scrambling, the authors of (1) proposed the SFF as an alternative diagnostic. As the analytically-continued thermal partition function, the SFF,  $g(t, \beta)$ , has two desirable properties: (i) at late times it displays RMT behaviour and (ii) because it has a quantum mechanical flavor, it is closer to the OTOC description of quantum chaos than standard RMT measures.

Concretely, we compute the *annealed* SFF (1),

$$g(t; \beta) = \frac{\langle |Z(\beta, t)|^2 \rangle_J}{\langle Z(\beta) \rangle_J^2} \quad (3.26)$$

where  $\langle \cdot \rangle_J$  is the disorder-averaged expectation value over the ensemble of randomly connected networks, and the partition functions are given by:

$$Z(\beta, t) = \text{Tr}(e^{-\beta H - iHt}), \quad (3.27)$$

$$Z(\beta) = \text{Tr}(e^{-\beta H}). \quad (3.28)$$

The notion of annealing is imposed by taking the disorder average over the numerator and denominator separately; this may be compared to the *quenched* SFF, in which the disorder average is taken over the ratio,

$$g(t; \beta) = \left\langle \left| \frac{Z(\beta, t)}{Z(\beta)} \right|^2 \right\rangle_J \quad (3.29)$$

As argued by Cotler *et al* (1), the advantage of using the annealed SFF is that it only requires a finite number of replicas in analytic calculations, whereas the quenched SFF requires an arbitrary number of replicas. However, in the infinite temperature ( $\beta \rightarrow 0$ ) limit,  $Z(\beta = 0) = \sum_{n=1}^{2^N} 1 = 2^N$  and both the annealed and quenched SFFs become equal, reducing to

$$g(t; 0) = \frac{1}{2^N} \langle |Z(0, t)|^2 \rangle_J. \quad (3.30)$$

Now, we may simplify the calculation of the magnitude of the partition function,  $|Z(0, t)|^2$ , so as to make it computationally tractable:

$$\begin{aligned} |Z(0, t)|^2 &= Z(0, t)Z(0, t)^\dagger \\ &= \text{Tr}(e^{-iHt}) \text{Tr}(e^{iHt}) \\ &= \sum_{m=1}^{2^N} \sum_{n=1}^{2^N} \langle \psi_n | e^{-iHt} | \psi_n \rangle \langle \psi_m | e^{iHt} | \psi_m \rangle \\ &= \sum_{m=1}^{2^N} \sum_{n=1}^{2^N} e^{-iE_n t} \langle \psi_n | \psi_n \rangle e^{-iE_m t} \langle \psi_m | \psi_m \rangle \\ &= \sum_{m=1}^{2^N} \sum_{n=1}^{2^N} e^{i(E_m - E_n)t}. \end{aligned}$$

Here, the  $E_n$  and  $E_m$  are the  $2^N$  eigenvalues of the Hamiltonian matrix,  $H$ . Since the double summation considers all pairwise differences between the eigenvalues twice, we

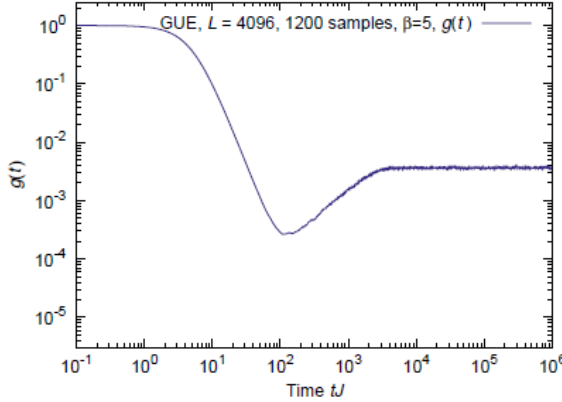


Figure 3.5: Log-log plot of  $g(t; \beta = 5)$  for random matrices sampled from the GUE of dimension  $2^{12}$ . Image reproduced from (1).

may simplify  $g(t; 0)$  to:

$$g(t; 0) = \frac{1}{2^N} \left\langle 2^N + 2 \sum_{m=1}^{2^N-1} \sum_{n=m+1}^{2^N} \cos(E_m - E_n)t \right\rangle_J \quad (3.31)$$

Now that we are able to calculate the SFF efficiently using just the Hamiltonian eigenvalues, we may consider how it can be used to diagnose (potentially) chaotic behaviour of a many-body system. For illustrative purposes, consider the SFF for GUE random matrices in Figure 3.5.

In the case of a chaotic system, the SFF exhibits several characteristics, and most importantly, three primary regimes: a smooth *dip*, a linear *ramp* and a constant *plateau*. The dip is smooth, with minimal noise or random fluctuations, and decreases to a minimum at the *dip time*,  $t_d$ . From this point the curve begins to fluctuate, but the size of such fluctuations is attenuated by the disorder averaging. The length of the ramp is then given by the difference between the dip time and the plateau time,  $t_p$ , at which the curve reaches an almost constant value, the long-time average of  $g(t; \beta)$ .

Now, what do these quantities tell us about the behaviour of the system? While the eigenvalue spacing distribution from RMT gives information on the nearest-neighbour spacings, at small energy separations, the SFF probes correlations between all energy levels, and therefore gives information about larger energy separations (1).

In particular, the  $t$  parameter in  $g(t)$  determines the scale of energy differences being probed; the origin of the ramp at intermediate timescales is due to level repulsion between well-separated eigenvalues, an indicator of chaos similar to that observed at small energy differences in the nearest neighbour spacing distribution. Specifically, Cotler *et al* observed that, for chaotic systems such as the SYK model,  $t_d$  and  $t_p$  both increase with system size  $N$ , but that  $t_p$  grows faster than  $t_d$ , leading to the length of the ramp growing proportionally to  $N$ . Additionally, at late times beyond  $t_p$  only individual energy levels,  $E_n = E_m$ , have an effect on  $g(t)$ , giving the height of the plateau (as the late-time average value of  $g(t)$ ), in terms of the eigenvalue degeneracies, providing information on internal symmetries of the system,

$$\langle g(t) \rangle_t = \frac{\sum_E N_E^2}{2^N}, \quad (3.32)$$

where  $N_E$  is the degeneracy of eigenvalue  $E$ .

### 3.4 Summary

In summary, we have introduced several state of the art methods for diagnosing chaos in many-body quantum systems. We began with a discussion of the origins of quantum chaos from random matrix theory, as first studied by Wigner, Dyson, Berry and others. This led us to consideration of the statistical distribution of energy levels as a primary signature of chaos, in the form of the nearest-neighbour eigenvalue spacing distribution; the central conclusions here being the Berry-Tabor and Bohigas-Giannoni-Schmit conjectures: that the eigenvalue statistics of integrable systems follow a Poisson distribution, while those of chaotic systems follow the Wigner surmise distributions of Gaussian random matrices. This led to the notion of the  $r$ -statistic as a more precise measure of the eigenvalue statistics for systems that may transition between integrability and chaos.

From here, we considered two modern signatures that have been introduced recently; the out-of-time-order correlator and the spectral form factor. The former is a fully quantum measure that captures the growth of system-wide correlations over time, and therefore provides information on early-time chaotic behaviour and quantum information scrambling. Due to its relation to the Lyapunov exponent of classical chaos, it is understood

that chaotic systems experience exponential growth of the OTOC at early times. This has been studied extensively since the introduction of the SYK model in 2015. However, further studies have also uncovered a tension between the OTOC and RMT results for known systems, which lead to the introduction of the spectral form factor as a measure over intermediate timescales that captures both quantum and statistical effects over larger energy scales.

# Chapter 4

---

## Quantum Small Worlds

---

We must know. We will know!

---

David Hilbert (82)

### 4.1 Introduction

This chapter introduces the central results of this thesis. The topology of a quantum spin network is generalized using concepts from graph theory. In particular, the Watts-Strogatz Algorithm is utilised to construct a small-world network of quantum spins. The evolution of the system is then analysed using tools from quantum chaos theory. The generalized model is verified by reproducing known spin systems, including the Ising and Heisenberg models.

Programming language	Wolfram Mathematica 11.3 (8 local kernels)
Operating system	Windows 10 Home 64-bit
Processor (CPU)	Intel Core i7-4720HQ @ 2.6GHz (8 logical cores)
Memory (RAM)	Asus 16384MB DDR3L @ 1.6GHz (2 × 8192MB)
Memory (SSD)	Samsung 850 EVO 250GB @ 540/520 MB/s R/W

Table 4.1: System hardware and software specifications.

## 4.2 Methodology

In this section, we detail the computational procedure followed in modeling and analysing our quantum small world networks. For reference, all simulations were performed on a system having the following hardware and software specifications:

Due to exponential dependence of the Hamiltonian matrix size on the number of particles in the system, simulating many-body quantum systems is a significant technological challenge for classical computing. As such, state-of-the-art methods for maximising system size typically involve a combination of: (i) approximation techniques for reducing the matrix size, using (ii) statically-typed, compile-time programming languages, running on (iii) massively-parallel high-performance or supercomputing clusters.

Therefore, it would be reasonable to question the use of the system whose specifications are described in Table 4.1. The ideal scenario would be to run all computations in C, using the Intel Math Kernel Library (MKL) and Message Passing Interface (MPI, for parallel computing), on a local cluster such as the Centre for High-Performance Computing (CHPC) or UCT High-Performance Computing (HPC) cluster.

However, achieving this performance has significant developmental overheads, particularly since this is a novel project for the QGaSlab research group. Hence, as a preliminary investigation, it was decided that the rapid prototyping and convenience afforded by a dynamically-typed, runtime, language, such as Mathematica on a local machine, were more important than the ability to access (marginally) larger system sizes.

Regarding the actual code implementation, a Mathematica package was written to en-

capsulate and organise the necessary algorithms and functions; the file, “QuantumSmallWorlds.m” is attached and discussed in the following subsections.

### 4.2.1 Network Initialisation

What are the degrees of freedom of the system, and what variables must we fix? From the Watts-Strogatz algorithm, the network topology is defined by the three variables for number of particles, rewiring probability and neighbour coupling length,  $N$ ,  $p$  and  $k$ , respectively. These define our graph adjacency matrix,  $A$ , that can be fed into the spin interaction Hamiltonian. Subsequently, we can introduce additional disorder by: (i) weighting each edge randomly by sampling from some distribution, (ii) considering anisotropy in the interactions in each direction;

$$J^\mu = \{J^x A_{ij}^x, J^y A_{ij}^y, J^z A_{ij}^z\} \quad (4.1)$$

Now, as will be shown in the following subsection, the size of the Hamiltonian matrix scales as  $2^N \times 2^N$  with the  $N$  number of particles. This represents a significant bottleneck due to the memory and computational requirements in storing and manipulating matrices of this size.

As an example, a Hamiltonian of 15 particles contains  $2^{15} \times 2^{15} \sim \mathcal{O}(10^9)$  elements, each of which is a complex number of 2 64-bit floating point numbers. This equates to a memory requirement of 16GB, which increases by a factor of 4 with each additional particle added, and exceeds the capabilities of our current hardware, without considering the additional memory needed to manipulate and perform the numerical eigenvalue decomposition. For this reason, we are in principle limited to systems of  $N \leq 14$ , and realistically to  $N < 12$  for reasonably time-efficient computations.

Now, this poses a problem, since as we saw in Chapter 2, we ideally need  $N > 200$  to maximise the small-worldness of the network. Furthermore, for systems of  $N \sim \mathcal{O}(10)$ , we have only a small number of  $\mathcal{O}(10)$  edges that may be rewired, meaning that the system becomes too sensitive to the potential variations in using a probabilistic rewiring parameter  $p$ . For this reason, we propose a slight modification to the Watts-Strogatz

algorithm, replacing the rewiring probability with a parameter  $r$  that instead fixes the number of rewirings applied to the network. This allows us to directly control the number of random couplings from  $0 \leq r \leq NK$ .

### 4.2.2 Hamiltonian Construction

Having defined the connectivity, we must next assign a spin particle to each site in the network. It is possible to consider any spin- $s$  particle, given by the spin matrices:

**Definition 4.1.** We define the  $d$ -dimensional *spin operators*  $\mathbf{S}^x, \mathbf{S}^y, \mathbf{S}^z$  as follows, where  $s$  is the particle spin and  $b_j \equiv \sqrt{(s+j)(s+1-j)}$ , and we set  $\hbar = 1$  (83):

$$\mathbf{S}^x = \frac{1}{2} \begin{bmatrix} 0 & b_j & 0 & 0 & \cdots & 0 \\ b_j & 0 & b_{j-1} & 0 & \cdots & 0 \\ 0 & b_{j-1} & 0 & b_{j-2} & 0 & \vdots \\ \vdots & 0 & \ddots & \ddots & \ddots & 0 \\ 0 & \cdots & & & \ddots & b_{-j+1} \\ 0 & \cdots & 0 & 0 & b_{-j+1} & 0 \end{bmatrix} \quad (4.2)$$

$$\mathbf{S}^y = \frac{1}{2} \begin{bmatrix} 0 & -ib_j & 0 & 0 & \cdots & 0 \\ ib_j & 0 & -ib_{j-1} & 0 & \cdots & 0 \\ 0 & ib_{j-1} & 0 & -ib_{j-2} & 0 & \vdots \\ \vdots & 0 & \ddots & \ddots & \ddots & 0 \\ 0 & \cdots & & & \ddots & -ib_{-j+1} \\ 0 & \cdots & 0 & 0 & ib_{-j+1} & 0 \end{bmatrix} \quad (4.3)$$

$$\mathbf{S}^z = \begin{bmatrix} s & 0 & 0 & 0 & \cdots & 0 \\ 0 & s-1 & 0 & 0 & \cdots & 0 \\ 0 & 0 & s-2 & 0 & 0 & \vdots \\ \vdots & 0 & & & & 0 \\ 0 & \cdots & 0 & 0 & \cdots & 0 \\ 0 & \cdots & 0 & 0 & 0 & -s \end{bmatrix} \quad (4.4)$$

Note that  $\mathbf{S}^z$  is diagonal in this choice of basis; this is referred to as the computational basis (84). In other words, the eigenvectors of  $\mathbf{S}^z$  form an orthonormal basis for the space  $\mathbf{H}^d$ ,  $\mathbf{e}_j^i = \delta_j^i$ , giving the  $j$ -th elements of the  $i$ -th eigenvector, with associated eigenvalues  $\alpha^i = \mathbf{S}_{ii}^z$ .

However, for the purposes of this investigation, we consider the simplest case using two-level (qubit) spin particles at each site, with spin operators given by the Pauli matrices:

$$\begin{aligned} \sigma^1 &= \begin{bmatrix} 0 & 1 \\ 1 & 0 \end{bmatrix} \\ \sigma^2 &= \begin{bmatrix} 0 & -i \\ i & 0 \end{bmatrix} \\ \sigma^3 &= \begin{bmatrix} 1 & 0 \\ 0 & -1 \end{bmatrix} \end{aligned}$$

Then, each spin matrix operating at site  $i$  is defined by repeated tensor products with the identity matrix,  $\sigma^0 \equiv \mathbb{I}_2$ , as follows ( $\hbar = 1$ ):

$$\mathbf{S}_i^\mu = \bigotimes_{n=1}^{i-1} \sigma^0 \otimes \sigma^\mu \otimes \bigotimes_{n=i+1}^N \sigma^0 \quad (4.5)$$

### Spin-Exchange Interaction

The two-point spin exchange interaction between two particles is simply given by the matrix product of the associated spin operators;  $\mathbf{S}_i^\mu \times \mathbf{S}_j^\mu$ . Therefore, we may define the

spin exchange Hamiltonian as follows:

$$H_{s-e} = \sum_{i=1}^n \sum_{j=1}^n \sum_{\mu=1}^3 J_{ij}^\mu \mathbf{S}_i^\mu \mathbf{S}_j^\mu \quad (4.6)$$

where the elements of the coupling matrix,  $J_{ij}^\mu$ , encode the adjacency matrix and edge weightings, as described above.

### External Field Interaction

We may now introduce an interaction with an external magnetic field. In general, we could imagine a system in which the field has different values at each site, and in any of the  $x, y, z$  directions, which could be written as follows:

$$H_d = \sum_{i=1}^n \sum_{\mu=1}^3 h_i^\mu \sigma_i^\mu \quad (4.7)$$

### General Hamiltonian

We may now generate the complete Hamiltonian, for a system of  $N$  particles,

$$H = H_{s-e} + H_d, \quad (4.8)$$

this is an Hermitian matrix of size  $2^N \times 2^N$ . By taking this graph theoretic approach to constructing our network Hamiltonian, we are able to generate multiple classes of systems simply through our choice of the elements of the adjacency matrix. As an illustrative example, consider the well-known networks in Figure 4.1, which we can generate through the Watts-Strogatz algorithm by selecting appropriate values for  $N$  and  $K$ , and, in the case of weighted networks, such as the Scherrington-Kirkpatrick and Sachdev-Ye models (Figure 4.1c), by introducing (Gaussian random) weightings on the edges.

Nevertheless, for the purposes of this thesis, we restrict ourselves to the unweighted networks of the Ising and Heisenberg models, and introduce long-range interactions through the rewiring probability parameter  $p$  of the Watts-Strogatz algorithm.

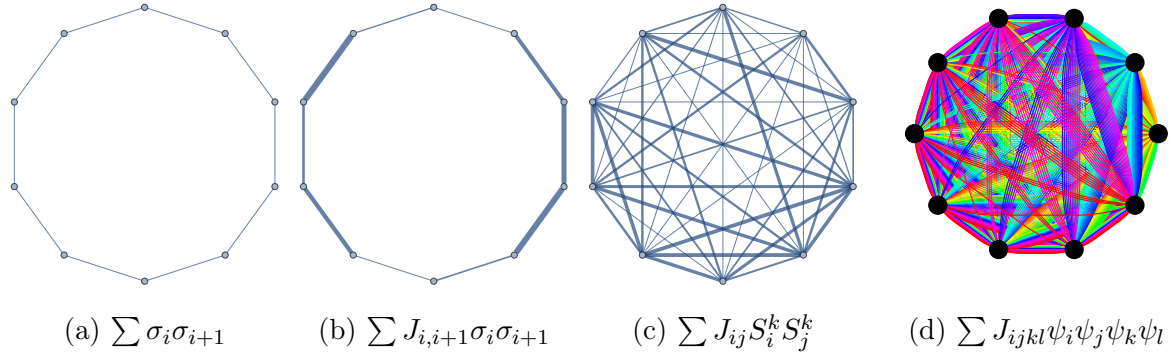


Figure 4.1: Example Spin Models

### 4.2.3 Numerical Diagonalisation

Due to the strongly-correlated nature of the long-range interactions introduced by the rewiring algorithm, it is necessary to perform exact diagonalisation on the Hamiltonian; approximation algorithms, such as DMRG, are most effective only for locally-interacting systems in which particles interact with their near neighbours. Therefore, the decomposition is performed by the Mathematica “Eigensystem” function, which implements the standard BLAS/LAPACK packages found in virtually all scientific computing languages, including Python NumPy, MATLAB, C MKL, Julia, and Fortran.

## 4.3 Analysis

We are now in a position to study our small-world spin networks, using the OTOC and SFF to diagnose the system as we transition away from integrability by adding long-range random interactions via the Watts-Strogatz algorithm.

### 4.3.1 Out-of-time-order Correlators

We begin by first examining the choice of operators from which to compute the OTOCs. Note that we will be calculating the squared commutator  $C_0^{WV}$ , which is really  $2(1 -$

$\text{Re}(OTOC)$ ), but will use the terms interchangeably. Given the expression (3.22) in terms of unitary and Hermitian operators  $W$  and  $V$ ,

$$C_0^{WV}(t) \approx 2[1 - \text{Re}(\langle \psi | (W(t)V(0)W(t)V(0)) | \psi \rangle)],$$

and noting that we are studying pure spin systems, the degrees of freedom are given by the Pauli spin operators,  $\mathbf{S}^x$ ,  $\mathbf{S}^y$  and  $\mathbf{S}^z$ . Therefore, we can write the OTOC as

$$C_0^{\mu\nu}(v, t) \approx 2[1 - \text{Re}(\langle \psi | (\mathbf{S}_v^\mu(t)\mathbf{S}_1^\nu(0)\mathbf{S}_v^\mu(t)\mathbf{S}_1^\nu(0)) | \psi \rangle)], \quad (4.9)$$

where the indices  $\mu$  and  $\nu$  select one of the  $x$ ,  $y$  or  $z$  spin operators, and the parameter  $v$  indicates the spin operator acting at vertex  $v$  in the network. Now, the quantity  $C_0^{\mu\nu}(v, t)$  probes the operator at site  $v$ , and so provides a measure of how a disturbance applied at vertex 1 spreads over the network as a function of time.

### Transverse Field Ising Chain

As an example, let us consider the transverse field, spin- $\frac{1}{2}$  Ising chain with nearest-neighbour interactions and periodic boundary conditions. In this regular case, where we do not rewire any edges, and only consider the (unit-weighted) nearest-neighbour interaction, (obtained from the Watts-Strogatz algorithm by setting  $k = 1$  and  $p = 0$ ), the adjacency matrix  $\mathbf{A}(C_N)$  is generated for the unweighted 2-regular cycle graph of order  $N$ ,  $C_N$ :

$$\mathbf{A}(C_N) = \begin{bmatrix} 0 & 1 & 0 & \cdots & 0 & 1 \\ 1 & \ddots & & & & 0 \\ 0 & & \ddots & & & \vdots \\ \vdots & & & \ddots & & 0 \\ 0 & & & & \ddots & 1 \\ 1 & 0 & \cdots & 0 & 1 & 0 \end{bmatrix} \quad (4.10)$$

In this case, with  $\mathbf{J} = \{\mathbf{0}_N, \mathbf{0}_N, J\mathbf{A}(C_N)\}$ , where  $\mathbf{0}_N$  is the  $N \times N$  zero matrix, the Hamiltonian expressions may be rewritten in the familiar form:

$$H_z = -\frac{J}{2} \left( \sum_{i=1}^{N-1} \sigma_i^z \sigma_{i+1}^z + g \sum_{i=1}^N \sigma_i^x \right). \quad (4.11)$$

By choosing the couplings  $J = g = 1$ , we are considering the critical case, where the system transitions between ferromagnetic and paramagnetic. Our reasoning for first considering this system is twofold; (i) It is a well-studied model that allows us to compare our results with those in the literature, thereby providing a benchmark of our numerics prior to our study of a novel system, and (ii) provides a simplified, integrable, model for observing the effect of the choice of operator for  $\mu$  and  $\nu$ , and understanding the behaviour of the OTOCs in integrable spin systems.

With regards to point (ii), consider as an example the plots in Figure 4.2, for each of the possible operator pairs on a regular Ising chain of  $N = 10$  vertices. The plots on the main diagonal are the pure correlators  $C_0^{xx}(v, t)$ ,  $C_0^{yy}(v, t)$  and  $C_0^{zz}(v, t)$ , while the off diagonal plots are the mixed correlators.

Our first observation from this chain of nearest-neighbour interactions is the presence of a light cone-like wavefront that propagates through the chain in all cases, with zero operator growth in the spacelike region. Within the timelike region of the wave, we see that the pattern of operator spreading differs based on the choice of operators. Of particular importance are the  $C^{xx}$  and  $C^{zz}$ , since they probe the correlations in the directions of the external field and spin-exchange interaction, respectively. The former produces a shell-like wavefront where the correlations tend to zero in the timelike region, while the latter produces a periodically oscillating light cone. These two are contrasted with the remaining OTOCs, which produce an approximately constant plateau in the timelike region. Furthermore, we note that the mixed correlators are not equivalent under an exchange of the operators ( $C_0^{XY}(v, t) \neq C_0^{YX}(v, t)$  for example), but that qualitative similarities between such pairs may be observed.

What is the physical significance of this behaviour? As discussed in Section 3.3.1, exponential early-time growth is widely regarded as an indicator of chaotic dynamics, while at late times  $C_0^{\mu\nu} \rightarrow 2$  and  $C_0^{\mu\nu} \rightarrow 0$  are indicative of scrambling and localisation of quantum information, respectively. In this sense, then, we can say that there is no scrambling of the  $\sigma^x$  operator, but that the plateau of the timelike region is a signature of scrambling, most noticeably in the case of the smooth plateau of  $C^{zx}$  in 4.2g.

We could relate this operator dependence of the scrambling behaviour to the very recently

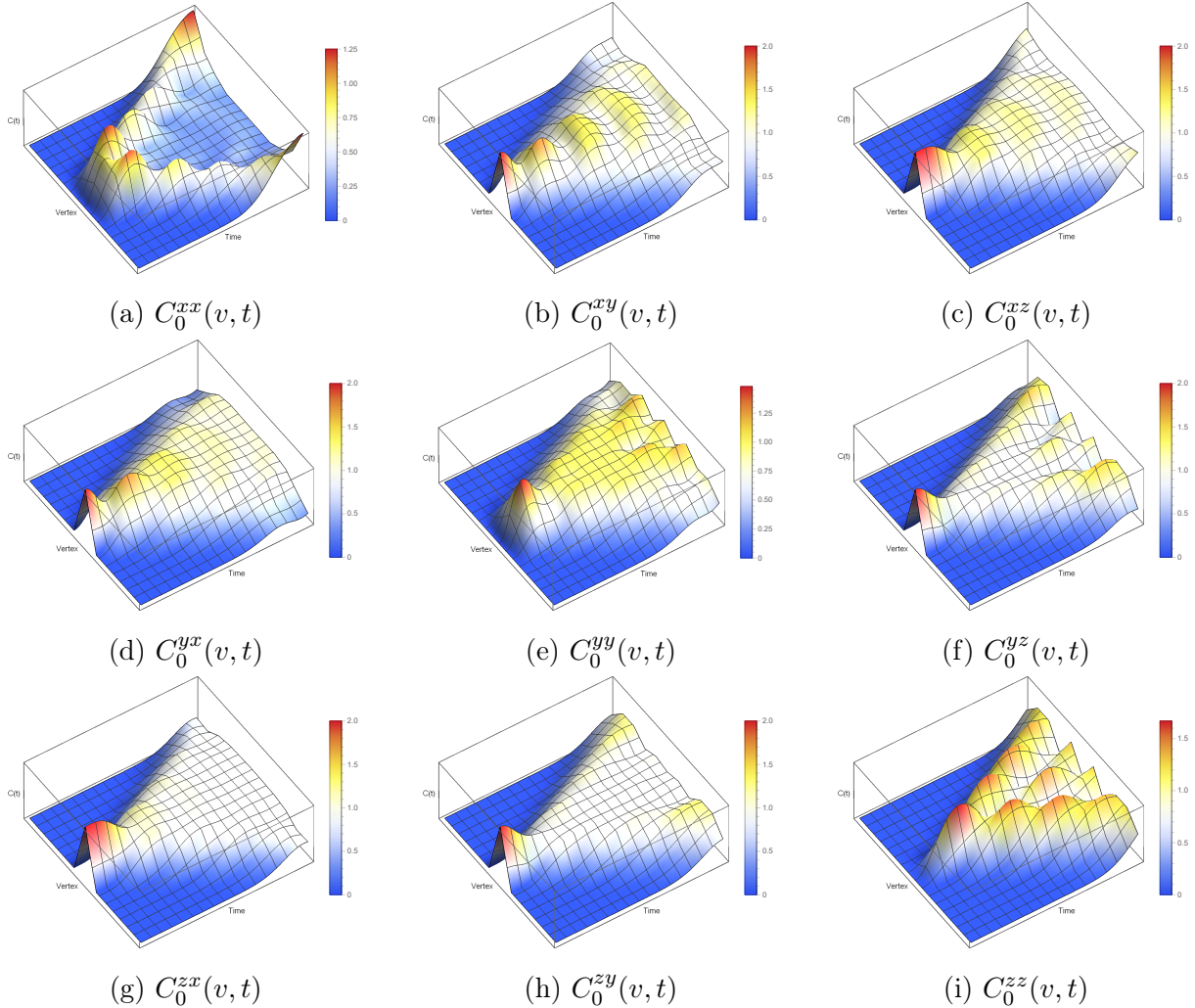


Figure 4.2: OTOCs for the Ising spin chain given by (4.11) with  $N = 10$  vertices. Each figure plots the quantity  $C_0^{\mu\nu}(v, t)$  in (4.9) as a function of time,  $t$ , and vertex position,  $v$ . These plots indicate how the different operators spread through the periodic chain following an initial perturbation applied at vertex 1.

introduced *Operator Thermalisation Hypothesis* (OTH) (85), which, in contrast to the *Eigenstate Thermalisation Hypothesis* (ETH), proposes that even in integrable theories, with highly-structured eigenvalue spectra, it is possible to observe thermalisation simply through a choice of sufficiently complex operator with which to probe the system.

Before continuing, we confirm, with regard to point (i) above, that our numerics are

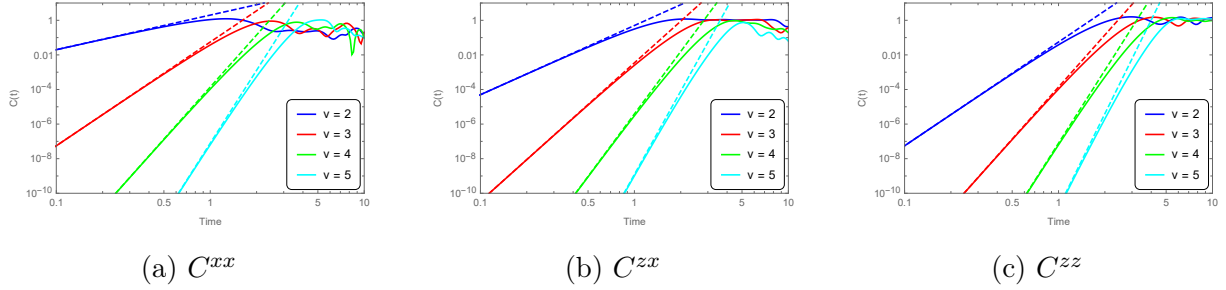


Figure 4.3: Log-Log plots of the OTOCs, for vertices 2 through 5, from Figure 4.2, focusing on the growth at early timescales. The dashed lines represent the power-law expressions given by (4.12) to (4.14).

producing accurate results. We refer to the work of Lin and Motrunich (23), in which they study the  $C^{xx}$ ,  $C^{zx}$  and  $C^{zz}$  operators for the same transverse field Ising chain. Indeed, visual comparison with Figures 4.2a, 4.2g and 4.2i does indicate that our results are qualitatively accurate. For a quantitative comparison, the researchers derived, using the Hausdorff-Baker-Campbell (HBC) expansion, the following universal power-law expressions for the early-time growth of the OTOCs as functions of vertex position, time and model couplings  $J$  and  $g$ :

$$C_0^{xx}(v, t; J, g) = \frac{2g^{2l-2}(Jt)^{4l-2}}{((2l-1)!)^2} \quad (4.12)$$

$$C_0^{zx}(v, t; J, g) = \frac{2g^{2l}(Jt)^{4l}}{((2l)!)^2} \quad (4.13)$$

$$C_0^{zz}(v, t; J, g) = \frac{2g^{2l+2}(Jt)^{4l+2}}{((2l+1)!)^2} \quad (4.14)$$

In Figure 4.3, we therefore plot, together, the early-time growth of the OTOCs from Figures 4.2a, 4.2g and 4.2i, together with the analytic results from the equations (4.12), (4.13) and (4.14). These results clearly indicate a good agreement with the analytically derived results, and match precisely with the same figures as presented by Lin and Motrunich. Additionally, these results reinforce the expected power law growth of the OTOCs for a well-known integrable system with short-range interactions.

Let us now ask the question: *What can we learn from, and about, OTOCs in an interacting many-body quantum system transitioning between completely regular and completely disordered behaviour?* Specifically, we shall examine the correlators for our quantum small-world models as the rewiring probability is varied from 0 to 1, thereby introducing disorder via long-range, random, interactions. Indeed, as we transition away from integrability, are there any cases where we observe exponential growth at early times, and how is the late time behaviour affected?

### Small-world Ising model

Completing our analysis of the transverse field Ising model, we refer to Figures 4.4 and 4.5, corresponding to the ( $K = 1$ ) nearest-neighbour and ( $K = 2$ ) next-to-nearest-neighbour interactions, respectively.

Looking at Figure 4.4, we plot the OTOCs for the network at the three rewiring probabilities,  $p = 0, 0.1$  and  $1$ , which, for the regular network of 9 vertices and edges, corresponds to 0, 1 and 9 rewired edges, respectively. From the contour plots, we observe a breakdown in the wavefront as long-range interactions are introduced into the system. However, this is understood when one considers the notion of distance in the graph, and how the causal structure is affected by the connectivity. To be precise, since the initial perturbation is applied at vertex 1, and propagates along the edges, we should consider the edge distance from vertex 1 to vertex  $i$  as a form of discrete metric on the network.

For example, in column 2, the rewiring changes the edge  $(1, 2) \rightarrow (1, 6)$ . Before rewiring,  $d(1, 2) = 1$  and  $d(1, 6) = 4$ . After the rewiring,  $d(1, 2) = 5$  and  $d(1, 6) = 1$ . The effect of this is clear in the 2D plots on the third row of the figure;  $C_0^{zz}(6, t)$  was the last to grow from zero, while after the rewiring it exhibits growth at the same time as vertex 9, while  $C_0^{zz}(2, t)$  is the furthest from vertex 1. Therefore, we should be able to recover the wavefront effect, in a sense, by plotting the contours, not based on vertex number, but on distance  $d(1, i)$ . As an example, consider Figure 4.6, where we change the order in which the vertices are plotted from  $\{1, 2, 3, 4, 5, 6, 7, 8, 9\}$  to  $\{1, 2, 9, 3, 5, 4, 6, 7, 8\}$ .

Let us look more closely at the growth curves in row 3, specifically at the initial growth

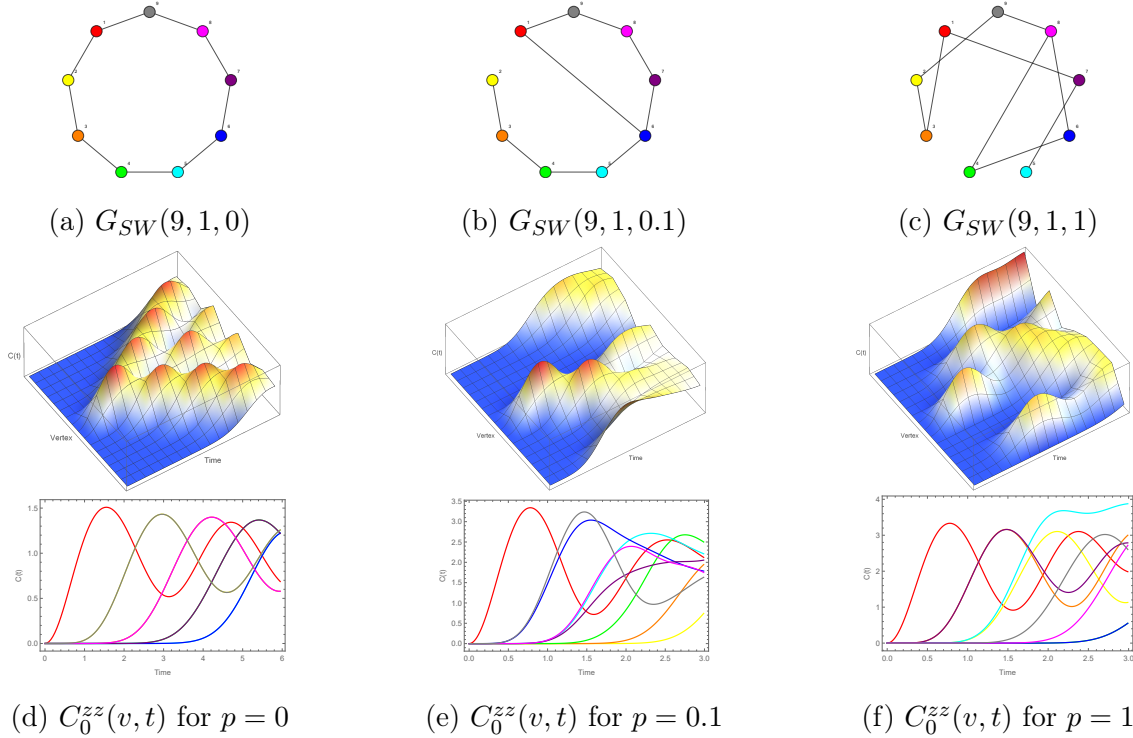


Figure 4.4: Contour and 2D plots of the OTOCs for different rewiring probabilities. Note that the colour of the curve refers to the OTOC probed at the corresponding vertex of the same colour on the graph.

phase. It is apparent that, as  $p$  increases, the most significant difference is the order in which the OTOCs for each vertex grow, depending on the distance from vertex 1. Indeed, it would appear that the time taken for the initial growth phases, and the rate of growth of the curves within this period, is not affected by the rewiring probability.

To make these observations more precise, we define the growth time,  $t_v^*$ , taken to reach the inflection point of the correlation curve for vertex  $v$ ,  $\frac{\partial^2 C_0^{zz}(v,t)}{\partial t^2}|_{t=t_v^*} = 0$ . As an illustrative example, consider the OTOCs in Figure 4.7, where the green highlighted points represent  $C_0^{zz}(v, t \leq t_v^*)$ , and the red vertical lines indicate the  $t_v^*$ . In the third plot, we plot the  $t_v^*$  as a function of the distance between vertex  $v$  and vertex 1,  $d(1, v)$ , for increasing rewiring probabilities. The linearity of the curves indicates that the relationship is indeed independent of rewiring probability.

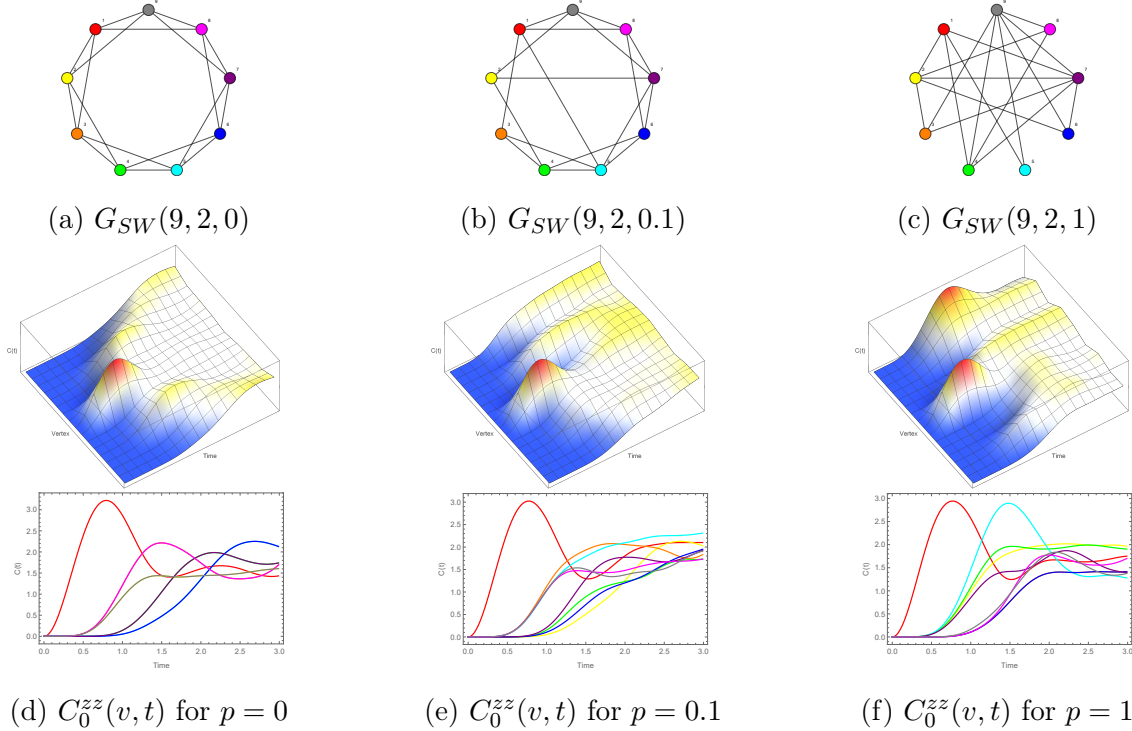


Figure 4.5: Contour and 2D plots for an Ising network of next-to-nearest-neighbour interactions for varying rewiring probabilities.

Now, most importantly, let us investigate how the rewiring probability affects the growth rate of the OTOCs. We shall do this in two ways; by (i) comparing the power-law model of (4.14), and (ii) finding best-fit curves to  $C_0^{zz}(v, t \leq t_v^*)$ .

In Figure 4.8, we plot the universal power-law curves, derived for the regular Ising chain, against the small-world networks with rewired edges. These plots indicate overall good agreement, though we do see deviations increasing with distance from vertex 1. All of the curves follow polynomial time growth that appears to decrease; the rate of growth is slower for vertices further from the initial perturbation. Regardless of rewiring probability, we do not observe exponential growth in the OTOCs.

This is confirmed by the fitted models in Figure 4.9, where we fit exponential ( $a(e^{bx} - 1)$ ) and polynomial ( $ax^b$ ) models, using nonlinear regression, to the convex regions of the OTOCs. This fitting returns the best-fit model parameters ( $a$  and  $b$ ), that maximise the

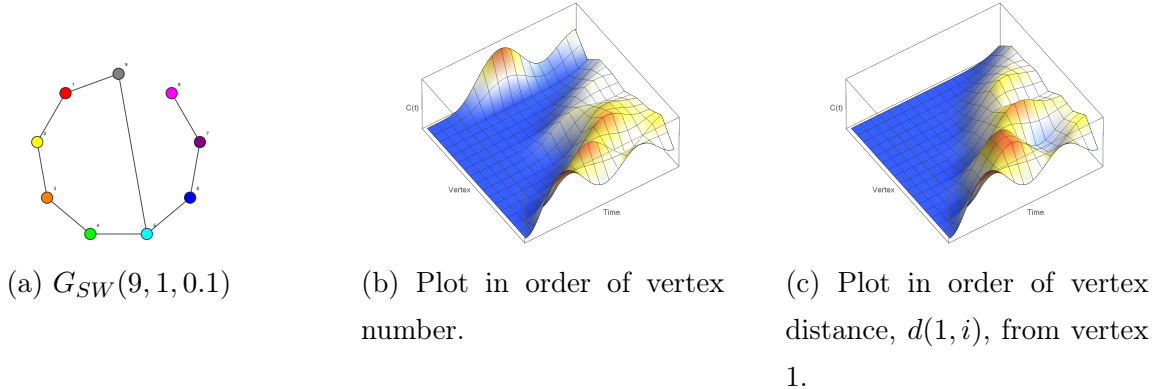


Figure 4.6: Contour plots of  $C_0^{zz}(v, t)$  using different methods of ordering the vertices.

$R^2$  goodness-of-fit statistic for each curve. After averaging over all the curves, we see that the polynomial models provide a better goodness-of-fit, indicating that they are a better estimator of OTOC growth than the best-fit exponential models. This is significant, as we do not observe a transition from polynomial-time to exponential time growth. We may therefore conclude that the OTOC does not diagnose chaos in the small-world Ising model.

Now, a similar set of observations may be made for the class of next-to-nearest neighbour networks shown in Figure 4.5. The  $\sigma_i\sigma_{i+2}$  terms of the next-to-nearest neighbour interactions reduce the overall path length, and increase the edge density, in the network. This leads to faster propagation of the correlations through the network. This interaction term also causes the system to become non-integrable. Despite this change, comparison with the power-law curves in Figure 4.10 shows that the OTOCs remain linear on the log-log plots, and therefore continue to grow in polynomial time. Indeed, we can see from these plots, in addition to those of 4.5, is that the rate of growth appears to be lower than for the  $K = 1$  case, particularly for the OTOCs of particles further from the starting site.

However, due to the increased edge density, we see that the correlations spread over more particles at each time step, leading to overall lower peak values of  $C_0^{zz}(v, t)$ . Furthermore, it can be seen that once all of the correlators have experienced a period of initial growth, they appear to fluctuate about a constant value of  $\sim 1$ . This is an indication of *quantum scrambling*; the delocalisation of the quantum information (introduced by our initial con-

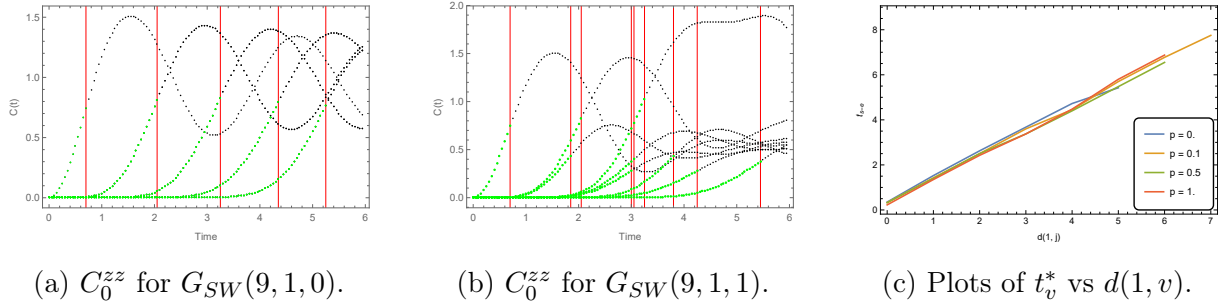


Figure 4.7: Plots indicating the initial growth periods of the OTOCs for varying rewiring probabilities. In (a) and (b), the green highlighted points indicate convexity, at times  $t \leq t_v^*$ , with the red vertical lines at  $t = t_v^*$  for each vertex  $v$ . The curves in (c) are for rewiring probabilities  $p = 0, 0.1, 0.5, 1.0$  on networks with  $N = 10$  and  $K = 1$ . For  $p \neq 0$ , each data point was obtained by taking the disorder average over 10 randomly generated networks sampled from the ensemble  $G_{SW}(10, 1, p)$ .

dition), over the system degrees of freedom due to unitary evolution. In other words, as the system evolves in time, the initial perturbation spreads via the spin-exchange interaction. The information becomes increasingly delocalised, until it is difficult to recover the initial perturbation, analogous to irreversibility in thermal processes.

Additionally, the rate at which this scrambling occurs appears to be greater for the regular network than for the small-world or random networks, though the difference between  $p = 0.1$  and  $p = 1$ , at least for this particular example, does not appear to be significant. We argue that the *scrambling rate* is dependent on the average path length of the network, which, as we have seen for small-world networks, is strongly dependent on the rewiring probability (see Figure 2.9a).

In order to quantify the scrambling rate, we need to first identify the *scrambling time*, beyond which we are unable to recover the initial state. Qualitatively, we know that this occurs when  $\text{Re}\{\langle \mathbf{S}_v^z(t) \mathbf{S}_1^z(0) \mathbf{S}_v^z(t) \mathbf{S}_1^z(0) \rangle\} \sim 0$ ; the time beyond which the operator  $\mathbf{S}_v^z(t)$  has spread sufficiently that it no longer commutes with  $\mathbf{S}_1^z(0)$ . However, we note that this is still an area of active research (86; 10), and that the random fluctuations of the correlations make the precise identification of such a time difficult.

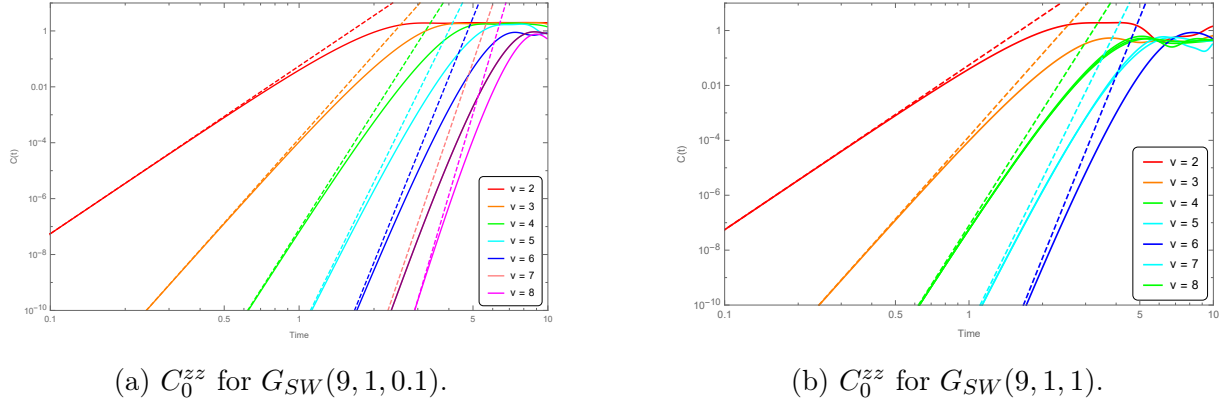


Figure 4.8: Log-log plots of the OTOCs for networks generated with (a)  $p = 0.1$  and (b)  $p = 1$ , showing power-law behaviour. The solid lines are the  $C_0^{zz}(v, t)$ , and the dashed lines are given by the power-law expression of (4.14), with  $l = d(1, v)$ .

We could make empirical approximations, based on statistical features of the simulated curves; however in the absence of physical, or analytical, arguments, this would be speculative. As examples, shown in Figure 4.11, where we plot the mean and standard deviations of the OTOCs alongside the original curves. We see that, after the initial growth period, the mean correlation,  $\langle C_0^{zz}(t) \rangle_v$ , fluctuates about a constant value of  $\sim 1$ . Furthermore, from the two samples shown in the figure, the time taken to reach this state is shorter for the random graph than for the regular graph.

### Small-world Heisenberg Model

Having studied in detail the transverse field Ising model on small-world networks, with  $\sigma_i^z \sigma_j^z$  spin interaction, let us now introduce the transverse spin interactions,  $\sigma_i^x \sigma_j^x$  and  $\sigma_i^y \sigma_j^y$  into the Hamiltonian. We may therefore write a general Hamiltonian, related to the *XYZ* Heisenberg model, without external interactions and over any network of spin interactions,

$$H_{XYZ} = \sum_{i=1}^N \sum_{j=1}^N \sum_{\mu \in \{x, y, z\}} J_{ij}^\mu \sigma_i^\mu \sigma_j^\mu. \quad (4.15)$$

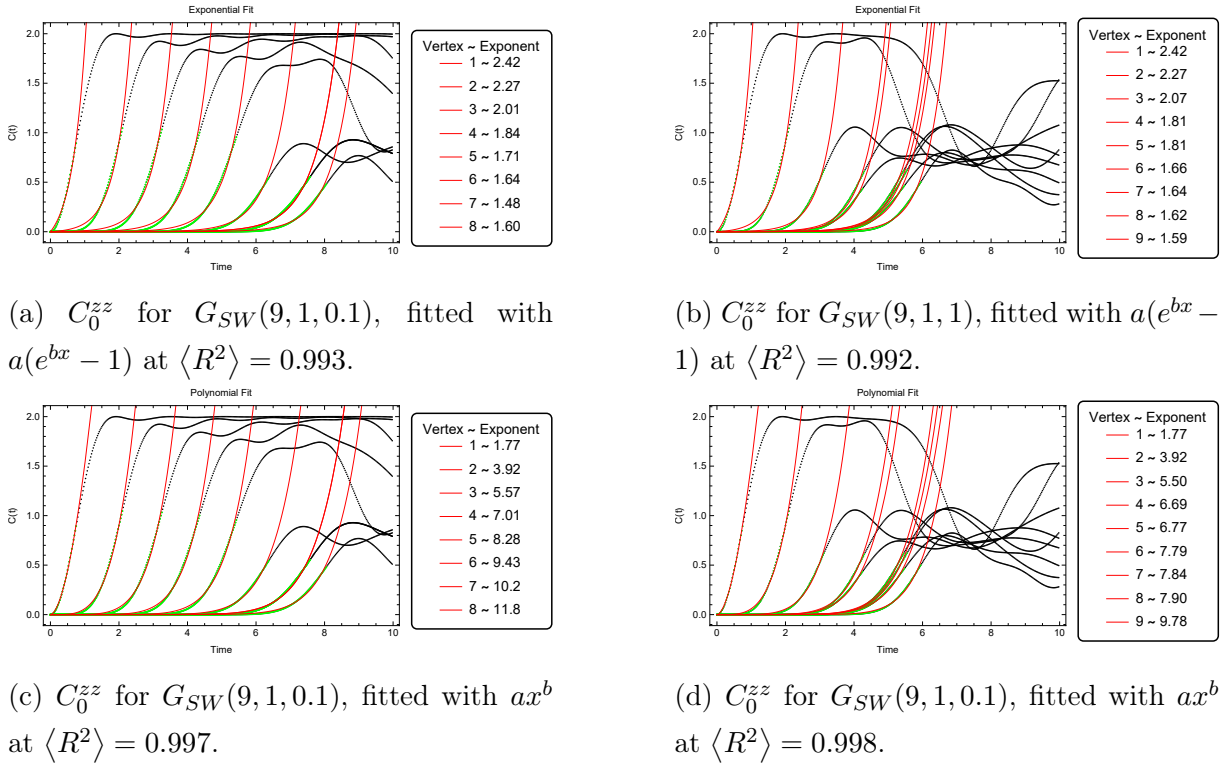


Figure 4.9: Plots indicating the (a, b) exponential and (c, d) power-law fitted models for (a, c)  $p = 0.1$  and (b, d)  $p = 1$ . The models were fitted to the convex regions of each curve (highlighted green), where  $t \leq t_v^*$ . The goodness-of-fit is given by the  $R^2$  statistic, averaged over each of the curves. The legends indicate the best-fit exponents ( $b$ ) for each fitted model, with the curves numbered sequentially in time.

The  $\mathbf{J}^\mu = J^\mu \mathbf{A}$  weighted adjacency matrices define the network topology and (an)isotropy; we shall consider the adjacency matrix to be fixed in the  $x, y, z$  directions, with only the weightings able to vary. Specifically,

$$\begin{aligned}
 J^x = J^y = J^z &\implies XXX, \\
 J^x = J^y \neq J^z &\implies XXZ, \\
 J^x \neq J^y \neq J^z &\implies XYZ.
 \end{aligned}$$

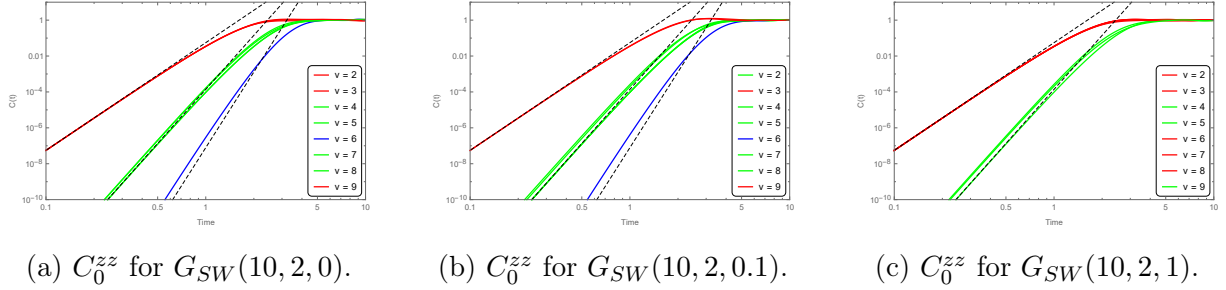


Figure 4.10: Log-log plots of the OTOCs for networks generated with (a)  $p = 0$ , (b)  $p = 0.1$  and (c)  $p = 1$ , showing power-law behaviour. The solid lines are the  $C_0^{zz}(v, t)$ , and the dashed lines are given by the power-law expression of (4.14), with  $l = d(1, v)$ . The colours of each curve indicate distance from the initial site.

Indeed, we begin by considering the following  $XXZ$  model,

$$H_{XXZ} = \sum_{i=1}^N \sum_{j=1}^N \frac{J_{ij}}{2} (\sigma_i^x \sigma_j^x + \sigma_i^y \sigma_j^y) + J_{ij}^z \sigma_i^z \sigma_j^z, \quad (4.16)$$

with the weighting terms  $J = 0.5$  and  $J^z = 0.6J$ . We consider these particular values to compare with the results of Dóra and Moessner (2), who studied the OTOCs of this model with nearest-neighbour interactions. Indeed, in this integrable case, they found that the OTOCs also obey early-time power-law growth given by the equation

$$C_0^{zz}(v, t) \sim \frac{t^{2l}}{(2l)!}. \quad (4.17)$$

This formula was obtained by Swingle and Roberts (87) using the Hausdorff-Campbell-Baker expansion of nested commutators of the time-evolved operator,

$$\sigma_i^\mu(t) = \frac{(it)^0}{0!} \sigma_i^\mu + \frac{(it)^1}{1!} [H, \sigma_i^\mu] + \frac{(it)^2}{2!} [H, [H, \sigma_i^\mu]] + \dots \quad (4.18)$$

Now, how do we expect the OTOC behaviour to change (from the one-dimensional Ising interaction), given the addition of the transverse interaction terms? An initial comparison of the plots in Figures 4.12, 4.13 ( $XXZ$ ) and 4.5, 4.4 (Ising), shows increasingly random fluctuations beyond the initial growth phase in the  $XXZ$  model, whereas those of the Ising model have a more regular, ‘periodic’, appearance. Heuristically, it could be argued

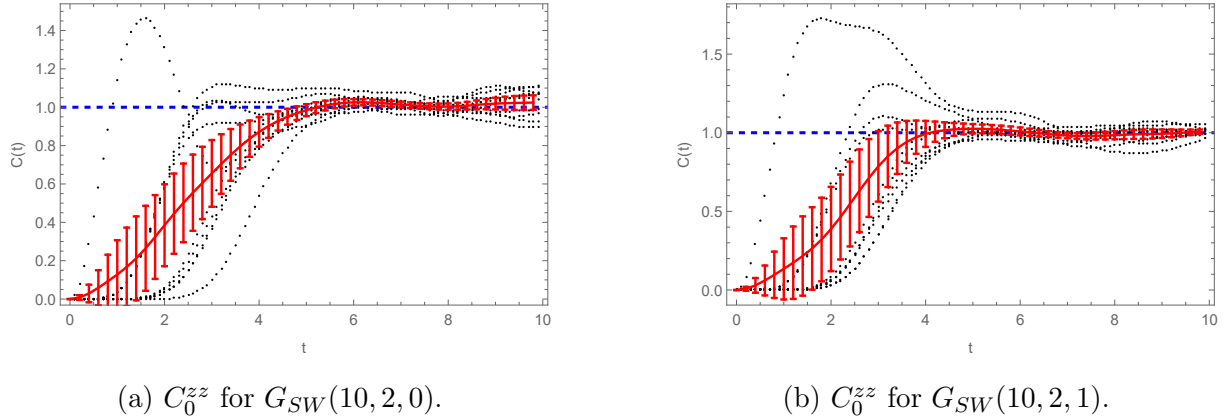


Figure 4.11: OTOCs for the regular, and random, next-to-nearest neighbour networks with  $N = 10$ . The red curve indicates the mean,  $\langle C_0^{zz}(t) \rangle_v$ , averaged over the  $N$  vertices, plotted with standard deviation on the error bars. The horizontal dashed line at 1 represents the value of the correlations at which the system is said to be scrambled.

that this is due to the new transverse terms allowing correlations to spread in the  $x$  and  $y$  directions as well. Therefore, when observing the correlations in the  $z$  operators,  $C_0^{zz}$ , we see the effects of this operator mixing.

We now compare Figures 4.12 and 4.13, for the computed OTOCs for networks of 10 vertices, with edge densities given by the parameter  $K = 1, 2$ , respectively. In the regular case, with  $p = 0$ , these correspond to nearest, and next-to-nearest, neighbour interactions, respectively. At this, relatively, small number of vertices, the most obvious difference between the two figures is the significant variation in path lengths for each graph, leading to different rates of propagation of the OTOCs. A further observation is the increased frequency of oscillation for the  $K = 2$  case, due to the increased edge density in the network. We could make an analogy with a system of coupled oscillators, where each edge represents an effective spring constant; therefore by adding in more springs, the effective spring constant increases and the system becomes ‘stiffer’ increasing oscillation frequency.

What about the early-time growth of the correlations? From (4.17), we should expect to see the OTOCs maintain power-law early-time growth rather than exponential. Looking

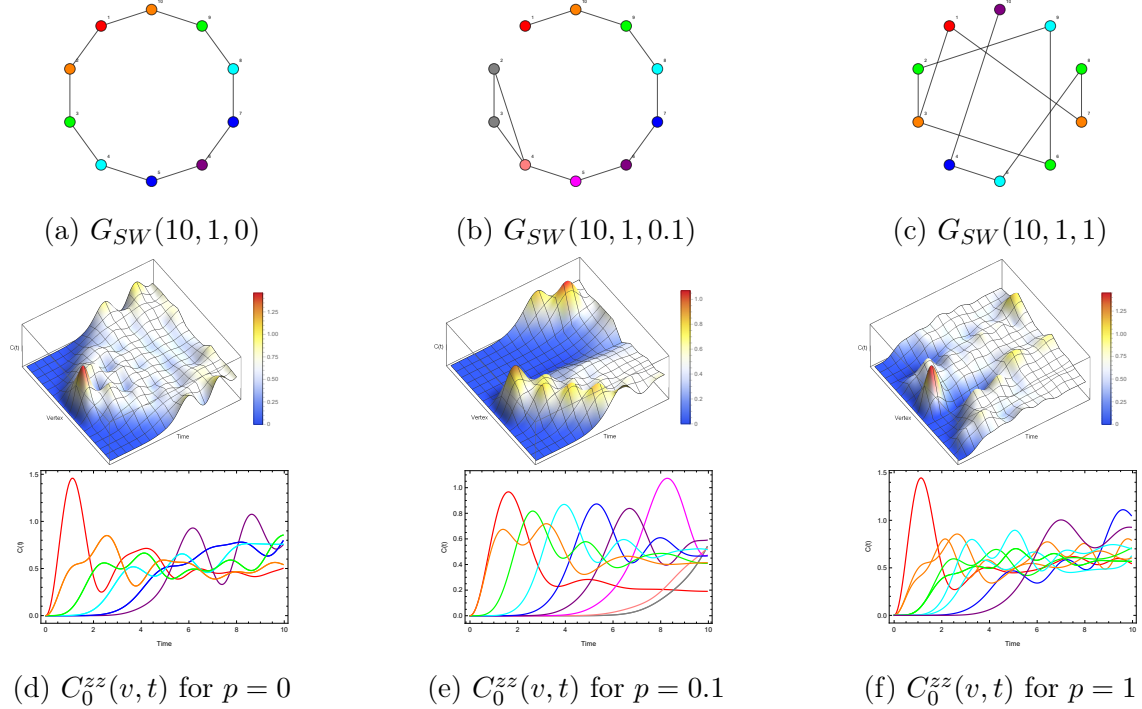


Figure 4.12: OTOCs for the Heisenberg XXZ model with  $N = 10$  and  $K = 1$  nearest-neighbour interactions, at  $p = 0, 0.1, 1$  in columns 1,2 and 3, respectively. The first row depicts the graph for which the OTOCs were computed. The second row shows a 3D plot of the initial perturbation propagating over the system. The third row shows the 2D plot of the OTOCs projected onto the same plane. The colouring of vertices (in the first row) and curves (in the third row), reflects the edge distance  $d(1, v)$ , to vertex 1 (red).

at Figure 4.14, we observe that this is indeed the case; the OTOCs exhibit linear growth on the log-log axes, at the same gradient (growth rate) predicted by the power-law formula. These results are very similar to those of the Ising model in Figures 4.8 and 4.10: we see good agreement with the power-law formula (predicted for the nearest neighbour system), even for the random graph case in column 3 (provided that we plot the curves according to distance from the initial vertex).

However, for the  $K = 2$  case in row 2 of the Figure, we did in fact observe a deviation between the predicted and computed curves. We obtained the agreement shown in plots

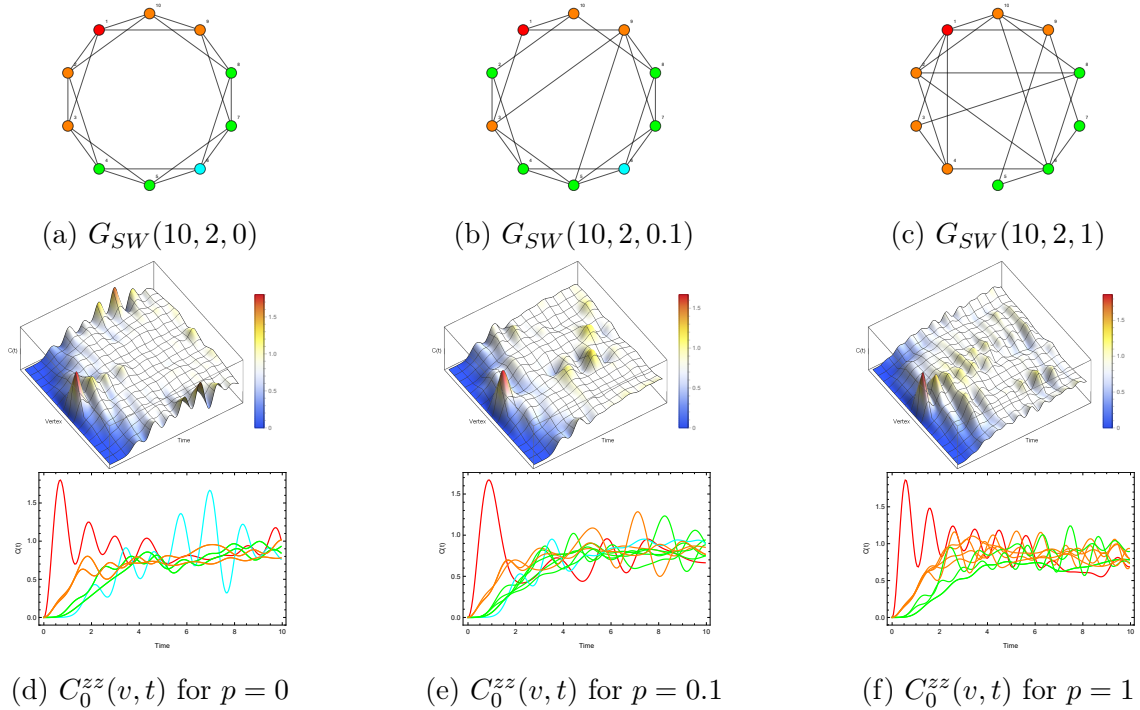


Figure 4.13: OTOCs for the Heisenberg XXZ model with  $N = 10$  and  $K = 2$  next-to-nearest-neighbour interactions, at  $p = 0, 0.1, 1$ . The first row depicts the graph for which the OTOCs were computed. The second row shows a 3D plot of the initial perturbation propagating over the system. The third row shows the 2D plot of the OTOCs projected onto the same plane. The colouring of vertices (in the first row) and curves (in the third row), reflects the edge distance  $d(1, v)$ , to vertex 1 (red).

(d,e,f), by instead considering the modification of the formula (4.17),

$$C_0^{zz}(v, t) \sim \frac{t^{2l}}{(2l - (K - 1))!}, \quad (4.19)$$

where we introduce the familiar interaction length  $K$ . This formula appears to apply too as  $K$  increases; of course for  $K = 1$  it remains unchanged for the nearest neighbour model, but for  $K = 2$  and  $K = 3$ , we can see the improvements in Figure 4.15. The red lines of the original formula deviate significantly from the actual computed curves, whereas the modified formula maintains good agreement as  $K$  is varied.

We note that this is merely an empirical observation, and may not represent the true

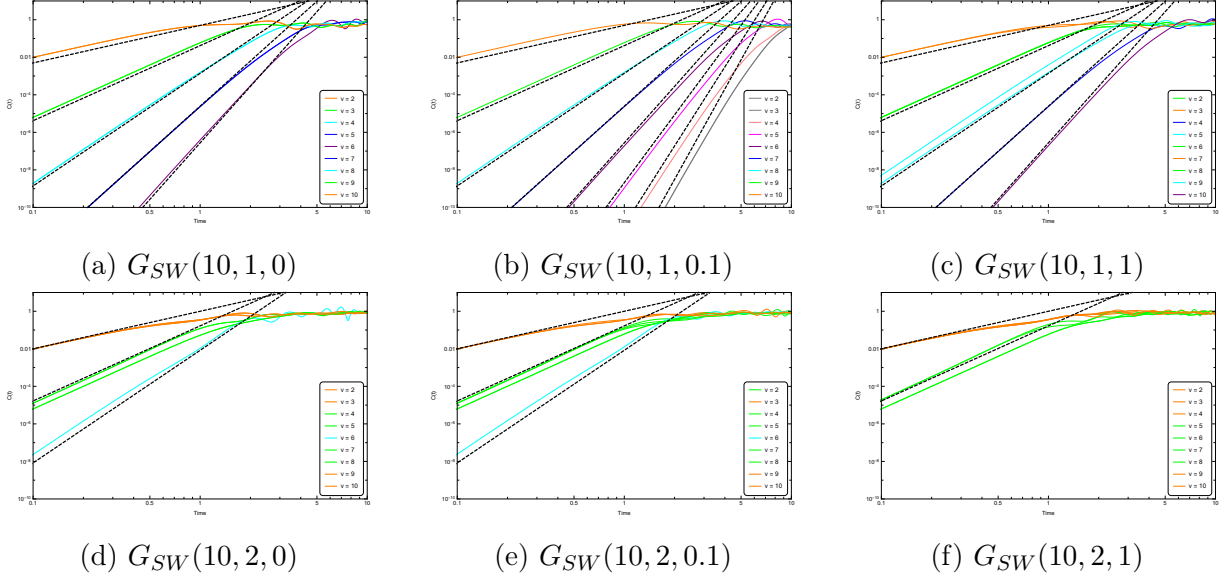


Figure 4.14: Log-log plots of the early-time behaviour of the  $C_0^{zz}(v, t)$  for the Heisenberg XXZ model, with  $N = 10$  vertices. Row 1 corresponds to the OTOCs, with  $K = 1$  nearest neighbour interaction, from Figure 4.12. Row 2 corresponds to the OTOCs, with  $K = 2$  next-to-nearest neighbour interaction, from Figure 4.13. The columns, from left to right, represent increasing rewiring probabilities,  $p = 0, 0.1, 1$ . In each plot, the solid curves are the computed OTOCs, highlighted by colour depending on edge distance from vertex 1. The dashed lines represent the power law curves.

behaviour of the system for arbitrary  $N$  and  $K$ . However, further investigation to derive a formula with explicit  $K$  dependence is warranted.

Finally, what changes do we observe in the scrambling behaviour of the  $XXZ$  model, compared to the Ising model? Looking at Figure 4.16, we actually observe less overall scrambling relative to the Ising model; as discussed in the previous section we are using the mean and standard deviation as a means of comparison, but note that it is speculative, and not an absolute measure. Specifically, the vertex-averaged correlator,  $\langle C_0^{zz}(t) \rangle_v$ , does not approach a stable value of  $\sim 1$  at the same rate as for the Ising model. We argue that this is also a consequence of the introduction of the transverse,  $x$  and  $y$ , degrees of freedom. Since the initial perturbation can now spread over these as well, we observe a lower value for the  $C_0^{zz}$  correlations in the  $z$  direction.

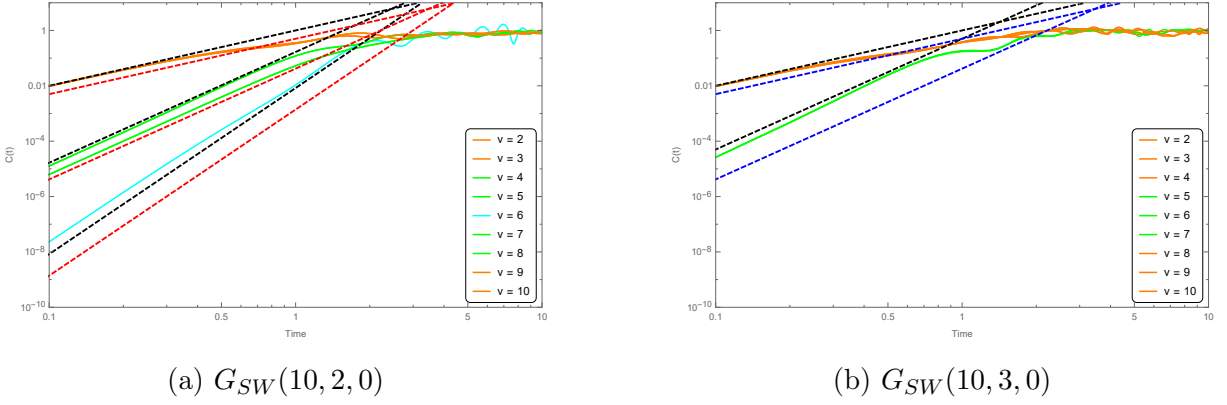


Figure 4.15: Log-log plots of the early-time behaviour of the  $C_0^{zz}(v, t)$  for the Heisenberg XXZ model, with  $N = 10$  vertices. In each plot, the solid curves are the computed OTOCs, highlighted by colour depending on edge distance from vertex 1. The red dashed lines represent the original power law curves predicted by (2). The black dashed lines represent the modified power law curves given by (4.19).

Additionally, we observe that the growth is slower for the  $K = 1$  case in the first row, without a significant difference as  $p$  is increased. 4.16b is an interesting case, in that the network configuration is analogous to a one-dimensional chain with a loop at the end (Figure 4.12b). Thus, we observe the wavefront propagating over a longer time; hence the localisation is maintained, and the scrambling effect is reduced. The scrambling rate for the  $K = 2$  networks in row 2 does appear to increase as the rewiring probability is increased;  $\langle C_0^{zz}(t) \rangle_v$  peaks nearer to 1, in Figure 4.16f, more rapidly than for the cases with zero or few rewirings.

### 4.3.2 Spectral Form Factors

Having studied the OTOCs for the small-world spin networks, where the integrability was broken by the introduction of long-range, random, rewirings, we observed a lack of exponential growth in the correlations. Yet, from our understanding of RMT eigenvalue statistics, we would expect to see some change in behaviour as our small world network transitions from integrable to non-integrable. Therefore, we now utilise the spectral form

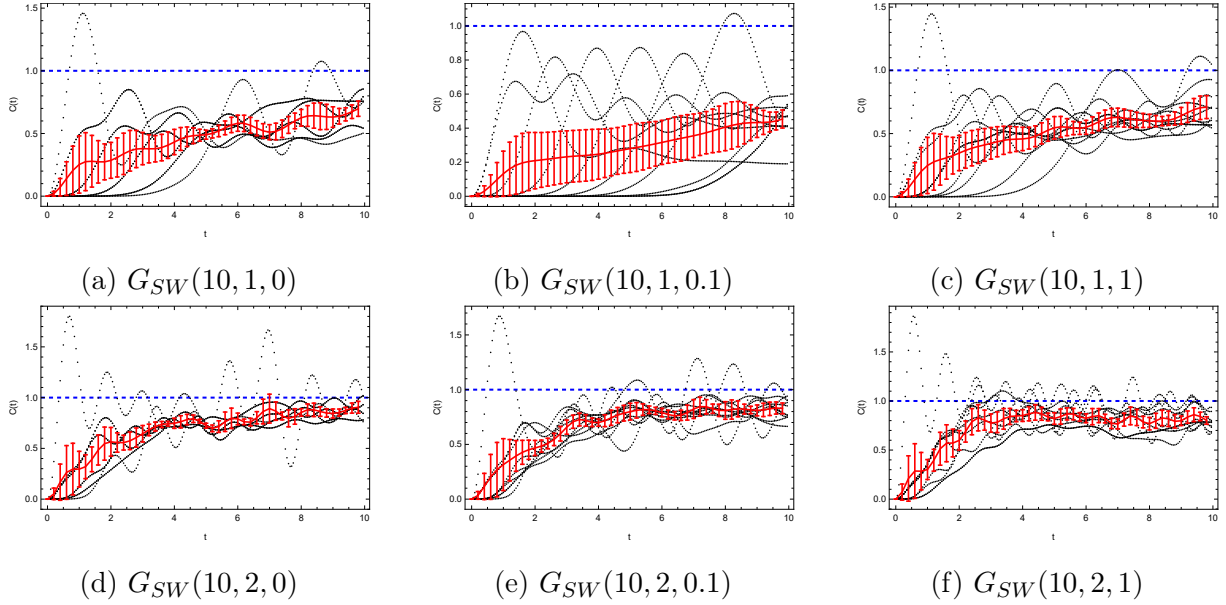


Figure 4.16: Replotted OTOCs for the 6 network configurations of Figures 4.12 and 4.13, showing the scrambling behaviour. The dotted black curves are the original curves  $C_0^{zz}(v, t)$ . The blue dashed lines represent the correlator values at which the scrambling is expected to maximise. The red curve is the mean correlation,  $\langle C_0^{zz}(t) \rangle_v$ , averaged over each vertex, with standard deviation on the error bars.

factor as a further diagnostic that may serve as a link between the early-time behaviour of the OTOCs and the late-time, statistical behaviour of the Hamiltonian eigenvalue spectrum.

As discussed in Section 3.3.2, our analysis of the spectral form factors, for varying network configurations, is primarily focused on two properties, (i) the dip-ramp-plateau structure, and (ii) the relationship between the ramp length,  $t_{plateau} - t_{dip}$ , and the system size,  $N$ .

Beginning with Figure 4.17, we compute the infinite temperature ( $\beta = 0$ ) SFF for a Heisenberg XXX network of  $N = 11$  vertices. From left to right, we can see that the transition to ramp-plateau structure is immediate following the introduction of random rewirings, becoming more pronounced with increasing randomness.

The smooth dip structure appears to be universal, which can be understood by considering

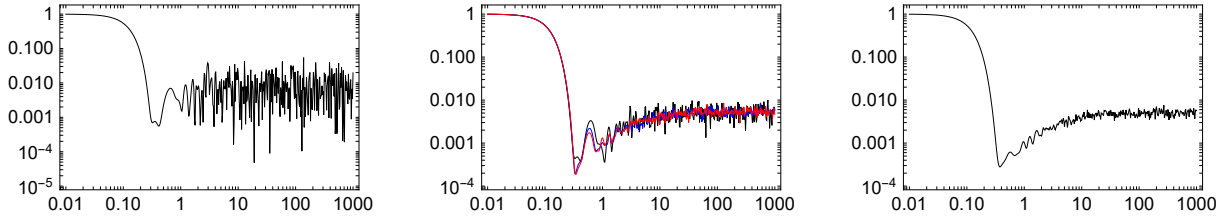


Figure 4.17: Spectral form factors  $g(t; 0)$ , at infinite temperature, for various rewiring probabilities of the Heisenberg XXX network of  $N = 11$  vertices. The plot on the left is for the regular chain with  $p = 0$ . The central plot is of the small-world network containing a small number of rewirings ( $1 \implies p \approx 0.09$  in black,  $2 \implies p \approx 0.18$ , in blue and  $3 \implies p \approx 0.27$  in red). The plot on the right is for  $p = 1$ , corresponding to a random graph. The disorder average is taken over  $J = 100$  realizations of each network.

the form of the SFF as expressed in (3.31); rewritten here:

$$g(t; 0) = \frac{1}{2^N} \left\langle 2^N + 2 \sum_{m=1}^{2^N-1} \sum_{n=m+1}^{2^N} \cos(E_m - E_n)t \right\rangle_J.$$

At  $t = 0$ , the summation term is zero, giving  $g(t; 0) = 1$ . For sufficiently small times, the cosine term is dominated by  $t \ll 1$ , making  $g(t; 0)$  essentially independent of the differences in energy levels, since at small times  $\cos t \approx 1$ ; this is illustrated by the example of a log-log plot of  $\cos t$  in Figure 4.18.

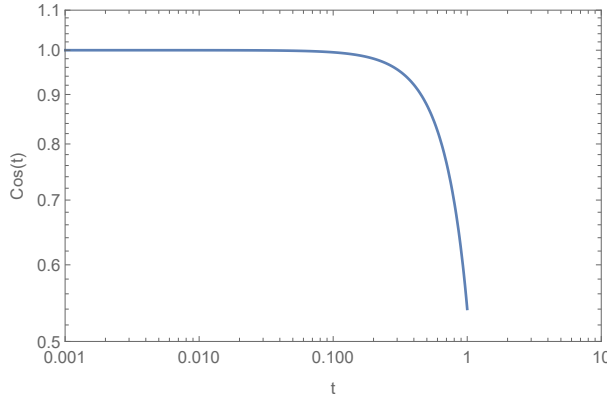


Figure 4.18: Log-log plot of the function  $\cos t$  for small values of  $t$ .

Subsequently, as  $t$  increases the first  $(E_m - E_n)$  terms to challenge the dominance of small

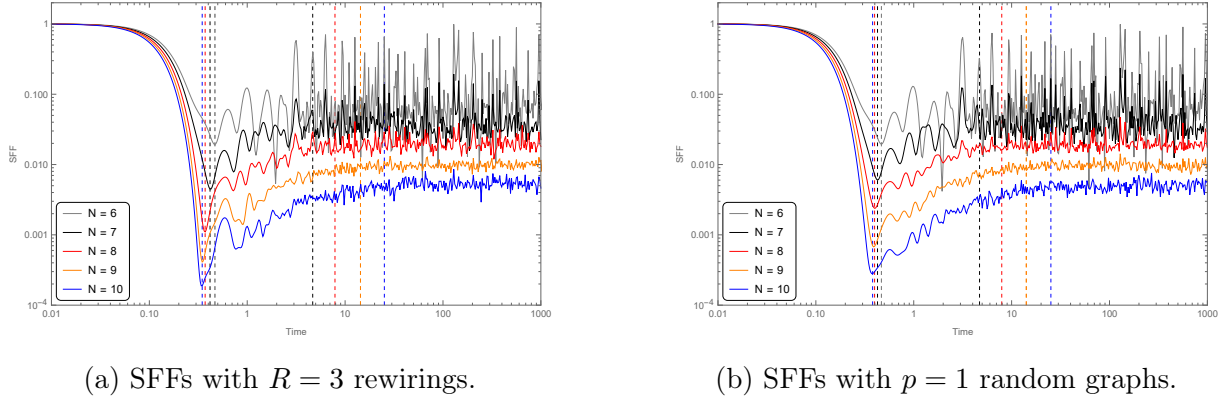


Figure 4.19: Plot of the spectral form factors for varying system sizes, with a fixed number of edges,  $K = 2$ , and (a) 3 rewirings and (b) completely random graphs.

$t$  will be those with the largest energy separations. By extrapolation, we may note that the time parameter,  $t$ , determines the scale of energy differences being probed (1), with the energy separations decreasing as  $t$  increases. Indeed, this behaviour is the origin of the plateau structure, since at large enough times only the (zero energy separation) terms with  $E_m = E_n$  survive. Moreover, the time at which this occurs is referred to as the plateau time,  $t_p$ , and is defined as the disorder-averaged inverse mean level spacing,

$$t_p = \left\langle \frac{2^N - 1}{\sum_{i=1}^{2^N-1} |E_{i+1} - E_i|} \right\rangle_J. \quad (4.20)$$

The inverse mean level spacing is the same quantity used to perform spectral unfolding in order to study the eigenvalue spacing distribution (as discussed in Section 3.2). Now that we are able to determine the time of onset of the plateau,  $t_p$ , we just need the dip time  $t_d$  in order to calculate the length of the ramp. This is easy to achieve computationally, since it corresponds to the first stationary point of the curve after the dip.

We now plot the spectral form factors in Figure 4.19, for small-worlds (4.19a) and random graphs (4.19b) at varying  $N$ . The vertical dashed lines indicate the times  $t_d$  and  $t_p$ , in the same colour as the associated SFF curve. From these plots, we notice a number of features. Firstly, there does not appear to be a significant difference between the curves for the small world and random graphs; the biggest change in behaviour is a lowering of the small ‘peak’ following the dip time for the random graphs.

Secondly, the magnitude of the fluctuations appears to decrease as the system size increases. This could be due to an increased number of graphs over which the disorder average can be taken, since the purpose of the averaging procedure is to smooth them out. More precisely, for smaller graphs, there are only a limited number of unique configurations, and so there is the possibility of repeated replicas being taken in the averaging, which do not have an effect. However, the number of configurations grows exponentially with graph size and order, hence the rapid smoothing as  $N$  grows.

Thirdly, the plateau time appears to grow linearly with system size; the spacing between consecutive vertical lines looks very much constant. Finally, the dip time actually decreases with increasing  $N$ . This is a surprising observation, since for chaotic models such as SYK, or even Gaussian random matrix ensembles, the rapid growth of the dip time is a significant factor, even leading Cotler *et al* (1) to make the conjecture that it is a new timescale in the theory. A final comparison is therefore to note that we see a linear growth in the length of the ramp, whereas they observed it to be exponential for the SYK model.

### 4.3.3 Eigenvalue Statistics

In this section, we provide a brief overview of our preliminary analysis of eigenvalue statistics. We note that this research is still ongoing.

Now, this system is completely integrable and the spectrum is exactly solvable, in the large- $N$  limit, using the Bethe Ansatz (88). We can also use intuition from classical physics to understand the eigenvalue spectrum in this case; such a system of  $N$  spins, either up or down, should have  $2^N$  eigenvalues in  $N + 1$  distinct energy levels. Furthermore, degeneracies due to rotational symmetry should result in  $\binom{N}{i}$  repeated eigenvalues at energy level  $0 \leq i \leq N$ . As an example, consider a network with  $N = 5$ , and normalised spectrum, as shown in Figure 4.20. For 5 particles, there are 6 possible configurations of up-, and down-, spinors, as enumerated in Table 4.2.

However, in Figure 4.20b, we see only three distinct energy levels; isotropy in the  $z$ -direction means that there is no energetic difference between spin-up and spin-down, so

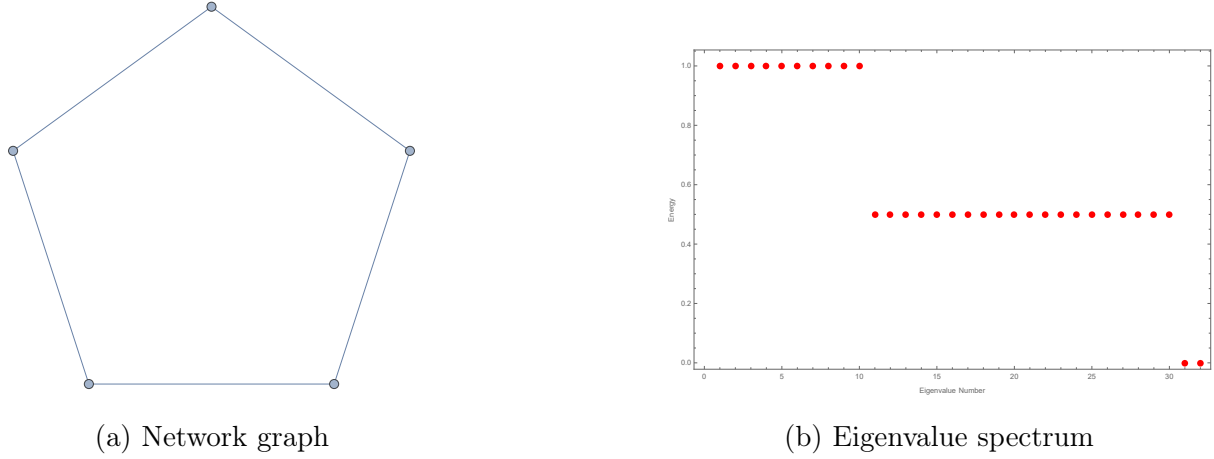


Figure 4.20: Network graph and normalised eigenvalue spectrum for a periodic Ising chain of 5 particles and nearest-neighbour interactions. Note that we normalise the spectrum in the range 0 to 1, since we are more interested in their relative values, for the spacing distribution.

the 3 levels correspond to (i) all spins aligned (2 states at  $E = 0$  and  $S_z = \pm \frac{5}{2}$ ), (ii) 1 spinor anti-aligned (20 states at  $E = 0.5$  and  $S_z = \pm \frac{1}{2}$ ), and (iii) 2 spinors anti-aligned (10 states at  $E = 1$  and  $S_z = \pm \frac{3}{2}$ ).

In this case, it is clear that the spacing distribution is Poisson-like (as expected for an integrable system), since there are only 2 nonzero values ( $\Delta E = 0.5$ ), representing the transitions between the 3 energy levels.

In order to distinguish each of the 6 spin parity sectors, we must break these symmetries by introducing the external field interaction of (4.7), resulting in Figure 4.21a. This is in agreement with the possible configurations listed in Table 4.2. Note the small gap in the 10 eigenvalues corresponding to spins  $\pm \frac{1}{2}$ . These energy levels both contain 2 spinors anti-aligned with the other 3; the gap is due to energetic disparities between configurations where the 2 spinors are adjacent, or separated by one of the other anti-aligned spinors.

$S_z$	States	Configurations
$\frac{5}{2}$	1	$\downarrow\downarrow\downarrow\downarrow\downarrow$
$\frac{3}{2}$	5	$\uparrow\downarrow\downarrow\downarrow\downarrow$ $\downarrow\uparrow\downarrow\downarrow\downarrow$ $\downarrow\downarrow\uparrow\downarrow\downarrow$ $\downarrow\downarrow\downarrow\uparrow\downarrow$ $\downarrow\downarrow\downarrow\downarrow\uparrow$
$\frac{1}{2}$	10	$\uparrow\uparrow\downarrow\downarrow\downarrow$ $\downarrow\uparrow\uparrow\downarrow\downarrow$ $\downarrow\downarrow\uparrow\uparrow\downarrow$ $\downarrow\downarrow\downarrow\uparrow\uparrow$ $\uparrow\downarrow\downarrow\downarrow\uparrow$ $\uparrow\downarrow\uparrow\downarrow\downarrow$ $\downarrow\uparrow\downarrow\uparrow\downarrow$ $\downarrow\downarrow\uparrow\downarrow\uparrow$ $\uparrow\downarrow\downarrow\uparrow\downarrow$ $\downarrow\uparrow\downarrow\downarrow\uparrow$
		$\uparrow\uparrow\uparrow\downarrow\downarrow$ $\downarrow\uparrow\uparrow\uparrow\downarrow$ $\downarrow\downarrow\uparrow\uparrow\downarrow$ $\uparrow\downarrow\downarrow\uparrow\uparrow$ $\uparrow\uparrow\downarrow\downarrow\uparrow$ $\uparrow\downarrow\uparrow\uparrow\downarrow$ $\downarrow\uparrow\downarrow\uparrow\uparrow$ $\uparrow\downarrow\uparrow\downarrow\uparrow$ $\uparrow\uparrow\downarrow\uparrow\downarrow$ $\downarrow\uparrow\uparrow\downarrow\uparrow$
$-\frac{1}{2}$	10	$\uparrow\uparrow\uparrow\uparrow\downarrow$ $\downarrow\uparrow\uparrow\uparrow\downarrow$ $\downarrow\downarrow\uparrow\uparrow\downarrow$ $\uparrow\downarrow\downarrow\uparrow\uparrow$ $\uparrow\uparrow\downarrow\downarrow\uparrow$ $\uparrow\downarrow\uparrow\uparrow\downarrow$ $\downarrow\uparrow\downarrow\uparrow\uparrow$ $\uparrow\downarrow\uparrow\downarrow\uparrow$ $\uparrow\uparrow\downarrow\uparrow\downarrow$ $\downarrow\uparrow\uparrow\downarrow\uparrow$
$-\frac{3}{2}$	5	$\uparrow\uparrow\uparrow\uparrow\downarrow$ $\downarrow\uparrow\uparrow\uparrow\uparrow$ $\uparrow\downarrow\uparrow\uparrow\uparrow$ $\uparrow\uparrow\downarrow\uparrow\uparrow$ $\uparrow\uparrow\uparrow\downarrow\uparrow$
$-\frac{5}{2}$	1	$\uparrow\uparrow\uparrow\uparrow\uparrow$

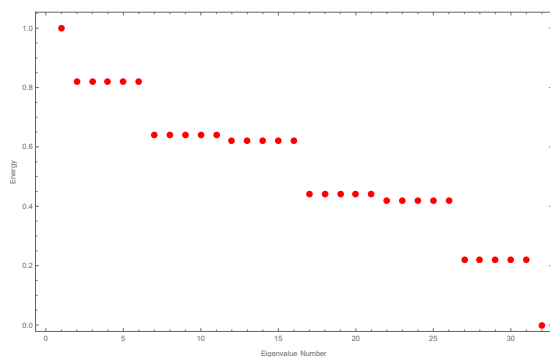
Table 4.2: Spin state configurations for 5 spin- $\frac{1}{2}$  particles in a periodic Ising chain.

## 4.4 Summary

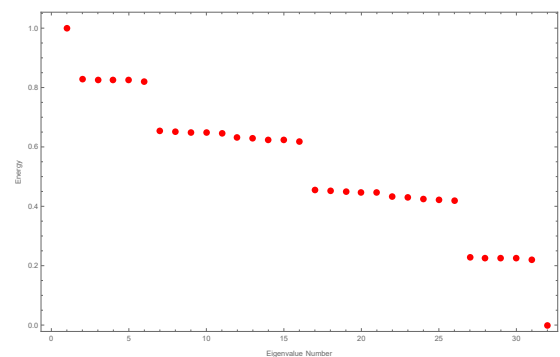
In this chapter, we have presented the results of our numerical simulations of quantum small-world spin networks. This is a novel class of spin model that we have introduced through the application of the Watts-Strogatz algorithm to the familiar spin-exchange Hamiltonian in a network of spinors.

We began by discussing the methodology approached in simulating such a system, including the computational specifications, programming language and packages used in performing the exact diagonalization of the system Hamiltonian.

In analysing our quantum small-worlds, we first utilised the regular (integrable) Ising model as a benchmarking tool for ensuring that our numerical procedure is correct and able to reproduce known results in the literature. Specifically, we compared our results with those of Lin and Motrunich for the calculation of the OTOCs for the same model, and found good agreement. Thereafter we applied the Watts-Strogatz algorithm to generate small-worlds containing random, long-range, interactions, and studied the effects of these on the system OTOCs. We found that the OTOCs continue to exhibit polynomial-time growth, even in the presence of long-range disorder. Thus, even for non-integrable systems, there is no exponential growth indicative of chaotic behaviour at early times.



(a) Spectrum with a moderate external field,  $h = 20$  and unit coupling strengths.



(b) Spectrum with  $h = 20$  external field and edge weights sampled from a uniform distribution with unit mean and  $\sigma = 0.9$  standard deviation.

Figure 4.21: Eigenvalue spectra for the chain of 5 particles, illustrating the effects of an external field and edge weightings on the system energy levels.

# Chapter 5

---

## Conclusion

---

### 5.1 Thesis Summary

We began this thesis with the aim of studying the scrambling of quantum information in interacting many-body quantum systems. In particular, we have been interested in understanding the relationship between scrambling and properties such as chaos, disorder and randomness. However, the way in which these properties interact, to affect the scrambling behaviour of a given system, has remained obscured. Indeed, identifying the precise nature of these interactions is a significant problem with wide-ranging implications, from the physics of black hole thermalisation to localisation and coherence in quantum computing.

With this goal in mind, we set out to study a system in which the amount of disorder could be controlled, parametrically, thereby allowing us to observe a transition between integrability and non-integrability. To this end, we introduced the concept of a quantum small world - the quantum analog of the Watts-Strogatz model of network theory. In this model, disorder is introduced through the generation of interactions between randomly selected particles, which is controlled by the rewiring probability parameter of the Watts-

Strogatz algorithm. The bulk of the research covered in this thesis was concerned with developing the theoretical and computational tools necessary to construct, simulate, and analyse this class of model; the details of which have been submitted for publication (44), and are summarised as follows.

In Chapter 2, we discussed the theory of classical small world networks. This began with a review of key concepts and definitions from algebraic graph theory. Most notable for our work were the adjacency matrix representation of, and notions of distance, path length and clustering in, graphs. These concepts were then used to introduce the small world network model of Watts and Strogatz, constructed by way of their namesake algorithm. By studying the small-worldness parameters for varying network configurations, we found that the characteristic features of high clustering and low path length were maximised in large ( $N > 200$ ) sparse networks with low ( $\rho < 0.1$ ) edge density and low rewiring probability ( $p \sim 0.1$ ).

In Chapter 3, we introduced measures for diagnosing chaos in quantum systems. A review of the origins of quantum chaos led us to the basics of random matrix theory; here we focused on the Gaussian random matrix ensembles, the most significant results being the Berry-Tabor and Bohigas-Giannoni-Schmidt conjectures. These relate the spectral statistics of integrable and chaotic quantum systems to Poisson and Wigner surmise distributions, respectively. Next, we discussed two time-dependent signatures of chaos that have been studied extensively in recent years, the out-of-time-order correlator and spectral form factor. Whereas the RMT statistics were originally used to study the late-time, statistical, features of quantum analogues of classically chaotic systems, the OTOC and SFF have been utilised to probe chaotic behaviour, at early and intermediate timescales, in strongly-correlated many-body quantum systems that do not have a classical counterpart.

Chapter 4 forms the central results of this thesis, wherein we applied the techniques developed in the earlier chapters to study the dynamical properties of quantum small world networks. We began by detailing our methodology for performing this analysis by numerical simulation. Due to computational limitations on the size of system that could be simulated, we found that the rewiring probability was not a good parameter for controlling the amount of disorder introduced into the system. Therefore, we proposed a

modification to the Watts-Strogatz algorithm, based instead on specifying the number of random rewirings to be performed, which is more appropriate for systems of  $N \sim \mathcal{O}(10)$  particles.

We used this modified algorithm to generate a small world network, and then used the graph adjacency matrix to construct a generic interaction Hamiltonian of spin-half particles located at each vertex. Numerical time evolution of the spin operators was performed, in the Heisenberg representation, by exact diagonalisation of the Hamiltonian.

We then studied in detail the OTOCs for varying network configurations. We began by testing our results against those of known models in the literature, specifically for the transverse field Ising, and  $XXZ$  Heisenberg, chains, both easily recovered from our generic interaction Hamiltonian. Agreement with these results confirmed that our numerical procedures were precise.

This led naturally to the original work presented in this thesis, wherein we extended our analysis by considering the same models, and then introducing disorder through increasing numbers of rewired edges, and next-to-nearest neighbour interactions. Both of these resulted in the systems becoming non-integrable. We extracted two primary features from the OTOCs, (i) the growth rate at early times and (ii) the average value at late times.

We found that, for both the Ising and Heisenberg models, regardless of the number of rewirings introduced, the OTOCs obeyed the power-law curves predicted for the regular, nearest-neighbour only chains, up to small deviations at larger time scales. Indeed, we observed that the time at which the OTOCs of each vertex began to grow depended only on the distance from the vertex to the site of the initial perturbation, but that the growth rate still matched the power law predictions.

We did not see any evidence of a transition from polynomial to exponential growth, and, therefore, no sign of early-time chaos in the form of a Lyapunov exponent. The same results were obtained for the next-to-nearest neighbour,  $K = 2$ , chains, with and without random rewirings. The only observed difference was for the  $XXZ$  model, where the exact form of power-law behaviour appeared to deviate for varying  $K$  value. We proposed a

new scaling law with explicit  $K$  dependence, and found improvement in the fit to the simulated OTOCs.

Regarding the late-time behaviour of the OTOCs, the growth of the time-evolved operators at each site is related to the scrambling of the information (of the initial perturbation) over the system degrees of freedom under unitary time evolution. We observed that the systems with random rewirings, and higher edge densities, scrambled faster than the regular, integrable, models. In other words, there appeared to be a correlation between the average path length of the graph and the scrambling time. However, given the small system sizes that were studied, it was difficult to discern a clear relationship between small and large numbers of rewirings and the scrambling time; the results we obtained were not conclusive, though, intuitively, we would expect to observe such a correlation.

Finally, we turned to the spectral form factor as a final diagnostic to understand these systems that were known to be non-integrable, yet did not exhibit exponential growth in their OTOCs. We computed the SFFs for the same spin networks as the OTOCs, varying the interaction length,  $K$ , and the number of rewired edges, from 0 (regular graph) to  $NK$  (random graph). Again, we investigated two primary features from the SFFs, (i) the dip-ramp-plateau behaviour expected for non-integrable systems, and (ii) the  $N$  dependence of the ramp length (equivalently, plateau time) expected for chaotic systems.

We found that the regular (integrable) networks, with no rewirings, did not exhibit a clear ramp-plateau behaviour. However, as we increased the number of random rewirings, the dip and ramp become more pronounced, with a more stable plateau. This is indicative of the level repulsion in the eigenvalues at small energy separations, consistent with the Wigner surmise predictions of RMT. Despite this result, we did not observe a clear growth in the length of the ramp as  $N$  was increased.

In conclusion, from our study of the OTOCs and SFFs of quantum small world spin networks, we have thus far not observed any behaviour that would be classified as chaotic, despite the disorder associated with the introduction of random spin interactions in otherwise integrable systems. Therefore, what we have found is a class of random, disordered, models, without evidence of quantum chaos. Nevertheless we found that the introduction of disorder, even at very low levels, with  $\mathcal{O}(1)$  random rewirings, was sufficient to affect

---

the ability of the system to scramble information.

## 5.2 Outlook

This thesis has presented a novel class of spin network that is able to transition between ordered and disordered behaviour, along with preliminary analyses based on existing diagnostic tools. Furthermore, this is currently a exciting and relevant area of research, with much future potential; clearly there is a significant amount of further work to be done, with many possible avenues to explore. While the bulk of this work has been summarised in (44), since this submission we have been preparing a follow-up paper, in which we will provide a more detailed analysis of the quantum small world model. Broadly speaking, the bulk of the immediate research lies in improving our (i) computational, and (ii) analytical tools.

Regarding our numerical techniques for simulating a many-body quantum system, the primary bottleneck is of course the exponential growth in the system Hilbert space. This fact renders exact computations for the system sizes required to obtain a true small world network,  $N \sim \mathcal{O}(100)$ , intractable, even with access to state-of-the-art supercomputers. However, there are a number of steps we could take to improve our numerics.

First, access to a high performance computing unit able to exploit parallel computations, such as the University of Cape Town High Performance Computing Unit (UCT HPC), or the national Center for High Performance Computing (CHPC).

Second, while Mathematica's exact diagonalisation algorithms are based on the standard, efficient, LAPACK, procedures available in most scientific computing languages, its dynamic programming paradigm renders lengthy iterative computations, such as OTOC and SFF time evolution, highly inefficient. Therefore, we are in the process of converting our code, such that we use Mathematica to construct and diagonalise the Hamiltonian matrices, but then export and perform the time evolution using a more efficient, lower-level language, such as C, FORTRAN, or even Julia, on a high performance cluster. A further improvement comes in the form of approximation methods. Recently implemented by

our collaborator Dario Rosa, the Lanczos algorithm has been used for near-exact diagonalisation, which has already enabled access to system sizes up to  $N = 26$ , for certain calculations where the exact spectrum is not as necessary.

In terms of the analytical tools, the first expectation would be to obtain more definitive results for the OTOCs and SFFs based on the access to increased system sizes. In particular, it will be interesting to more clearly observe the relationship to the average path length and clustering coefficients in larger networks. Furthermore, with regards to the SFF, additional calculations need to be done in separating the connected and disconnected portions, and also considering finite temperature. Additionally, a new derivation of the power-law scaling of the OTOCs for the Hamiltonians with  $K > 1$  from the Hausdorff-Campbell-Baker formula is necessary; it is hoped that this will result in a new scaling law with explicit  $K$  dependence, that matches with our empirically observed results.

Second, despite our review discussion of the spectral properties of the small-world Hamiltonians, we noted that this is still a work in progress. The difficulties here lay in the eigenvalue degeneracies and mixing of energy levels; this has most recently been resolved through (i) the introduction of an external magnetic field term in the Hamiltonian to separate these levels, and (ii) random weighting of the adjacency matrices to break the degeneracies. However, a complete analysis based on the r-statistic is currently being completed.

Finally, the introduction of the randomly weighted adjacency matrices opens up another means of introducing disorder into the system. This is relevant since the well-known SYK has Gaussian distributed random couplings (and a  $q$ -point order spin interaction). The question here being how this might affect the scrambling or presence of chaos within the system. Perhaps it is instead the nature of the two-particle spin exchange interaction itself that is inherently non-chaotic, and it might be worth investigating higher-point interactions on hypergraphs. Indeed, this is speculative, but it is to emphasise that we have only just begun to scratch the surface on what appears to be a deep and fascinating field of study.

---

## Appendices

---

### A Mathematica Code Package

```
1 (* ::Package:: *)
2
3 (* ::Section:: *)
4 (*Functions *)
5
6
7 pauliTensor[x_, i_, n_] := pauliTensor[x, i, n] = N[KroneckerProduct @@ Table[If[m !=
8   ↪ i, SparseArray[N[PauliMatrix[0]]], SparseArray[N[PauliMatrix[x]]]], {m, n}]]
9
10
11 adjacencyMatrix[n_, p_, k_] := Module[{},
12   graph = RandomGraph[WattsStrogatzGraphDistribution[n, p, k]];
13
14   While[! ConnectedGraphQ[graph], graph = RandomGraph[WattsStrogatzGraphDistribution
15   ↪ [n, p, k]]];
16
17   Normal[AdjacencyMatrix[graph]]
18 ]
19
```

```
20
21 AdjacencyMatrixFixedRewirings[n_, rewirings_, k_] := Module[{  

22
23   g = RandomGraph[WattsStrogatzGraphDistribution[n, 0, k]],  

24
25   gComplete = CompleteGraph[n]  

26
27 },  

28
29 For[j = 1, j <= rewirings, j++,  

30 {  

31
32   e = RandomChoice[EdgeList[GraphDifference[CompleteGraph[n], g]]],  

33
34   gT = EdgeAdd[g, e],  

35
36   index = Flatten[Position[EdgeList[gT], e]][[1]],  

37
38   newEdgeVertices = {EdgeList[gT][[index, 1]], EdgeList[gT][[index, 2]]},  

39
40   neighbourList = Union[EdgeList[NeighborhoodGraph[g, newEdgeVertices[[1]]]],  

41   EdgeList[NeighborhoodGraph[g, newEdgeVertices[[2]]]]],  

42
43   edgeLengthList = Table[{i, GraphDistance[gT, neighbourList[[i]][[1]]],  

44   neighbourList[[i]][[2]]}, {i, Length[neighbourList]}],  

45
46   shortestEdgesList = Cases[edgeLengthList, i_ /; i[[2]] == Min[edgeLengthList  

47   [[;; , 2]]]],  

48
49   gTemp2 = gT,  

50
51   While[! ConnectedGraphQ[gTemp2 = EdgeDelete[gT, neighbourList[[RandomChoice[  

52   shortestEdgesList[[;; , 1]]]]]], gTemp2 = EdgeDelete[gT, neighbourList[[  

52   RandomChoice[shortestEdgesList[[;; , 1]]]]]]],  

52   g = gTemp2  

51 }]
```

```
53 ];
54
55 Normal[AdjacencyMatrix[g]]
56
57 ]
58
59
60 AdjacencyMatrixPlusRandomEdges[n_, edgesToAdd_, k_] := Module[{
61
62     g = RandomGraph[WattsStrogatzGraphDistribution[n, 0, k]],
63
64     completeGraph = CompleteGraph[n]
65
66 },
67
68 For[j = 1, j <= edgesToAdd, j++,
69 {
70
71     e = RandomChoice[EdgeList[GraphDifference[completeGraph, g]]],
72
73     g = EdgeAdd[g, e]
74
75 }
76 ];
77
78 Normal[AdjacencyMatrix[g]]
79
80 ]
81
82
83 SpinHalfHamiltonian[n_, k_, p_, {{\Mu}x_, {\Sigma}x_}, {{\Mu}y_, {\Sigma}y_}, {{\Mu}z_, {\Sigma}z_}],
84     fieldStrength_, OptionsPattern[{Model -> ToString[XXX], Field
85     -> -> ToString[Z]}]] := Module[
86
87     {
88         coupling
```

```
89
90 {
91
92     adjacency = AdjacencyMatrixFixedRewirings[n, p, k],
93
94     coupling = couplingTensor[n, adjacency, {{\[Mu]x, \[Sigma]x}, {\\[Mu]y, \[Sigma]y
95     \[Mu]z, \[Sigma]z}}, Model -> OptionValue[Model]],
96
97     Sum[(1) * coupling[[1, i, j]] * pauliTensor[1, i, n] . pauliTensor[1, j, n], {i,
98     \[i], {j, i + 1, n}, {1, 3}],
99
100    (*Sum[(-1) * coupling[[1, i, j]] * pauliTensor[1, i, n] . pauliTensor[1, j, n],
101    \[i], {j, i + 1, n}, {1, 3}]*)
102
103
104
105
106 SpinHalfHamiltonian2[n_, k_, p_, adjacency_, {{\[Mu]x_, \[Sigma]x_}, {\\[Mu]y_, \[Sigma]
107     \[Mu]z_, \[Sigma]z_}}, fieldStrength_, OptionsPattern[{Model -> ToString[
108     \[Model], Field -> ToString[Z]}]]] := Module[
109
110     {
111
112         coupling
113
114         },
115
116         adjacency,
117
118         coupling = couplingTensor[n, adjacency, {{\[Mu]x, \[Sigma]x}, {\\[Mu]y, \[Sigma]y
119     \[Mu]z, \[Sigma]z}}, Model -> OptionValue[Model]],
```

```

119   Sum[(1) * coupling[[l, i, j]] * pauliTensor[l, i, n] . pauliTensor[l, j, n], {i,
120   ↪ n}, {j, i + 1, n}, {l, 3}],
121
122   (*Sum[(-1) * coupling[[l, i, j]] * pauliTensor[l, i, n] . pauliTensor[l, j, n],
123   ↪ {i, n}, {j, i + 1, n}, {l, 3}]*)
124
125   deformationMatrix[n, fieldStrength, Model -> OptionValue[Model], Field ->
126   ↪ OptionValue[Field]]
127
128
129 deformationMatrix[n_, fieldStrength_, OptionsPattern[{Model -> ToString[XXX], Field ->
130   ↪ ToString[X]}]] := Module[
131
132   deformationSize = fieldStrength * OptionValue[Model] /. {"XXX" -> 1, "XXZ" -> 1,
133   ↪ "XYZ" -> If[OddQ[n], I, 1], "IsingX" -> 1, "IsingY" -> 1, "IsingZ" -> 1},
134
135   deformationDirection = OptionValue[Field] /. {"I" -> 0, "X" -> 1, "Y" -> 2, "Z"
136   ↪ -> 3},
137
138   deformationSum,
139
140   deformationMatrix
141
142   deformationSum = Sum[pauliTensor[deformationDirection, j, n], {j, n}];
143
144   deformationMatrix = OptionValue[Model] /. {"XXX" -> deformationSum, "XXZ" ->
145   ↪ deformationSum, "IsingX" -> deformationSum, "IsingY" -> deformationSum, "IsingZ"
146   ↪ -> deformationSum, "XYZ" -> DiagonalMatrix[Table[Chop[Exp[I * (Pi / 2) *
147   ↪ deformationSum[[i, i]]]], {i, 2 ^ n}]]};

```

```
148 ]
149
150
151 couplingTensor[n_, adjacency_, \[Delta]Weights_, OptionsPattern[{Model -> ToString[XXX
152   ↪ ]}]] := Module[
153 {
154   weights = Join[Table[Normal[Symmetrize[RandomReal[{\[Delta]Weights[[i, 1]] - \[
155     ↪ \[Delta]Weights[[i, 2]], \[Delta]Weights[[i, 1]] + \[Delta]Weights[[i, 2]]}], {n, n
156   ↪ }]}], {i, 3}], Table[0, {1}, {n}, {n}]],
157   weightsIndex = OptionValue[Model] /. {"XXX" -> {1, 1, 1}, "XXZ" -> {1, 1, 2}, "
158   ↪ XYZ" -> {1, 2, 3}, "IsingX" -> {1, 4, 4}, "IsingY" -> {4, 1, 4}, "IsingZ" -> {4,
159   ↪ 4, 1}}
160   },
161   Table[adjacency * weights[[weightsIndex[[i]], ;, , ;]], {i, 3}]
162 ]
163
164
165 FourPointOTOC3[waveFunction_, forwardTimeEvolve_, n_, i_, jTable_, spinOperator1_,
166   spinOperator2_] := Module[{[
167   },
168   operatorTimeEvolve = Conjugate[forwardTimeEvolve].pauliTensor[spinOperator1, i, n
169   ↪ ].forwardTimeEvolve;
170
171   psi2Temp1 = ParallelTable[Normal[pauliTensor[spinOperator2, j, n]].waveFunction, {
172     ↪ j, jTable}];
173   psi2 = ParallelTable[operatorTimeEvolve.psi2Temp1[[j]], {j, jTable}];
174
175   psi1Temp1 = operatorTimeEvolve.waveFunction;
176   psi1 = ParallelTable[pauliTensor[spinOperator2, j, n].psi1Temp1, {j, jTable}];
177
178   Table[Dot[Flatten[Conjugate[psi2[[v]]]], Flatten[psi1[[v]]]], {v, n}]
```

```
178
179 ]
180
181
182 FourPointOTOC2[waveFunction_, forwardTimeEvolve_, n_, i_, jTable_, spinOperator1_,
183   ↪ spinOperator2_] := FourPointOTOC2[waveFunction, forwardTimeEvolve, n, i, jTable,
184   ↪ spinOperator1, spinOperator2] = Module[{
185
186   },
187
188   operatorTimeEvolve = ParallelTable[Normal[Conjugate[forwardTimeEvolve] .
189   ↪ PauliTensor[spinOperator1, j, n].forwardTimeEvolve, {j, jTable}];
190
191   psi1Temp1 = ParallelTable[operatorTimeEvolve[[j]].waveFunction, {j, jTable}];
192   psi1 = ParallelTable[Normal[PauliTensor[spinOperator2, i, n]].psi1Temp1[[j]], {j
193   ↪ , jTable}];
194
195   psi2Temp1 = Normal[PauliTensor[spinOperator2, i, n]].waveFunction;
196   psi2 = ParallelTable[operatorTimeEvolve[[j]].psi2Temp1, {j, jTable}];
197
198   Table[Dot[Flatten[Conjugate[psi2[[v]]]], Flatten[psi1[[v]]]], {v, n}]
199 ]
200
201
202
203
204
205 OTOEvolution3[parameterTable_, timesTable_, waveFunction_, site_, OptionsPattern[{
206   ↪ Operator1 -> ToString[Z], Operator2 -> ToString[Z], ExternalField -> ToString[Z
207   ↪ ]}]] := Module[{
208
209   nVertices = parameterTable[[2]],
210
211   nTimeSteps = Length[timesTable],
212
213   hamiltonian = SpinHalfHamiltonian[parameterTable[[2]], parameterTable[[3]],
214   ↪ parameterTable[[4]], parameterTable[[7]], parameterTable[[6]], Model ->
215   ↪ parameterTable[[1]], Field -> OptionValue[ExternalField]],
216
217   operator1 = OptionValue[operator1] /. {"I" -> 0, "X" -> 1, "Y" -> 2, "Z" -> 3},
```

```
208
209     operator2 = OptionValue[Operator2] /. {"I" -> 0, "X" -> 1, "Y" -> 2, "Z" -> 3},
210
211     jSites = Table[Mod[v + site - 1, parameterTable[[2]], 1], {v, parameterTable
212     ↪ [[2]]}],
213
214     correlator = Table[0, {parameterTable[[2]]}, {Length[timesTable]}],
215
216     n
217
218     }, {
219
220     {eigenvalues, eigenvectorsRows} = Eigensystem[Normal[Chop[hamiltonian[[3]]]] +
221     ↪ Chop[hamiltonian[[4]]]]];
222
223     eigenvectorsCols = ConjugateTranspose[eigenvectorsRows];
224
225     For[n = 1, n <= nTimeSteps, n++,
226     {
227
228         forwardTimeEvolve = eigenvectorsCols.DiagonalMatrix[Exp[-I*eigenvalues *
229         ↪ timesTable[[n]]]].eigenvectorsRows,
230
231         correlator[[All, n]] = FourPointOTOC3[waveFunction, forwardTimeEvolve,
232         ↪ nVertices, site, jSites, operator1, operator2],
233
234         (*Print[ToString[n]]*)
235
236     }
237
238 ];
239
240     correlatorNorm = Table[Norm[correlator[[v, t]]]^2, {v, nVertices}, {t,
241     ↪ nTimeSteps}];
242
243     correlatorReal = Table[(1 - Re[correlator[[v, t]]]), {v, nVertices}, {t,
244     ↪ nTimeSteps}];
```

```
239     vertexList = If[EvenQ[nVertices], Append[Table[Mod[n - Floor[nVertices/2],  
240      nVertices, 1], {n, nVertices}], Ceiling[nVertices / 2] + 1], Table[Mod[n - Floor  
241      [nVertices/2], nVertices, 1], {n, nVertices}]] ;  
242  
243     correlatorNormTable = Table[{timesTable[[t]], correlatorNorm[[v, t]]}, {t,  
244      nTimeSteps}, {v, nVertices}];  
245  
246     correlatorRealTable = Table[{timesTable[[t]], correlatorReal[[v, t]]}, {t,  
247      nTimeSteps}, {v, nVertices}];  
248  
249   }; {  
250  
251     correlatorRealTable,  
252  
253       ListPlot3D[Table[correlatorRealTable[[;; , v, 2]], {v, vertexList}], DataRange  
254       -> {{timesTable[[1]], timesTable[[nTimeSteps]]}, {1, nVertices}}, ColorFunction  
255       -> "TemperatureMap", ViewPoint -> {-90, -135, 180}, PlotRange -> All, Ticks ->  
256       None, AxesLabel -> {"Time", "Vertex", "C(t)}],  
257  
258     ListPlot[Table[correlatorRealTable[[;; , v, ;]], {v, nVertices}], Joined ->  
259       True, PlotRange -> All, Frame -> True, FrameLabel -> {"Time", "C(t)"}],  
260  
261     hamiltonian  
262  
263     (*, FrameTicks-> {{{0, 0.5, SetPrecision[1.0,2], 1.5, SetPrecision[2.0,2], 2.5,  
264       SetPrecision[3.0,2], 3.5}, None},{{0, 0.01, 0.1, SetPrecision[1.0, 2],  
265       SetPrecision[10.0, 3],SetPrecision[100.0, 4]}, None}}, Frame->True*)  
266   ]  
267  
268  
269 FindConvexData[data_] := FindConvexData[data] = Module[{  
270  
271     convexUpToPosition = Position[Sign[Differences[Differences[Chop[data[[;; ,  
272       2]]]]]], -1][[1, 1]] + 1,  
273  
274     convexData  
275  
276   },
```

```
266
267     convexData = data[[1 ;; convexUpToPosition]]
268
269 ]
270
271
272 InflectionPointPosition[data_, tolerance_, curvatureChange_] := Module[{  
273
274 },  
275
276     Position[Sign[Chop[Differences[Differences[data]], tolerance]], curvatureChange  
277     ↪ ] [[1, 1]] + 1
278 ]
279
280
281 MaxPointPosition[data_] := Module[{  
282
283     diff
284
285 },  
286
287     diff = Differences[Differences[data]];
288     Flatten[Position[diff, n_ /; n == Max[diff]]][[1]]
289
290 ]
291
292
293 FindBestFitModel[data_] := FindBestFitModel[data] = Module[{  
294
295     modelExp = a (E^(b x) - 1),
296
297     modelPol = a x^b
298
299     (*modelSin = a Cos[b x + c] + d*)
300
301 }, {
302 }
```

```
303 NonlinearModelFit[data, modelExp, {{a, 10^-6}, {b, 1}}, x],  
304  
305 NonlinearModelFit[data, modelPol, {a, b}, x]  
306  
307 (*NonlinearModelFit[data, modelSin, {{a, -Max[data]}, b, {c, -1}, {d, Max[data]}}, x]  
308    *)  
309 }]  
310  
311  
312 FitOTOCs[OTOC_] := Module[{  
313  
314     dataSetNonZero  
315  
316     }, {  
317  
318     dataSetNonZero = DeleteCases[Table[If[AllTrue[Chop[OTOC[[1, ;;, i, ;;]]][[;;,  
319     2]], # == 0 &], Null, OTOC[[1, ;;, i, ;;]]], {i, Dimensions[OTOC[[1, ;;, ;, ;,  
320     ;]]][[2]]}], Null],  
321     Table[FindBestFitModel[dataSetNonZero[[i]]], {i, Dimensions[dataSetNonZero  
322     ][[1]]}]  
323     }]  
324  
325 PlotFittedOTOCs[OTOCData_, fittedData_, fittedModels_] := Module[{  
326  
327     PlotOTOC = ListPlot[OTOCData, PlotStyle -> Black],  
328  
329     PlotFittedData = ListPlot[fittedData, PlotStyle -> Green],  
330  
331     PlotExp = Plot[Table[fittedData[[2, i, 2]]["BestFit"], {i, Dimensions[fittedData  
332     ][[2]]][[1]]}], {x, 0, Last[fittedData[[1, 1]][[;;, 1]]]}, PlotStyle ->  
333     Directive[Red, Thin]],  
334  
335     PlotPol = Plot[Table[fittedData[[2, i, 3]]["BestFit"], {i, Dimensions[fittedData  
336     ][[2]]][[1]]}], {x, 0, Last[fittedData[[1, 1]][[;;, 1]]]}, PlotStyle ->
```

```
334  ↪ Directive[Red, Thin]],  
335  PlotSin = Plot[Table[fittedData[[2, i, 4]]["BestFit"], {i, Dimensions[fittedData  
336  ↪ [[2]]][[1]]}], {x, 0, Last[fittedData[[1, 1]][[;; , 1]]]}, PlotStyle ->  
337  ↪ Directive[Red, Thin]],  
338  
339  RSquaredExp = Table[fittedData[[2, i, 2]]["RSquared"], {i, Dimensions[fittedData  
340  ↪ [[2]]][[1]]}],  
341  
342  RSquaredPol = Table[fittedData[[2, i, 3]]["RSquared"], {i, Dimensions[fittedData  
343  ↪ [[2]]][[1]]}],  
344  
345  RSquaredSin = Table[fittedData[[2, i, 4]]["RSquared"], {i, Dimensions[fittedData  
346  ↪ [[2]]][[1]]}]  
347  
348  }, {  
349  
350  Show[PlotOTOC, PlotConvex, PlotExp, Frame -> True, FrameLabel -> {"t", "C(t)", "  
351  ↪ Exponential Fit"}],  
352  
353  Show[PlotOTOC, PlotConvex, PlotPol, Frame -> True, FrameLabel -> {"t", "C(t)", "  
354  ↪ Polynomial Fit"}],  
355  
356  Show[PlotOTOC, PlotConvex, PlotSin, Frame -> True, FrameLabel -> {"t", "C(t)", "  
357  ↪ Sinusoidal Fit"}],  
358  
359  {RSquaredExp, RSquaredPol, RSquaredSin}  
360  
361  }]  
362  
363 powerLawZZ[t_, l_, J_, g_] := 2*((J t)^(4l + 2) g^(2 l + 2))/((2l+1)!)^2  
364  
365 powerLawXZ[t_, l_, J_, g_] := 2*((J t)^(4l) g^(2 l))/((2l)!)^2  
366  
367 powerLawXX[t_, l_, J_, g_] := 2*((J t)^(4l - 2) g^(2 l - 2))/((2l-1)!)^2
```

```
363
364
365 powerLawXXX[t_, l_, K_, g_] := (t)^(21)/(2 l-(K-1))!
366
367
368 RSquaredPowerLawZZ[list_, v_] := 1 - SquaredEuclideanDistance[list[[;; , 2]],
369   ↪ powerLawZZ[#, v, 1, 1] & /@ list[[;; , 1]]]/SquaredEuclideanDistance[list[[;; ,
370   ↪ 2]], Mean@list[[;; , 2]]]
371
372 SFF[eigenvalues_, timeSteps_] := Module[
373   {
374     nEigenvalues = Length[eigenvalues]
375   },
376   nEigenvalues + Sum[Sum[2 * Cos[(eigenvalues[[n]] - eigenvalues[[m]]) * #], {m, n -
377     ↪ 1}], {n, 2, nEigenvalues, 1}] & /@ timeSteps
378
379 ]
380
```

---

## Bibliography

---

- [1] Jordan S. Cotler, Guy Gur-Ari, Masanori Hanada, Joseph Polchinski, Phil Saad, Stephen H. Shenker, Douglas Stanford, Alexandre Streicher, and Masaki Tezuka. Black Holes and Random Matrices. *Journal of High Energy Physics*, 2017(5), May 2017. arXiv: 1611.04650. URL: <http://arxiv.org/abs/1611.04650>, doi:10.1007/JHEP05(2017)118.
- [2] Balázs Dóra and Roderich Moessner. Out-of-Time-Ordered Density Correlators in Luttinger Liquids. *Physical Review Letters*, 119(2):026802, July 2017. URL: <http://link.aps.org/doi/10.1103/PhysRevLett.119.026802>, doi: 10.1103/PhysRevLett.119.026802.
- [3] Edward N. Lorenz. Deterministic Nonperiodic Flow. *Journal of Atmospheric Sciences*, 20(2):130–148, March 1963. doi:10.1175/1520-0469(1963)020<0130: DNF>2.0.CO;2.
- [4] Edward N. Lorenz. Predictability; Does the Flap of a Butterfly’s wings in Brazil Set Off a Tornado in Texas? In *American Association for the Advancement of Science, 139th Meeting*, Cambridge, Mass, December 1972.
- [5] M. C. Gutzwiller. *Chaos in classical and quantum mechanics*. Number v. 1 in Interdisciplinary applied mathematics. Springer-Verlag, New York, 1990.
- [6] Michael Berry. Quantum chaology, not quantum chaos. *Physica Scripta*, 40(3):335–

- 336, September 1989. URL: <https://doi.org/10.1088%2F0031-8949%2F40%2F3%2F013>, doi:10.1088/0031-8949/40/3/013.
- [7] Stephen H. Shenker and Douglas Stanford. Black holes and the butterfly effect. *Journal of High Energy Physics*, 2014(3):67, March 2014. arXiv: 1306.0622. URL: <http://arxiv.org/abs/1306.0622>, doi:10.1007/JHEP03(2014)067.
- [8] Patrick Hayden and John Preskill. Black holes as mirrors: quantum information in random subsystems. *Journal of High Energy Physics*, 2007(09):120–120, September 2007. arXiv: 0708.4025. URL: <http://arxiv.org/abs/0708.4025>, doi:10.1088/1126-6708/2007/09/120.
- [9] Yasuhiro Sekino and Leonard Susskind. Fast Scramblers. *Journal of High Energy Physics*, 2008(10):065–065, October 2008. arXiv: 0808.2096. URL: <http://arxiv.org/abs/0808.2096>, doi:10.1088/1126-6708/2008/10/065.
- [10] Shenglong Xu and Brian Swingle. Locality, Quantum Fluctuations, and Scrambling. *Physical Review X*, 9(3):031048, September 2019. URL: <https://link.aps.org/doi/10.1103/PhysRevX.9.031048>, doi:10.1103/PhysRevX.9.031048.
- [11] J. M. Deutsch. Quantum statistical mechanics in a closed system. *Physical Review A*, 43(4):2046–2049, February 1991. URL: <https://link.aps.org/doi/10.1103/PhysRevA.43.2046>, doi:10.1103/PhysRevA.43.2046.
- [12] Mark Srednicki. Chaos and quantum thermalization. *Physical Review E*, 50(2):888–901, August 1994. URL: <https://link.aps.org/doi/10.1103/PhysRevE.50.888>, doi:10.1103/PhysRevE.50.888.
- [13] P. W. Anderson. Absence of Diffusion in Certain Random Lattices. *Physical Review*, 109(5):1492–1505, March 1958. URL: <https://link.aps.org/doi/10.1103/PhysRev.109.1492>, doi:10.1103/PhysRev.109.1492.
- [14] D. M. Basko, I. L. Aleiner, and B. L. Altshuler. Metal-insulator transition in a weakly interacting many-electron system with localized single-particle states. *Annals of Physics*, 321(5):1126–1205, May 2006. arXiv: cond-mat/0506617. URL: <http://arxiv.org/abs/cond-mat/0506617>, doi:10.1016/j.aop.2005.11.014.

## BIBLIOGRAPHY

---

- [15] J. Šuntajs, J. Bonča, T. Prosen, and L. Vidmar. Quantum chaos challenges many-body localization. *arXiv:1905.06345 [cond-mat, physics:hep-th, physics:quant-ph]*, June 2019. arXiv: 1905.06345. URL: <http://arxiv.org/abs/1905.06345>.
- [16] Clara Moskowitz. Tangled Up in Spacetime. *Scientific American*, October 2016. URL: <https://www.scientificamerican.com/article/tangled-up-in-spacetime/>.
- [17] Juan M. Maldacena. The Large N Limit of Superconformal Field Theories and Supergravity. *International Journal of Theoretical Physics*, 38(4):1113–1133, 1999. arXiv: hep-th/9711200. URL: <http://arxiv.org/abs/hep-th/9711200>, doi:10.1023/A:1026654312961.
- [18] Juan Maldacena, Stephen H. Shenker, and Douglas Stanford. A bound on chaos. *Journal of High Energy Physics*, 2016(8), August 2016. arXiv: 1503.01409. URL: <http://arxiv.org/abs/1503.01409>, doi:10.1007/JHEP08(2016)106.
- [19] Subir Sachdev and Jinwu Ye. Gapless Spin-Fluid Ground State in a Random Quantum Heisenberg Magnet. *Physical Review Letters*, 70(21):3339–3342, May 1993. arXiv: cond-mat/9212030. URL: <http://arxiv.org/abs/cond-mat/9212030>, doi:10.1103/PhysRevLett.70.3339.
- [20] Alexei Kitaev. A Simple Model of Quantum Holography, July 2015. URL: <http://online.kitp.ucsb.edu/online/entangled15/kitaev/>; <http://online.kitp.ucsb.edu/online/entangled15/kitaev2/>.
- [21] Edward Witten. An SYK-Like Model Without Disorder. *arXiv:1610.09758 [hep-th]*, November 2016. arXiv: 1610.09758. URL: <http://arxiv.org/abs/1610.09758>.
- [22] Razvan Gurau. The 1/N Expansion of Colored Tensor Models. *Annales Henri Poincaré*, 12(5):829–847, July 2011. URL: <http://link.springer.com/10.1007/s00023-011-0101-8>, doi:10.1007/s00023-011-0101-8.
- [23] Cheng-Ju Lin and Olexei I. Motrunich. Out-of-time-ordered correlators in quantum Ising chain. *Physical Review B*, 97(14), April 2018. arXiv: 1801.01636. URL: <http://arxiv.org/abs/1801.01636>, doi:10.1103/PhysRevB.97.144304.
- [24] A. Georges, O. Parcollet, and S. Sachdev. Quantum Fluctuations of a Nearly Criti-

- cal Heisenberg Spin Glass. *Physical Review B*, 63(13), March 2001. arXiv: cond-mat/0009388. URL: <http://arxiv.org/abs/cond-mat/0009388>, doi:10.1103/PhysRevB.63.134406.
- [25] David Sherrington and Scott Kirkpatrick. Solvable Model of a Spin-Glass. *Physical Review Letters*, 35(26):1792–1796, December 1975. URL: <https://link.aps.org/doi/10.1103/PhysRevLett.35.1792>, doi:10.1103/PhysRevLett.35.1792.
- [26] David J. Luitz and Yevgeny Bar Lev. Emergent locality in systems with power-law interactions. arXiv:1805.06895 [cond-mat], May 2018. arXiv: 1805.06895. URL: <http://arxiv.org/abs/1805.06895>.
- [27] Benedikt Kloss and Yevgeny Bar Lev. Spin transport in long-range interacting one-dimensional chain. arXiv:1804.05841 [cond-mat], April 2018. arXiv: 1804.05841. URL: <http://arxiv.org/abs/1804.05841>.
- [28] Y. A. Kharkov, V. E. Sotskov, A. A. Karazeev, E. O. Kiktenko, and A. K. Fedorov. Revealing quantum chaos with machine learning. arXiv:1902.09216 [cond-mat, physics:quant-ph], February 2019. arXiv: 1902.09216. URL: <http://arxiv.org/abs/1902.09216>.
- [29] S F Edwards and P W Anderson. Theory of spin glasses. *Journal of Physics F: Metal Physics*, 5(5):965–974, May 1975. URL: <http://stacks.iop.org/0305-4608/5/i=5/a=017?key=crossref.425898dadf35a95c9904e9235ef48585>, doi:10.1088/0305-4608/5/5/017.
- [30] Gregory Bentsen, Yingfei Gu, and Andrew Lucas. Fast scrambling on sparse graphs. arXiv:1805.08215 [cond-mat, physics:hep-th, physics:quant-ph], May 2018. arXiv: 1805.08215. URL: <http://arxiv.org/abs/1805.08215>.
- [31] Duncan J. Watts and Steven H. Strogatz. Collective dynamics of ‘small-world’ networks. *Nature*, 393(6684):440–442, June 1998. URL: <https://doi.org/10.1038/30918>, doi:10.1038/30918.
- [32] Albert-László Barabási. *Linked: the new science of networks*. Perseus Pub, Cambridge, Mass, 2002.

## BIBLIOGRAPHY

---

- [33] Olaf Sporns and Jonathan D. Zwi. The Small World of the Cerebral Cortex. *Neuroinformatics*, 2(2):145–162, 2004. URL: <http://link.springer.com/10.1385/NI:2:2:145>, doi:10.1385/NI:2:2:145.
- [34] Olaf Sporns. *Networks of the brain*. MIT Press, Cambridge, Mass, 2011. OCLC: ocn551342282.
- [35] Qawi K. Telesford, Karen E. Joyce, Satoru Hayasaka, Jonathan H. Burdette, and Paul J. Laurienti. The Ubiquity of Small-World Networks. *Brain Connectivity*, 1(5):367–375, December 2011. URL: <http://www.liebertpub.com/doi/10.1089/brain.2011.0038>, doi:10.1089/brain.2011.0038.
- [36] Richard Van Noorden, Brendan Maher, and Regina Nuzzo. The top 100 papers. October 2014. URL: <https://www.nature.com/news/the-top-100-papers-1.16224>.
- [37] Yu N Ovchinnikov and A.I. Larkin. Quasiclassical Method in the Theory of Superconductivity. *Soviet Journal of Experimental and Theoretical Physics*, 28:1200, June 1969.
- [38] Daniel A. Roberts and Douglas Stanford. Two-dimensional conformal field theory and the butterfly effect. *Physical Review Letters*, 115(13):131603, September 2015. arXiv: 1412.5123. URL: <http://arxiv.org/abs/1412.5123>, doi:10.1103/PhysRevLett.115.131603.
- [39] Koji Hashimoto, Keiju Murata, and Ryosuke Yoshii. Out-of-time-order correlators in quantum mechanics. *Journal of High Energy Physics*, 2017(10), October 2017. arXiv: 1703.09435. URL: <http://arxiv.org/abs/1703.09435>, doi:10.1007/JHEP10(2017)138.
- [40] Madan Lal Mehta. *Random matrices*. Number 142 in Pure and applied mathematics series. Elsevier, Amsterdam, 3. ed edition, 2004. OCLC: 253930836.
- [41] Robert de Mello Koch, Jia-Hui Huang, Chen-Te Ma, and Hendrik J. R. Van Zyl. Spectral Form Factor as an OTOC Averaged over the Heisenberg Group. *Physics Letters B*, 795:183–187, August 2019. arXiv: 1905.10981. URL: <http://arxiv.org/abs/1905.10981>, doi:10.1016/j.physletb.2019.06.025.

- [42] Jordan Cotler, Nicholas Hunter-Jones, Junyu Liu, and Beni Yoshida. Chaos, Complexity, and Random Matrices. *Journal of High Energy Physics*, 2017(11), November 2017. arXiv: 1706.05400. URL: <http://arxiv.org/abs/1706.05400>, doi:10.1007/JHEP11(2017)048.
- [43] Jonah Kudler-Flam, Laimei Nie, and Shinsei Ryu. Conformal field theory and the web of quantum chaos diagnostics. *Journal of High Energy Physics*, 2020(1):175, January 2020. arXiv: 1910.14575. URL: <http://arxiv.org/abs/1910.14575>, doi:10.1007/JHEP01(2020)175.
- [44] Jean-Gabriel Hartmann, Jeff Murugan, and Jonathan P. Shock. Chaos and Scrambling in Quantum Small Worlds. *arXiv:1901.04561 [cond-mat, physics:hep-th, physics:quant-ph]*, January 2019. arXiv: 1901.04561. URL: <http://arxiv.org/abs/1901.04561>.
- [45] John Guare. *Six Degrees of Separation*. Random House, New York, 1990.
- [46] Stanley Milgram. The small-world problem: (400002009-005). Technical report, American Psychological Association, 1967. type: dataset. URL: <http://doi.apa.org/get-pe-doi.cfm?doi=10.1037/e400002009-005>, doi:10.1037/e400002009-005.
- [47] Alexei Kitaev and S. Josephine Suh. The soft mode in the Sachdev-Ye-Kitaev model and its gravity dual. *Journal of High Energy Physics*, 2018(5):183, May 2018. arXiv: 1711.08467. URL: <http://arxiv.org/abs/1711.08467>, doi:10.1007/JHEP05(2018)183.
- [48] Paul Erdős and Alfréd Rényi. On Random Graphs I. *Publicationes Mathematicae Debrecen*, 6:290, 1959.
- [49] E. N. Gilbert. Random Graphs. *The Annals of Mathematical Statistics*, 30(4):1141–1144, December 1959. URL: <http://projecteuclid.org/euclid.aoms/1177706098>, doi:10.1214/aoms/1177706098.
- [50] Jaroslav Nešetřil and Patrice Ossona de Mendez. *Sparsity*, volume 28 of *Algorithms and Combinatorics*. Springer Berlin Heidelberg, Berlin, Heidelberg, 2012.

## BIBLIOGRAPHY

---

- URL: <http://link.springer.com/10.1007/978-3-642-27875-4>, doi:10.1007/978-3-642-27875-4.
- [51] Swati Goswami, C. A. Murthy, and Asit K. Das. Sparsity Measure of a Network Graph: Gini Index. *arXiv:1612.07074 [physics]*, December 2016. arXiv: 1612.07074. URL: <http://arxiv.org/abs/1612.07074>.
- [52] E. W. Dijkstra. A note on two problems in connexion with graphs. *Numerische Mathematik*, 1(1):269–271, December 1959. URL: <http://link.springer.com/10.1007/BF01386390>, doi:10.1007/BF01386390.
- [53] Richard Bellman. On a routing problem. *Quarterly of Applied Mathematics*, 16(1):87–90, April 1958. URL: <http://www.ams.org/qam/1958-16-01/S0033-569X-1958-0102435-2/>, doi:10.1090/qam/102435.
- [54] Robert W. Floyd. Algorithm 97: Shortest path. *Communications of the ACM*, 5(6):345, June 1962. URL: <http://portal.acm.org/citation.cfm?doid=367766.368168>, doi:10.1145/367766.368168.
- [55] Mark D. Humphries and Kevin Gurney. Network ‘Small-World-Ness’: A Quantitative Method for Determining Canonical Network Equivalence. *PLoS ONE*, 3(4):e0002051, April 2008. URL: <http://dx.plos.org/10.1371/journal.pone.0002051>, doi:10.1371/journal.pone.0002051.
- [56] Vito Latora and Massimo Marchiori. Efficient Behavior of Small-World Networks. *Physical Review Letters*, 87(19):198701, October 2001. arXiv: cond-mat/0101396. URL: <http://arxiv.org/abs/cond-mat/0101396>, doi:10.1103/PhysRevLett.87.198701.
- [57] Henri Poincaré. *Science and method*. Dover Publications, Mineola, N.Y, dover ed edition, 2003.
- [58] Steven Henry Strogatz. *Nonlinear dynamics and chaos: with applications to physics, biology, chemistry, and engineering*. Studies in Nonlinearity. Perseus Books, Cambridge, Mass, 2. print edition, 2001. OCLC: 248691524.
- [59] Ja. G. Sinai. Dynamical systems with elastic reflections. Ergodic properties of dis-

- persing billiards. *Akademiya Nauk SSSR i Moskovskoe Matematicheskoe Obshchestvo. Uspekhi Matematicheskikh Nauk*, 25(2 (152)):141–192, 1970.
- [60] L.A. Bunimovich. Many-dimensional nowhere dispersing billiards with chaotic behavior. *Physica D: Nonlinear Phenomena*, 33(1-3):58–64, October 1988. URL: <https://linkinghub.elsevier.com/retrieve/pii/S0167278998900094>, doi:10.1016/S0167-2789(98)90009-4.
- [61] Eugene P. Wigner. Characteristic Vectors of Bordered Matrices With Infinite Dimensions. *The Annals of Mathematics*, 62(3):548, November 1955. URL: <https://www.jstor.org/stable/1970079?origin=crossref>, doi:10.2307/1970079.
- [62] Freeman J. Dyson. Statistical Theory of the Energy Levels of Complex Systems. I. *Journal of Mathematical Physics*, 3(1):140–156, January 1962. URL: <http://aip.scitation.org/doi/10.1063/1.1703773>, doi:10.1063/1.1703773.
- [63] Jens Marklof. The Berry-Tabor Conjecture. In Carles Casacuberta, Rosa Maria Miró-Roig, Joan Verdera, and Sebastià Xambó-Descamps, editors, *European Congress of Mathematics*, pages 421–427. Birkhäuser Basel, Basel, 2001. URL: [http://link.springer.com/10.1007/978-3-0348-8266-8\\_36](http://link.springer.com/10.1007/978-3-0348-8266-8_36), doi:10.1007/978-3-0348-8266-8\_36.
- [64] M. V. Berry and M. Tabor. Level Clustering in the Regular Spectrum. *Proceedings of the Royal Society of London. Series A, Mathematical and Physical Sciences*, 356(1686):375–394, 1977. URL: <http://www.jstor.org/stable/79349>.
- [65] O. Bohigas, M. J. Giannoni, and C. Schmit. Characterization of Chaotic Quantum Spectra and Universality of Level Fluctuation Laws. *Physical Review Letters*, 52(1):1–4, January 1984. URL: <https://link.aps.org/doi/10.1103/PhysRevLett.52.1>, doi:10.1103/PhysRevLett.52.1.
- [66] Corinna Kollath, Guillaume Roux, Giulio Biroli, and Andreas M Läuchli. Statistical properties of the spectrum of the extended Bose–Hubbard model. *Journal of Statistical Mechanics: Theory and Experiment*, 2010(08):P08011, August 2010.

## BIBLIOGRAPHY

---

- URL: <http://stacks.iop.org/1742-5468/2010/i=08/a=P08011?key=crossref.8a5b4f65a6aaca229615742b01760d5e>, doi:10.1088/1742-5468/2010/08/P08011.
- [67] Bertrand Eynard, Taro Kimura, and Sylvain Ribault. Random matrices. *arXiv:1510.04430 [cond-mat, physics:hep-th, physics:math-ph]*, July 2018. arXiv: 1510.04430. URL: <http://arxiv.org/abs/1510.04430>.
- [68] Y. Y. Atas, E. Bogomolny, O. Giraud, and G. Roux. Distribution of the Ratio of Consecutive Level Spacings in Random Matrix Ensembles. *Physical Review Letters*, 110(8):084101, February 2013. URL: <https://link.aps.org/doi/10.1103/PhysRevLett.110.084101>, doi:10.1103/PhysRevLett.110.084101.
- [69] Vadim Oganesyan and David A. Huse. Localization of interacting fermions at high temperature. *Physical Review B*, 75(15):155111, April 2007. URL: <https://link.aps.org/doi/10.1103/PhysRevB.75.155111>, doi:10.1103/PhysRevB.75.155111.
- [70] Alexei Kitaev. Hidden Correlations in the Hawking Radiation and Thermal Noise, October 2014.
- [71] Stephen H. Shenker and Douglas Stanford. Stringy effects in scrambling. *arXiv:1412.6087 [hep-th]*, March 2015. arXiv: 1412.6087. URL: <http://arxiv.org/abs/1412.6087>.
- [72] Shenglong Xu and Brian Swingle. Locality, Quantum Fluctuations, and Scrambling. *arXiv:1805.05376 [cond-mat, physics:hep-th, physics:quant-ph]*, May 2018. arXiv: 1805.05376. URL: <http://arxiv.org/abs/1805.05376>.
- [73] David J. Luitz and Yevgeny Bar Lev. Information propagation in isolated quantum systems. *Physical Review B*, 96(2), July 2017. arXiv: 1702.03929. URL: <http://arxiv.org/abs/1702.03929>, doi:10.1103/PhysRevB.96.020406.
- [74] David A. Lowe and Mengyang Tong. Black Hole Interiors via Spin Models. *arXiv:1908.11190 [hep-th]*, August 2019. arXiv: 1908.11190. URL: <http://arxiv.org/abs/1908.11190>.
- [75] Tomoki Nosaka, Dario Rosa, and Junggi Yoon. Thouless time for mass-deformed

- SYK. *Journal of High Energy Physics*, 2018(9), September 2018. arXiv: 1804.09934. URL: <http://arxiv.org/abs/1804.09934>, doi:10.1007/JHEP09(2018)041.
- [76] Juan Maldacena and Douglas Stanford. Comments on the Sachdev-Ye-Kitaev model. *Physical Review D*, 94(10), November 2016. arXiv: 1604.07818. URL: <http://arxiv.org/abs/1604.07818>, doi:10.1103/PhysRevD.94.106002.
- [77] Robin Steinigeweg, Jochen Gemmer, and Wolfram Brenig. Spin-Current Autocorrelations from Single Pure-State Propagation. *Physical Review Letters*, 112(12), March 2014. URL: <https://link.aps.org/doi/10.1103/PhysRevLett.112.120601>, doi:10.1103/PhysRevLett.112.120601.
- [78] Michel Ledoux. *The concentration of measure phenomenon*. Number Issue 89 in Mathematical surveys and monographs. American Mathematical Society, 2001. OCLC: 880580292. URL: <http://www.ams.org/surv/089>.
- [79] Vitali Milman and Gideon Schechtman. *Asymptotic Theory of Finite Dimensional Normed Spaces*, volume 1200 of *Lecture Notes in Mathematics*. Springer Berlin Heidelberg, Berlin, Heidelberg, 1986. URL: <http://link.springer.com/10.1007/978-3-540-38822-7>, doi:10.1007/978-3-540-38822-7.
- [80] David J. Luitz and Yevgeny Bar Lev. The Ergodic Side of the Many-Body Localization Transition. *Annalen der Physik*, 529(7):1600350, July 2017. arXiv: 1610.08993. URL: <http://arxiv.org/abs/1610.08993>, doi:10.1002/andp.201600350.
- [81] Antonio M. García-García, Bruno Loureiro, Aurelio Romero-Bermúdez, and Masaki Tezuka. Chaotic-Integrable Transition in the Sachdev-Ye-Kitaev Model. *Physical Review Letters*, 120(24):241603, June 2018. URL: <https://link.aps.org/doi/10.1103/PhysRevLett.120.241603>, doi:10.1103/PhysRevLett.120.241603.
- [82] David Hilbert. volume 3, page 387, Konigsberg, 1930.
- [83] David J. Griffiths. *Introduction to quantum mechanics*. Pearson, Prentice Hall, Upper Saddle River, NJ, 2. ed., international ed edition, 2005. OCLC: 249367270.
- [84] Michael A. Nielsen and Isaac L. Chuang. *Quantum computation and quantum information*. Cambridge University Press, Cambridge ; New York, 2000.

## BIBLIOGRAPHY

---

- [85] Philippe Sabella-Garnier, Koenraad Schalm, Tereza Vakhtel, and Jan Zaanen. Thermalization/Relaxation in integrable and free field theories: an Operator Thermalization Hypothesis. *arXiv:1906.02597 [cond-mat, physics:hep-th, physics:quant-ph]*, September 2019. arXiv: 1906.02597. URL: <http://arxiv.org/abs/1906.02597>.
- [86] R. J. Lewis-Swan, A. Safavi-Naini, J. J. Bollinger, and A. M. Rey. Unifying scrambling, thermalization and entanglement through measurement of fidelity out-of-time-order correlators in the Dicke model. *Nature Communications*, 10(1):1581, December 2019. URL: <http://www.nature.com/articles/s41467-019-09436-y>, doi:10.1038/s41467-019-09436-y.
- [87] Daniel A. Roberts and Brian Swingle. Lieb-Robinson and the butterfly effect. *Physical Review Letters*, 117(9):091602, August 2016. arXiv: 1603.09298. URL: <http://arxiv.org/abs/1603.09298>, doi:10.1103/PhysRevLett.117.091602.
- [88] H. Bethe. Zur Theorie der Metalle: I. Eigenwerte und Eigenfunktionen der linearen Atomkette. *Zeitschrift fur Physik*, 71(3-4):205–226, March 1931. URL: <http://link.springer.com/10.1007/BF01341708>, doi:10.1007/BF01341708.